2017

Rational Synthesis Of Catalysts For Biomass Conversion

Qiuli Liu
University of South Carolina

RATIONAL SYNTHESIS OF CATALYSTS FOR BIOMASS CONVERSION

by

Qiuli Liu

Bachelor of Science
Dalian University of Technology, 2011

Submitted in Partial Fulfillment of the Requirements

For the Degree of Doctor of Philosophy in

Chemical Engineering

College of Engineering and Computing

University of South Carolina

2017

Accepted by:

John R. Regalbuto, Major Professor

John R. Monnier, Committee Member

John W. Weidner, Committee Member

Christopher T. Williams, Committee Member

Aaron K. Vannucci, Committee Member

Cheryl L. Addy, Vice Provost and Dean of the Graduate School

Dedication

Dedicated to my parents, Daofu Liu and Fenghua Li who are always supportive. I am looking forward to our next family travel. Also to my elder brother, Zhongqing Liu, sister-in-law, Mingguo Wu. They are taking good care of my parents in the past five years. To my nephew, Qixin Liu who wants to study anthropology or history in the future and he told me so many stories which I wouldn't know as a chemical engineer.

Acknowledgements

I would like to first acknowledge my supervisor, Dr. John R. Regalbuto for taking me into a dynamic group and guiding me in my research. He is always inspiring and patience no matter how bad my written English is. Without his help, I couldn't have published four papers. Thanks for his trust and encouragement when I was frustrated. Thanks for his support letting me attend many conferences and meetings which have broadened my research perspective. It is lucky to work with him.

I would also like to appreciate my committee members, Dr. John R. Monnier, Dr. Christopher T. Williams, Dr. Aaron K. Vannucci and Dr. John W. Weidner for their advices after my comprehensive exam and their time to review my work. Thanks Dr. Monnier for sparing time to teach me so much in catalysis which I believe will be my lifetime treasure, and your positive feedback on my fashion is also greatly appreciated.

Besides, I would like to show my greatest appreciation to USDA for funding my research during my PhD study, and Dr. Yaseen Elkasabi and Dr. Yongsuck Choi for their effort in our cooperated project which makes greatest contribution to Chapter 3 in my dissertation.

In addition, I would like to thank staffs in the Department of Chemical Engineering: Marcia Rowen, Loretta Hardcastle, Carol Stork, Vernon Dorrell, Chase Ferch and Brian Loggans, for their help. I would like to make special mention of my colleagues: Dr. Hyeran Cho, Dr. John M. Tengco, Dr. Shuo Cao, Dr. Jadid E. Samad, Dr. Kerry O'Connell,

Dr. Ritubarna Banerjee, Dr. Weijian Diao, Dr. Yunya Zhang, Andrew P. Wong, Fahad Almalki, Jayson Keels, Sonia Eskandari, Sean Noble, Jeremiah W. Lipp and Jose L. Contreras Mora. They helped me so much in both my work and life and I've learned a lot from those interactive talks we had. Also, five undergrads I worked with, Kevin A. Über, John E. Copple, Christine M. Satterwhite, Shirlandra T. Griffin and Morgan Sulzbach, thanks for their effort in my work.

I would like to express my sincere gratitude to my friends, thanks for their generous sharing and companion.

At last, I would like to give special thanks to fried chicken (Bernie's), dark chocolate and mexican train dominoes, life would be boring without them.

Abstract

With climate change due to global warming, the production of hydrocarbon fuels and chemicals from renewable biomass resource has become more pressing in recent decades. The biggest challenge in biomass conversion is to develop active, selective and stable catalysts for particular applications. The objective of this research is to optimize catalytic performance for hydrodeoxygenation (HDO) and hydrogenation reactions by enhancing the stability of the support, tuning metal particle size, and controlling surface composition.

The high content of water in bio-oil and the aqueous environment of the upgrading process requires a hydrothermally stable catalyst. The hydrothermal stability has been effectively improved at 220^{o}C by various means: the introduction of Zr, carbon coating on silica, and the development of mesoporous alumina. Monometallic and bimetallic catalysts were prepared on these stable supports by strong electrostatic adsorption (SEA) and ultra-small nanoparticles (<2 nm) were synthesized. Stability tests at the bio-oil HDO reaction temperature of 300^{o}C revealed that the mesoporous alumina outperformed the other supports in terms surface area and pore structure maintenance, and metal particle stability. Mesoporous alumina-supported Pt/Ru and Cu/Ni were tested for HDO of bio-oil at USDA. Two methods were applied to control metal particle sizes. In the first, SEA-derived Ru and Pt nanoparticles (<2 nm) supported on mesoporous silica were treated at elevated

temperatures (800°C and 900°C) in humidified hydrogen to achieve series of catalysts with particle sizes ranging from 1 to 5 nm. This treatment, however, significantly deteriorated the support. A milder method was demonstrated via charge enhanced dry impregnation (CEDI): Pt particles were grown from about 1 to 10 nm on a variety of common supports by adding excess chloride to the impregnating solution. Particle size sensitivity to chloride was compared on various supports.

The effect on furfural hydrogenation of controlling of surface composition of bimetallic nanoparticles was demonstrated with silica supported PdCu and PdCo catalysts prepared by co-SEA, SEA followed by Electroless Deposition (SEA-ED), and dry impregnation (co-DI). SEA and co-SEA preparations yielded ultra-small (about 1 nm) single metal Pd, Cu, and Co and homogeneously alloyed PdCu and PdCo nanoparticles. Cu could be added as partial monolayer shells via ED to the SEA-synthesized Pd cores. The reaction pathway and product yield were seen to be a sensitive function of the synthesis method and corresponding surface composition.

Table of Contents

List of Tables

List of Figures

Chapter 1

Introduction

1.1 Biomass conversion

With the increasing demand for energy and depletion of fossil fuel around the world and the commensurate issue of global warming, substantial research is being carried out to find alternative fuels which are renewable, environmental friendly, and low cost, such as wind, solar, fuel cell and biomass. One fifth of total energy consumption is from transportation [1-3], and that number keeps increasing as the world's population grows. As one of the few green sources to yield liquid transportation fuel, biomass conversion has been gaining more and more attention. Being derived from biomass with food grade quality, the first-generation bio-oil (bio-ethanol and bio-diesel) is losing its attraction. The second-generation biofuel is produced from agricultural waste, forest waste, energy crops and aquatic plants, and it is emerging as a promising solution to relieve energy and environmental concerns. Sustainable production of fuels and high value chemicals from biomass resources can be established by integration of conversion processes into biorefineries.

As reported in the literature, three general routes can be used to convert biomass into hydrocarbon fuel, including syngas production by gasification followed by Fisher-Tropsch process, bio-oil from pyrolysis or liquefaction followed by catalytic upgrading, and hydrolysis of lignocellulose followed by catalytic processing or fermentation. Compared with gasification and hydrolysis, pyrolysis of biomass integrated with catalytic

upgrading has been cited as the most economical path with simplest cycle [4-5]. Besides cost-effectiveness and efficiency, fast pyrolysis can produce bio-oil in high yields, and retain 70% of energy stored in biomass, therefore fast pyrolysis is attracting great interest in recent years. However, the high energy density bio-oil from pyrolysis cannot be directly utilized as transportation fuel and chemicals. More than 200 oxygenated compounds have been identified in pyrolysis oil [2, 4, 6] and specific composition in bio-oil depends on biomass resources and conditions used. Oxygen content affects properties of heating value, viscosity and acidity in bio-oil, therefore bio-oil must be upgraded via hydrodeoxygenation (HDO), hydrogenation, or other processes before being blended as transportation fuel.

The catalytic upgrading of pyrolysis oil is quite challenging due to the complexity of pyrolysis oil. Zeolite cracking and hydrodeoxygenation are widely accepted catalytic approaches to upgrade bio-oil [2, 4]. Zeolites, like HZSM-5 are used in zeolite cracking to exclude oxygen from pyrolysis oil. Zeolite cracking is operated at 350-500^{o}C and atmospheric pressure without H_2. Despite of these advantages, the application of zeolite cracking is limited due to the lower grade of product oil [2, 7] and high yield of coking [7]. HDO is an alternative path with best potential to upgrade bio-oil. HDO is operated under high pressure hydrogen to remove oxygen as water, leading to high grade bio-oil as crude oil. Conventional hydroprocessing catalysts, such as Co-MoS_2/Al_2O_3 and Ni- MoS_2/Al_2O_3 [8-9], and supported base (Ni, Cu, Co, Fe etc.) [2, 10-15] and noble metal (Pt, Ru, Pd etc.) [9, 11-12, 15-20] catalysts are found out to be active in HDO reactions of phenolic compounds (phenol, cresol, guaiacol etc.) and real bio-oil. One pronounced problem of sulfide catalysts is deactivation. Co-feeding of H_2S into the system can help to avoid it [2], but at the same time it causes sulfur contamination in bio-oil which initially is almost sulfur-free [2, 21]

Supported noble metal catalysts have been widely used in chemical and energy production as well as environmental protection [22]. Unlike metal sulphides, supported metal catalysts do not require the addition of sulfur to maintain stability and activity. The metal used as hydrogenation catalysts are not prone to coking as are zeolites. Prior studies have shown that supported metal hydrogenation catalysts can hydrogenate and deoxygenate phenolic compounds [1-2, 23]. For example, supported metal catalysts (Pt/SiO_2, Ru/SiO_2, Pt/Al_2O_3, Ru/Al_2O_3, Pt/C, Ru/C, etc.) can be used to upgrade bio-oil via hydrodeoxygenation for production of traditional refinery-ready hydrocarbon feedstock. The effect of metal, solvent and mass-transfer on catalytic hydroprocessing of p-cresol as a model compound has been investigated by Wan et. al. [9]. Similarly, Foster et. al [12] studied the effect of acid functionalized support and metal function for m-cresol hydrodeoxygenation. Very recently, the Lercher group investigated the importance of Ni nanoparticle size and distribution on the hydrodeoxygentation of microalgal oil [13]. In Wang's group, Fe based bimetallic catalysts were examined in the gas phase HDO of guaiacol [24-25]. Compared with other cheap metals, such as Ni, Cu and Co, besides the lowest cost, Fe showed a better hydrogen economy: higher oxygen removal percentage with lowest hydrogen consumption; Pd promoted Fe bimetallic catalyst exhibited promising catalytic features: showing a same level of oxygen removal (100%) as Ni-Cu bimetallic catalyst but less aromatic ring saturation [26]. At 350^{o}C, guaiacol conversion was improved from 96% to 100% with Pd promotion on 2wt %Pd-10wt %Fe/C, and the yield of oxygen-free aromatic compounds improved from 6.3% to 25.9%. The enhanced hydrodeoxygenation activity is believed to stem from the presence of Pd which facilitates the reduction of FeOx and modifies Fe, leading to enhanced HDO of phenol. The presence

of Pd may also facilitate H_2 dissociation/oxygen removal. The further hydrogenation of aromatic ring is likely prevented by the preferential adsorption of phenols from Fe's oxygen affinity.

Furfural hydrogenation is one of the important reactions in biomass conversion. Furfural ($C_5H_4O_2$), can be produced from acid-catalyzed hydrolysis and dehydration of hemicellulose in lignocellulosic biomass [27-28], and it is considered as a key platform molecule in biomass conversion. With multiple functional groups, furfural can be catalytically transformed into a variety of valuable chemicals through various routes [29], including furans, alcohols and ketones. Currently, furfural is mainly transformed into furfural alcohol (FAL) or tetrahedralfurfural alcohol (THFAL) which are widely used as solvents [30].

Another possible product in furfural conversion is cyclopentanone. Cyclopentanone (CPO), a cyclic ketone, is a key intermediate chemical in the production of pharmaceuticals, fragrances and cosmetics, rubber chemicals and agrochemicals. CPO is traditionally produced from is prepared by catalytic vapor-phase cyclisation of 1,6-hexanediol or adipic esters [31], or liquid-phase oxidation of cyclopentene with nitrous oxide [32]. Driven by the rapid growth of pharmaceutical industry, the global demand for cyclopentanone market was valued at USD 100.0 million in 2014, and is expected to reach USD 130.0 million in 2020 [33]. As one of the downstream products of furfural hydrogenation, the production of CPO from biomass based FFA might be an efficient way to expand the industrial application of biomass.

FFA conversion has been widely reported in literature, including decarbonylation/hydrodeoxygenation to furans [34], hydrogenation to alcohols [35-36] and

rearrangement to ketones [37]. At 220°C, 53% yield of furans was observed on 3%Pd/C after 5 hours in isopropyl alcohol, including 20% of tetrahydrofuran (THF), 20% of methyl furan (MF) and 13% of methyl tetrahydrofuran (MTHF) [38]; the production of THF is via decarbonylation of furfural to furan (FN), followed by ring hydrogenation [38]; and MF is believed to be produced from hydrodeoxygenation fof furfural and further ring hydrogenation forms MTHF [39]. Product distribution was greatly affected by temperature [40]: the selectivity of furans (MF+FN) increased from 8.1% to 56.4% as tempreature increased from 180 °C to 240°C on 5%Pt/Al_2O_3; The production of MF is investigated in Vohs' work: furfural bonding was significantly altered on the Zn modified-Pt catalyst where the carbonyl C-O bond was weakened and the weak interaction between furan ring and ZnPt surface limited ring hydrogenation to MTHF [41]. Furfural alcohol (FAL) and tetrahydrofufural alcohol (THFAL) were observed on Pd bimetallic catalysts in liquid phase [30, 36, 42]. The total hydrogenation of furfural to THFAL occured on PdNi/TiO_2-ZrO_2 at 130°C with 725 psig H_2, the alteration in products from partial hydrogenated product (FAL) was believed from the bimetallic synergistic effect [30]. Furfural hydrogenation was affected by solvent polarity: the high polarity of water facilited furfural hydrogenation [42] and the selectivity towards THFAL was enhanced in ethanol, followed by dioxane and toluene, which is in the same trend of polarity order [30]. The mechanism of furfural ring arrangement to CPO was proposed to be consisting of steps: partial hydrogenation of furfural to FAL and subsequent conversion to CPO or THFAL [43-44]. The selectivity to CPO showed a vocanol-shape trend as temperature increased from 140°C to 200°C on Cu-Co catalysts, meanwhile the further hydrogenation of CPO to cyclopentanol (CPL) was improved [44]; and higher hydrogen pressure also favored hydrogenation of CPO to CPL,

together with total hydrogenation of furfural to THFAL [44]. The effect of solvents on furfural transformation to cyclopentanone has been studied in Hronec's work [37]: furan ring rearrangement wasn't observed on noble metal catalysts in alcohol but in water. Furfural was selectively transformed into CPO on 6.8 nm Pd-Cu/C bimetallic catalysts [43]; CPO yield was improved from 73.1% to 92.1% as Cu loading increased from 3% to 10%; the first step was facilited on Pd-Cu^{+} sites, and the yielded FAL wan then rearranged to CPO accelarated by the concentration of hydrogen ions from water dissociation.

Since pyrolysis produces bio-oils having up to 30 vol% water, HDO catalysts must not only be active and selective, but also stable under hydrothermal conditions. Besides, to maintain the liquid phase, high pressure is necessary when operating above the boiling point of water. The converntial supports utilized in catalysis field such as Al_2O_3, SiO_2 which are unstable under such hydrothermal conditions due to the fact that increased amount of H^{+} and OH^{-} ions can attack the surface of the supports leading to severe change in the support, such as surface area loss, pore structure collapse which is undesirable for catalytic performance. Therefore, it is necessary to enhance the supports' hydrothermal stability to be suitable for aqueous phase biomass conversion.

Currently, there are four strategies to improve hydrothermal stability in heterogenous catalysis: introduction of heteroatoms into support, deposition of thin layers onto support, deposition of oxide particles onto carbon and surface modification by functional groups.

It has been reported that hydrothermal stability can be improved by doping heteroatoms such as La^{3+}, Ga^{3+}, Sm, Ce, Ti^{4+}, Zr and Al [45-51]. The hydrothermal stability of aluminosilicate was markedly enhanced by the incorporation of Al into mesoporous

SBA-15 matrix. The hydrolysis of Si-O-Si was impeded by the formation of more stable Si-O-Al [52]. The amount of Al being introduced greatly affected stability: in Huber's work [53], the least amount of Al (Si/Al = 40.1) provided the better protection on MCM-41 than Si/Al = 8.5 and 23.1 in boiling water. It was suggested that Al incorporated onto the surface/near surface region of the pore walls provided the greatest protection. Tetrahedral Al creates a net negative charge in the framework, which repels OH^- ions that accelarates siloxane hydrolysis [48].

A Nb_2O_5 layer was deposited onto SBA-15 by atomic layer deposition in Datey's group [54]. The amount of Nb_2O_5 can be controlled by ALD cycles. These mesoporous niobia materials were proved to be superior stability in liquid water at 200°C; Another a simple and inexpensive approach to strengthen stability of oxides is to coat a carbon layer derived from sugars onto the base support. With 10 wt% carbon, mesoporous silica and alumina demonstrated intact structure after 24 hours treatment in water at 200°C [55]. In Coe's research, precursors of carbon were studied [51]: compared with sucrose and furfuryl alcohol (FA), polyfurfural alcohol (PFA) was the most effective carbon precursor to yield carbon coatings to maintain stability in water at 220°C.

Recently, a new method of a deposition–precipitation–carbonization was devised to prepare niobia/carbon composites [56-57]. 8 nm Nb_2O_5 nanoparticles were dispersed onto carbon surface which was proved to be more stable than the commercial Nb_2O_5 HY-340 at elavated temperatures. The enhanced stability of niobia/carbon composites was due to the hydrophobic nature of carbon. In the catalytic evaluation of γ-valerolactone to pentanoic acid, niobia/carbon helped to preserve the Pd dispersion.

The ultimate goal in surface modification is to increase the hydrophobicity of support by indroducing new functional groups or removing unstable functionalityies. The hydrophobic groups hintered support from the hydrolytic attack. Zeolite's stability was improved by hydrophobization with octadecyltrichlorosilane (OTS) [58]. The introduction of OTS didn't change the acid sites in zeolites and makes it more suitable to be utilized in bio-oil upgrading. It is also reported that N-(2-aminoethyl)-3-aminopropyltrimethoxysilane (AEAPS)-functionalized SBA-16 materials can change the properties of the support showed superior hydrophobicity to the pure SBA-16 support [59].

The above studies are more focused on the process of biomass conversion (temperature, pressure, solvents etc.). Catalysts being used in those studies are typically either commercial or by dry impregnation, which give around 5 nm or even larger metal particles. In this work, catalysts optimization is the focus. Catalysts are fabricated to yield ultra-small metal particles by a simple and reproducible method: Strong Electrostatic Adsorption (SEA).

1.2 Catalysts synthesis

Various methods have been developed for both monometallic and bimetallic catalysts. The catalytic performance of catalysts is closed related to the methods of catalyst synthesis. Impregnation [60], deposition-precipitation [61], strong electrostatic adsorption [62] and redox reactions [63] are the most commonly-used methods.

1.2.1 Impregnation

The most prevalent catalyst preparation method in literature and in industry is dry impregnation (DI), also named as pore filling. In this method, metal precursor in pore volume of solution is impregnated to the dry support powder. This method does not

guarantee either strong metal-support interaction or homogenous metal deposition. However, DI process is the quickest, simplest and least expensive method of catalyst preparation with no loss of metals.

The second common impregnation is wet impregnation (WI) where support is immersed in an excess volume of solution containing the metal salt precursor. Compared with DI method, WI is a much slower process involving diffusion of metal precursor into pores in support which takes several hours to reach equilibrium. Precursor crystallization might happen during water removal by evaporation which can cause waste of metal precursor and metal precipitation.

There are two methods for bimetallic catalysts synthesis by impregnation method: co-impregnation and successive impregnation. In co-impregnation, simultaneous impregnation of both active metal precursor components occurs. Successive impregnation consists of two steps where the impregnation of first metal salt on a support is applied, followed by impregnation of second metal on the monometallic catalyst. Due to the lack of strong interaction between precursors and support, the poor mixing between two metal precursor components is usually observed. These catalysts are not true bimetallic catalysts, to be specific, but a wide range of materials with a rather random distribution of monometallic and bimetallic particles which are normally large in size.

1.2.2 Precipitation-deposition

The deposition-precipitation (D-P) method is a process in which the selective precipitation of a soluble metal precursor onto support is induced by addition of precipitating agent. The most commonly used agents are sodium hydroxide [64-65] and urea [63, 66]. The precipitating agent must be added gradually into the metal precursor containing

solution to maintain a homogenous concentration of hydroxyl ions which can avoid metal precipitation in the solution. The D-P method presents a higher reproducibility with the nanoparticles synthesized showing a tighter size distribution than impregnation method even at higher metal loadings. For example, when utilizing urea as the precipitating agent, metal loadings up to 8% Au/TiO_2 had an average particle size as small as 1.8 nm [67-68]. The slow decomposition of urea at elevated temperature helps to evenly disperse OH^-, and the pH gradient in the solution is minimized, therefore metal hydroxide deposits on the support. In preparation of bimetallic catalysts, two metal salts can be precipitated simultaneously or sequentially on the support. However, this method is problematic, same as impregnation, in terms of surface composition in bimetallic catalysts.

1.2.3 Strong electrostatic adsorption (SEA) and charge-enhanced dry impregnation (CEDI)

SEA is columbic in nature and can be achieved with precise pH control [69]. Oxide surfaces terminate in hydroxyl groups which can be protonated or deprotonated as a function of solution pH. At these conditions the strong interaction between the charged support and metal precursor of opposite charges via electrostatic force can be established. Anion precursors will adsorb over a protonated surface below the point of zero charge (PZC), similarly, cations will adsorb over a deprotonated surface above the PZC. With the strong interaction, the metal migration is limited to minimum extent during thermal treatment, resulting in small metal particles. SEA has been successfully applied to synthesize highly dispersed metal nanoparticles (1-2 nm) on a variety of oxides and carbon supports [3, 70-72]. The procedure of a typical SEA experiment is presented as in Fig. 1.1.

The pH of bulk solution in contact with support is acidified or basified to stay away from the PZC of support to generate electrostatic adsorption; as the pH is enhanced, more

metal precursors are adsorbed on the support by electrostatic interaction. The optimal pH to achieve the maximum uptake can be located in metal uptake survey. The amount of metal being adsorbed is determined as the difference between initial (pre-adsorption) and final (post-adsorption) metal concentration C_i and C_f ppm by ICP-OES: (Molecular weight M = MWM, surface loading = SL)

$$\text{Metal uptake in } \mu\text{moles/m}^2 = \frac{(Ci-Cf)[\text{ppm}]\times 1000\ \text{MWM}}{\text{SL}\ [m^2/\text{liter}]},$$

$$\text{SL}\ [m^2/liter] = \frac{\text{Surface Area of support}\ [m^2/\text{g}]\times\text{grams of support[g]}}{\text{Volume of Precursor Solution[liter]}}$$

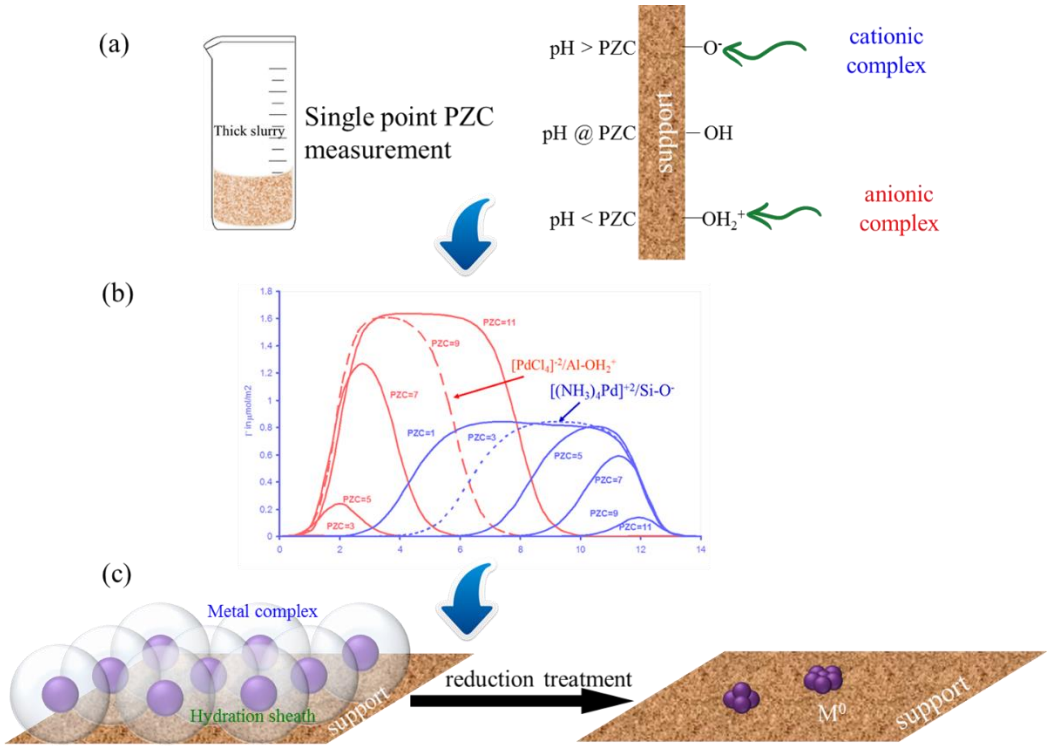

Figure 1.1 Steps of SEA synthesis: a) PZC measurement of support by single point method and precursor determination; b) location of optimal pH in metal uptake survey, c) precursor adsorption with hydration layers over oppositively charged support in synthesis at optimal pH determined from b) and highly dispersed metal particles over support after thermal reduction.

The metal uptake capacity is assumed to be a steric maximum, which is dictated by the closed packed geometry of metal ion precursor retaining various numbers of hydration sheaths (Figure 1.1c). It is generally suggested that cationic and anionic metal precursor ions retain two and one layers of hydration respectively. Cationic precursors such as $Pt(NH_3)_4^{2+}$ and $Pd(NH_3)_4^{2+}$ retaining double hydration sheaths exhibits a maximum adsorption capacity of ~0.84 mol/m^2 [62]. On the other hand, anionic precursors, $PtCl_6^{2-}$ and $Ru(CN)_6^{4-}$ retain a single hydration sheath and hence the maximum uptake is around 1.6 mol/m^2 [62]. At extreme pH values, however, adsorption is retarded by high ionic strength [62, 70-71]. After drying and reduction, well dispersed metal nanoparticles are derived via this method due to the initial strong precursor-support interaction.

Recently, a simple way to synthesize supported metal catalysts with high dispersion was demonstrated, called Charge Enhanced Dry Impregnation (CEDI) which is essentially the same concept as SEA[73-75]. CEDI combines the simplicity of dry impregnation with the high dispersion rendered by SEA [70, 72, 76-80]. The normal procedure for dry impregnation (also known as incipient wetness or pore filling impregnation) is followed, except that the impregnating solution is acidified or basified to cause an electrostatic interaction between the support surface and the oppositely charged metal precursor. The amount of acid or base need to overcome the buffering effect of the support surface is surprisingly large [74, 81], for example, at DI conditions to obtain the optimal final pH of 11 over alumina, an initial pH of 13.5 must be employed [80]. CEDI-synthesized Pt particles over alumina, silica, and titania are less than 1.5 nm in diameter (the XRD limit of detection) [75].

Bimetallic catalysts can be also prepared by either simultaneous SEA (co-SEA) making alloy catalysts or sequential SEA leading to core-shell structure. Rendered by the

advantages in SEA method, SEA-prepared bimetallic catalysts present close intimacy between two metals [82-83]

1.2.4 Electroless deposition (ED)

Another method to make core-shell bimetallic catalysts is electroless deposition (ED), through which a shell metal is deposited in partial or multi-monolayers on a core metal. It is typically an aqueous bath maintained at a predetermined pH containing a secondary metal precursor, a reducing agent (Hydrazine (N_2H_4), formaldehyde (HCHO), hypophosphite ($H_2PO_2^-$), and dimethylamine borane (DMAB) are commonly used reducing agents [84], an optional complexing/stabilizing agent [85]. A supported monometallic catalyst is used as the seed or base catalyst for following ED process. Placing a second metal exclusively as a partial shell on a first metal core offers the ability to synthesize true bimetallic surfaces with no particles of each of the monometallic components. ED proceeds catalytically or autocatalytically whereby a shell of controllable coverage of metal can be deposited selectively onto pre-existing core particles (or seed nuclei) of a pre-existing metal. The solution phase reducing agent only activated on the surface of metal particles, therefore, deposition of secondary metal is targeted onto the base catalyst particles or itself. By controlling the base catalyst, secondary metal ion source, reducing agent, bath temperature, and pH, multiple bimetallic catalyst systems, such as Cu−Pd [86], Ag−Pt [87], Pt−Co [88], Au−Pd [84, 89], and Ag−Pd [90] were successfully synthesized.

The objective of this work is to optimize catalytic performance by tuning the noble metal particle size, controlling surface composition and increasing the hydrothermal stability of support using the rational catalyst synthesis methods outlined above.

Chapter 2

Experimental methods

2.1 Catalysts preparation

Four different commercial powder supports were utilized as recieved. Chemicals include metal precursors, acid/base (pH adjustment). Details are presented in the following Table 2.1.

2.1.1 Catalysts by SEA

a) PZC determination

Deionized water was added to incipient wetness of 2 grams support in a 50 mL centrifuge tube. A spear-tip pH meter was used to measure the pH of the thick slurry.

b) Uptake surveys

Metal uptake-pH surveys were carried out in 60 mL polypropylene bottles containing 55 mL of 200 ppm precursors, with initial pH adjusted in the range of 5 to 13 by HCl and NaOH (NH_4OH for base metal precursors: NiHA, CuTA and CoHA). 5 ml solution was taken out for later ICP analysis ($C_{metal,initial}$). The amounts of supports were added to achieve a constant surface loadings (500 or 1000 m^2/L). Taking as received SBA-15 (SA=710 m^2/g) as an example, $m\ (g) = \frac{1000\frac{m^2}{L} \times \frac{50\ L}{1000}}{710\frac{m^2}{g}} = 0.0704g$.

After adding supports into metal precursor solutions, they were placed on an orbital shaker for 1 h to ensure adsorption equilibrium. Final pH values were recorded

and 5 mL solution was filtered for ICP analysis ($C_{metal,final}$). The metal surface density, Γ, is calculated as: $\Gamma(\frac{\mu mol}{L}) = \frac{(C_{metal,initial} - C_{metal,final})(\frac{\mu mol}{L})}{SL\frac{m^2}{L}}$.

Table 2.1. Summary of chemicals and materials.

Commercial name	Formular/abbr.	Supplier
Hexaammineruthenium (III) chloride	$Ru(NH_3)_6Cl_3$/RuHA	Sigma Chem Co.
Potassium hexacyanoruthenate(II)	$K_4Ru(CN)_6$/RuHCN	Sigma Chem Co.
Tetraamineplatinum(II) chloride	$Pt(NH_3)_4Cl_2$/PTA	Sigma Chem Co.
Chloroplatinic(IV) acid	$H_2PtCl_6.6H_2O$/PtHC	Sigma Chem Co.
Tetraaminepalladium(II) chloride	$Pd(NH_3)_4Cl_2$/PdTA	Sigma Chem Co.
Hexaamminecobalt(III) chloride	$Co(NH_3)_6Cl_3$/CoHA	Sigma Chem Co.
Tetraamincopper(II) chloride	$Cu(NH_3)_4(SO_4)_2$/CuTA	Sigma Chem Co.
Copper(II) nitrate	$Cu(NO_3)_2$	Sigma Chem Co.
Potassium copper(I) cyanide	$KCu(CN)_2$	Sigma Chem Co.
Nickle(II) nitrate hexahydrate	$Ni(NO_3)_2$	Alfa Aesar
Sodium chloride	NaCl	Fisher Scientific
Citric acid	$C_6H_8O_7$	Sigma Chem Co.
Hydrochloric acid	HCl	Sigma Chem Co.
Sodium hydroxide	NaOH	Ricca Chemical Co.,
Ammonium hydroxide	NH_4OH	BDH, 5N
Aerosil 300	SiO_2	Evonik
Sba-200	Al_2O_3	Sasol
Hombikat N100	TiO_2	Sachtleben
Timrex	C	Sachtleben

c) Catalysts synthesis and characterization

2 grams of catalysts were prepared under the same conditions where the maximum uptake occurred in the uptake surveys. When synthesizing the Pd bimetallic catalysts by SEA, a solution containing two metal precursors in a certain molar ratio was first prepared, NH_4OH was used to adjust the pH in the solution. The excess solution was removed by vacuum filtration and the wet slurry were then dried overnight at 100°C in oven and reduced in the flow of 20% H_2/He at optimal temperature determined in temperature-programmed reduction for 1 hour.

2.1.2 Catalysts by CEDI

The Pt loading in CEDI prepared catalysts were determined by maximum uptake with surface loading as high as 25,000 m^2/L to make sure metal adsorption was electrostatic. PTA-OH or PTA-NO_3 was dissolved into a pore volume's worth of 1M NH_4OH. Sodium chloride (NaCl) was added into the solution to achieve Cl^- loadings from 0.1 to 1 wt%. After thorough mixing, the thick slurries were oven dried at 85°C for 2 hours to evaporate excess water. The dried powder was then reduced for 1 hour in 20% H_2/He at 350°C (300°C for carbon catalysts to avoid methanation), using a ramp rate of 5°C/min.

2.1.3 Catalysts by DI

Equivalent metal loadings using the same precursor as in SEA were prepared by conventional dry impregnation (DI) (also called o incipient wetness impregnation or pore filling). The precursors were dissolved into the quantity of deionized water needed to just fill the pore volume of 2 grams of support. The thick slurry was dried overnight at 100°C in air and reduced in a flow of 20% H_2/He at the same temperature as its SEA counterpart for 1 hour.

2.1.4 Pd/Cu/SiO_2 catalysts by ED

The SEA prepared 1.3% Pd/SiO_2 was utilized as the seed catalyst. In a typical electroless deposition of Cu, 0.4 g seed catalyst was placed in 100 mL $KCu(CN)_2$ containing- solution, diluted reducing agent (hydrazine, H_4N_2) was pumped into the solution constantly in one hour period. The whole process was performed around pH 9.5 at room temperature. Small aliquots of the bath were withdrawn and syringe-filtered at 20 min intervals and then analyzed. The residue reducing agent was rinsed off by 2 liters of deionized water. The amount of Cu deposition was controlled by the initial concentration of Cu in the ED bath. Catalysts were air dried at 100 ^oC overnight after ED.

2.2 Catalyst characterization

2.2.1 pH probe meter

A standard pH electrode (Orion 3-star benchtop) was used and calibrated by 3-point calibration with three HACH color-coded pH buffer solutions (pH = 4.0, 7.0, 10.0). Acceptable electrode slope was set to be 95% or higher. For measurement of PZC of the support, a spear-tip pH meter from Fisher Scientific was used to measure the pH of the thick slurry, and the calibration process is same as Orion 3-star benchtop.

2.2.2 N_2 physisorption (BET surface area and pore size distribution)

BET surface area measurements were obtained using an automated adsorption system (ASAP, 2100, Micromeritics). 0.2 grams of support powder was first degassed at 150^oC, 10^{-3} Pa. After being transported from degassing port to analysis port, the sample was charged by N_2 at 77 K with relative pressure ranging from 0~0.99. The BET specific surface area was evaluated using the linear relation between P/P0 and 1/ [V/ (P/P0-1)] with

8 points from 0-0.35 of P/P0 values. And pore size distribution was plotted as d(V) vs dlog (D) based on the desorption branch.

2.2.3 Inductively coupled plasma optical emission spectrophotometry (ICP-OES)

Metal concentration before and after SEA were measured by ICP-OES from PerkinElmer. Metal uptake and loading were calculated from the difference between initial and final concentration. During ICP analysis, a 5ppm Y solution was used as internal standard. Mn solution was used for optical alignment. Three concentrations of standard metal solutions (0, 200 and 500 ppm) were utilized for concentration calibration. Analysis for each sample was repeated 3x times using an auto-sampler. Acceptable goodness of fit for calibration was set to be ≥ 0.999. A quality check (QC) was performed with a 200 ppm standard solution after calibration and the acceptable limit of error in concentration for QC was set at $\leq \pm 10\%$. Besides, QC was set every 10 analysis. If the error was beyond the limit, metal concentration would be recalibrated.

2.2.4 Temperature program reduction (TPR)

TPR was performed on Micromeritics AutoChem II 2920 with a thermal conductivity detector. Samples were first dried in He at 120^{o}C for 1 hour to remove moisture. TPR analysis was run in 10% H_2/He and TCD signals were recorded from 40^{o}C to 800^{o}C with a ramp rate of 5^{o}C/min.

2.2.5 X-ray diffraction (XRD)

Powder XRD analysis was carried out on a Rigaku Miniflex-II with a silica strip detector (D/teX Ultra) with Cu Kα radiation ($\lambda = 1.5406$ Å), operated at 15 kV and 30 mA. Scans were made in the 20°−80° 2θ range, with a scan rate of 2.0° 2θ/min, Pt diffractions

were fit on the software of Fityk using Gaussian to achieve FWHM values. Metal particle sizes were calculated by Scherrer equation with a shape factor of 0.94.

2.2.6 Pulse chemisorption

Chemisorption measurements were also carried out with the Micromeritics Autochem II 2920. Before analysis, all samples were pretreated in situ in flowing H_2 for 2 h at 350°C and then purged with flowing Ar for 30 min before cooling to 40°C in Ar. The catalyst was then contacted with 10% oxygen in helium at 40°C for 30 min to form O-covered Pt species, PtO. After residual physisorbed O_2 being reduced in Ar flow for 30 min, pulses of 10% H_2/Ar were dosed at 4 min intervals until all the surface oxygen reacted with H_2 to form H_2O and Pt−H species. The assumed overall stoichiometry is 0.667 Pt: 1 H_2. Particle sizes were estimated from chemisorption assuming hemispherical geometry.

2.2.7 Scanning tunneling electron microscopy (STEM)

Micrographs of catalysts were acquired using the JEM-ARM200CF STEM (JEOL USA Inc., Peabody, MA, USA). The JEM-ARM200CF is a probe aberration corrected 200kV STEM/TEM with a cold field emission source with 0.35eV energy resolution. And the elemental mappings of bimetallic catalysts were generated using an Oxford Instruments X-Max100TLE SDD detector (Oxford Instruments PLC, Abingdon, Oxfordshire, UK). Approximately 500 particles were counted over a series of images for size distribution for each sample.

2.2.8 X-ray photoelectron spectroscopy (XPS)

XPS measurements were conducted using a Kratos AXIS Ultra DLD XPS system equipped with a monochromatic Al K source. The monochromatic Al Kα source was operated at 15 keV and 150 W, incident at 45° with respect to the surface normal. The pass

energy was fixed at 40 eV for the detailed scans. All Ru $3d_{5/2}$ binding energy (BE) peak positions were corrected using the C 1s binding energy value of 284.2 eV and all peak intensities were normalized to that for the C 1s peak for quantitative comparison.

2.2.8 GC-MS

Gas chromatography–mass spectrometry (GC-MS) is an analytical method that combines the features of gas-chromatography and mass spectrometry to identify different substances within a sample. Products of bio-oil HDO were analyzed by GC-MA. For GC-MS, a small measured amount of sample was collected from the reactor as-is post-reaction and dissolved in 0.05 wt% fluoranthene in acetone, to a known concentration. The dissolved sample was then centrifuged in a microcentrifuge (Fisher Scientific) to remove any precipitated catalyst. The liquid portion removed, and the centrifuged mass was weighed by difference, which was used to correct the liquid concentration for GC-MS analysis.

2.2.9 NMR

Nuclear magnetic resonance (NMR) is a physical phenomenon in which nuclei in a magnetic field absorb and re-emit electromagnetic radiation. Nuclear Magnetic Resonance (NMR) spectroscopy is an analytical chemistry technique used in quality control and reserach for determining the content and purity of a sample as well as its molecular structure. Products of bio-oil HDO were analyzed by H NMR. For NMR analysis, a fixed amount of sample from the reactor as-is post-reaction was dissolved in deuterated methanol. After the entrained catalyst precipitated, the solution was transferred to an NMR tube for analysis.

2.3 Catalysts evaluation

2.3.1 Hydrothermal tests

Hydrothermal stability testing was carried out in a stainless-steel batch reactor with 100mL capacity from Autoclave Engineers with the stirring speed of 1000 rpm. 0.2g of sample with 50 ml of DI water was heated to 220^{o}C at autogenous pressure (22bar) for 24 hours.

2.3.2 Bio-oil hydrodexoygenation (HDO)

Batch hydrodeoxygenation reaction experiments were carried out at USDA-ARS. In each experiment, a certain amount of catalyst and bio-oil were placed in 20 ~ 30g of deionized water in a Parr Series 4598 100 mL bench-top reactor. The detailed procedure was as followed: after catalyst and bio-oil were loaded, the vessel was then sealed tight and flushed 3 times with hydrogen; after charging the vessel with 300 psi hydrogen, the water/catalyst slurry was lightly stirred at 300 rpm while the temperature of the vessel was maintained at 300^{o}C for 1 hour; then the hydrogen reservoir pressure regulator was increased to 1800 psig; around 9g of bio-oil was injected into the reactor, and the mixer speed was increased to 750 rpm; after 3 hours reaction, the primary hydrogen valve was closed off, the heater was removed, and the mixer speed was decreased to 300 rpm; Once the reactor was cooled to room temperature, non-condensable gases were vented into a collection bag and further analyzed; the aqueous phase was decanted from the vessel and centrifuged to remove any partially miscible components; a sample of bio-oil/catalyst product was also collected for direct analysis of the product before the vessel and the reactor parts were washed with acetone to collect any accumulated oil. The acetone

washings were filtered through a 0.45 um PTFE filter to remove the catalyst, and the acetone was removed by rotary evaporation. Experiments were performed in duplicate.

2.3.2 Furfural hydrogenation

The hydrogenation of furfural was performed in a stainless-steel batch reactor with 100mL capacity from Autoclave Engineers with the stirring speed of 1000 rpm. Reactions were run for 3 h at 430 psi H_2 and 150^{o}C in water. Control runs with no catalyst showed negligible reactivity. A given amount of catalyst and 200μL of 1,4-dioxane (internal standard) were added. Prior to the reaction, catalysts were pretreated in 57 grams of water in H_2 flowing at 150^{o}C for 1 h, after which 3.0 g furfural (FFA) was pumped (in 10 s) into the reactor with a high-pressure HPLC pump. Liquid samples (0.25ml) were taken in an interval of 20 min and analyzed by gas chromatography. The Madon-Boudart test was implemented over 3.3% Pd/SiO_2 and 0.7% Pd/SiO_2. XRD showed both samples to have Pd size below 1.5 nm. Turnover frequency was calculated based on 10% conversion of furfural at 150^{o}C and were equivalent (~0.11$^-$s) within experimental error. The similarity of the TOFs at with a five-fold variation in the number of active sites in the same catalyst volume confirms the absence of transport limitations. Reaction rates of catalysts were calculated based on mass of Pd and mass compared at 10% conversion of FFA. Catalytic activity was also reported as turnover frequency (TOF, molecules reacted per site per second) which were estimated from H_2-chemisorption for Pd, and for Cu/SiO_2 which does not chemisorb, from the 1.5 nm size determined from XRD).

Conversion, product selectivity and yield were calculated as:

$\text{Conversion} = 100\% \times \frac{n^0_{FFA} - n_{FFA}}{n^0_{FFA}}$, $S_i = 100\% \times \frac{n_i}{\sum n_i}$ and $Y_i = 100\% \times S_i \times \textit{Conversion}.$

Chapter 3

Synthesis of highly dispersed monometallic catalysts on hydrothermally stable supports by strong electrostatic adsorption, characterization, and evaluation for biomass conversion

3.1 Introduction

Strong electrostatic adsorption was utilized to synthesize ultra-small (about 1 nm) Pt and Ru metal nanoparticles over amorphous SiO_2 and SBA-15 supports; meanwhile, Pt and Ru catalysts were also prepared by conventional impregnation methods. Comparison was made between the two methods. Supported catalysts are used in aqueous phase biomass conversion at high temperature and pressure. Conventional supports such as SiO_2 and Al_2O_3 are unstable under such conditions due to the hydrolysis of support [91]. For example, SBA-15, a type of mesoporous silica which is widely utilized in the field of catalysis with its high surface area and well-ordered pore structure, loses 88% of its original surface area after hydrothermal treatment at 220^{o}C in for water for 4 hours. Therefore, it is necessary to improve the stability of supports in water to achieve better catalytic performance.

Four types of supports were employed in this study: silica supports were stabilized by two methods; first, the introduction of heteroatoms (Zr, Al) to impede hydrolysis of silica, and second, the deposition of thin carbon layers on the support surface. Third, a mesoporous alumina was prepared, and the fourth was carbon, known to be stable in hydrothermal conditions but also generally recognized to be less selective to desired HDO

products. These supports were first tested in a moderately rigorous hydrothermal environment of 220°C and 360 psig, and then under reaction conditions at 300°C and 1800 psig. Support stability was determined by the surface area measurements before and after tests. The ability of the supports to anchor the metal nanoparticles against sintering and in the case of bimetals, dealloying was also studied.

The most stable and best anchoring oxide support was found to be mesoporous alumina. Noble metal (Pt and Ru) single and bimetallic catalysts as well as base metal (Cu and Ni) single and bimetallic particles were synthesized on this support, and to compare the effect of support, the base metal catalysts were also prepared over a carbon support. These series of catalysts were tested at the USDA-ARS research center in Philadelphia for HDO of hardwood-derived bio-oil.

3.2 Results and discussion

3.2.1 Synthesis and characterization of highly dispersed Ru and Pt nanoparticles on silica

SBA-15 was prepared as reported [92]. Ruthenium hexaamine chloride ($[Ru(NH_3)_6]Cl_3$, 99.9%) and platinum tetraamine chloride ($[Pt(NH_3)_4]Cl_2$, 99.9%) obtained from Aldrich which are designated as RuHA and PTA respectively were used as ruthenium and platinum precursors. Stock solutions of 200ppm Ru or Pt were prepared. The PZC of SiO_2 support was determined as 4.4, the procedure was such: deionized water was added to incipient wetness of 2g SBA-15 in a 50 mL centrifuge tube. A spear-tip pH meter was used to measure the pH of the thick slurry.

The PZC of SBA-15 was determined to be below 7, thus, cation metal complexes such as platinum tetraammine chloride (PTA) and ruthenium hexamine chloride (RuHA) were chosen as precursor. Metal uptake-pH surveys were carried out in 60-mL

polypropylene bottles containing 55 mL of 200 ppm RuHA or PTA, with initial pH adjusted in the range of 5 to 13 by HCl and NaOH. 5 ml solution was taken out for later Inductively coupled plasma optical emission spectrometry (ICP-OES) analysis ($C_{metal,initial}$).

After adding supports into metal precursor solutions, they were placed on an orbital shaker for 1 h to ensure adsorption equilibrium. Final pH values were recorded and 5 mL solution was filtered for ICP analysis ($C_{metal,final}$). The metal surface density, Γ, is calculated as: $\Gamma(\frac{\mu mol}{m^2}) = \frac{(C_{metal,initial} - C_{metal,final})(\frac{\mu mol}{L})}{SL(\frac{m^2}{L})}$.

Figure 3.1 represents uptake surveys of RuHA/SBA-15 and PTA/SBA-15 for 1000 m^2/L surface loading (m^2 of support per liter of precursor solution) and 200 ppm metal as a function of final pH of solution. The metal uptake is reported as surface density, in $\mu mol/m^2$. SBA-15 followed essentially the same trend as silica [72]. No adsorption occurred below pH 6 as hydroxyl groups are not deprotonated sufficiently. Volcano-shaped plots are observed in the range of pH 6 to pH 13. As pH increases the adsorption of RuHA increase and reaches maximum surface density of 1.6 $\mu mol/m^2$; while in case of PTA maximum surface density of 0.9 $\mu mol/m^2$ is observed. In case of RuHA, the maximum adsorption occurs at pH 11.4. The retardation of adsorption process occurs at pH extremes, caused by high ionic strength, which decreases adsorption equilibrium constant [72]. The same trends are seen in all the other uptake surveys. For the same precursor, similar maximum adsorption can be obtained on different silica supports at the same surface loading. All catalysts were synthesized around the optimal pH followed by temperature programed reduction (TPR) to determine the reduction temperatures. Catalysts were

characterized by X-ray diffraction (XRD) and scanning transmission electron microscopy (STEM) to determine metal particle sizes.

The limit of metal uptake is thought to be steric; a monolayer is limited to a closed-packed arrangement of complexes which retain one or two hydration sheaths. The maximum uptake of PTA is 0.9 μmol/m^2 or 1 complex/ 2 nm^2, which corresponds to the retention of two hydration sheaths by the square planar PTA complex [72]. It appears that the octahedral RuHA complex, which adsorbs at 1.6 μmol/m^2 or 1 complex/nm^2, retains only one hydration sheath.

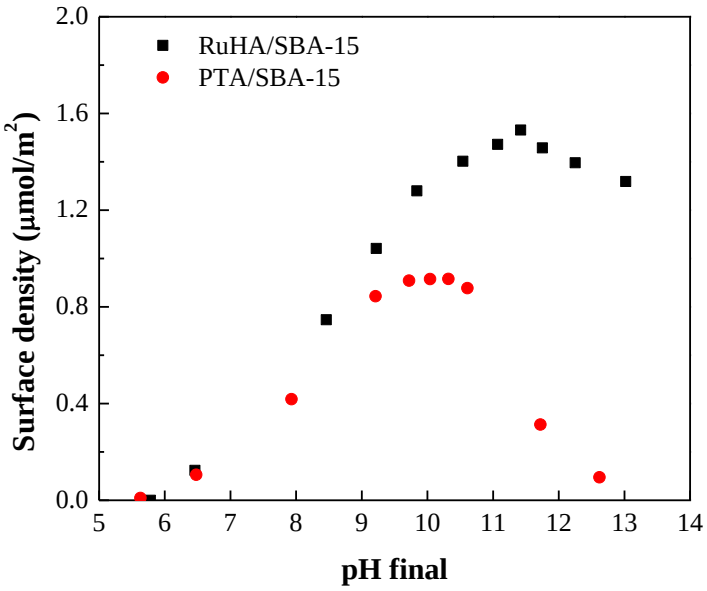

Figure 3.1. Metal surface density vs final pH of solution at 1000 m^2/L: RuHA; and PTA on SBA-15.

Temperature program reduction (TPR) was performed on all filtered and dried SEA samples to determine the temperature of reduction of the metal complexes to metal. The TPR profile (Figure 3.2a) shows two peak for the RuHA complex. The reduction of Ru^{4+} to Ru^0 occurred at around 180°C whereas Ru^{3+} reduces to metallic Ru^0 at 300~350°C.

Hence all RuHA/SiO_2 catalysts were reduced at 300°C to obtain metallic Ru particles on SBA-15. Two reduction peaks were also observed for PTA samples, one at 280°C and another at 350~400°C (Figure 3.2b). Goguet et al. [93] systematically studied the decomposition of $[Pt(NH_3)_4(OH)_2]n$ complex on SiO_2 and suggested that the decomposition steps involve an intermediate complex which anchors to SiO_2 strongly during drying process and then decomposes to Pt^0. All PTA/SiO_2 catalysts were reduced at 350°C.

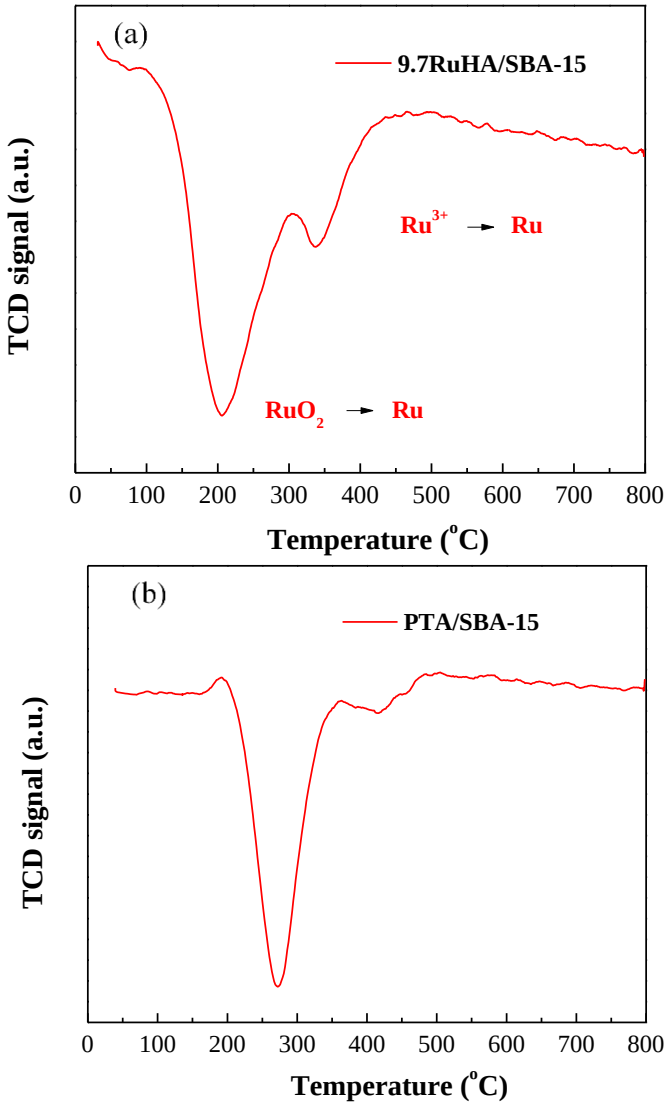

Figure 3.2. TPR profiles of dried a) RuHA/SBA-15 and b) PTA/SBA-15.

Scanning transmission electron microscope (STEM) was used to obtain high-angle annular dark-field (Z-contrast) images for each sample. Figure 3.3 shows typical images for 9.7 wt% Ru and 10.0 wt% Pt particles deposited on SBA-15 prepared via SEA at monolayer adsorption.

The hexagonal pore structure of SBA-15 is seen in some orientations of the sample as dark and bright contrast channels as in Figure 3.3a. Figure 3.3b shows a side view of the hexagonal channels of the Pt/SBA-15 sample. Metal particle sizes of the reduced catalysts prepared by SEA show very narrow size distribution throughout the SBA-15 pore channels. The average particle size for 9.7 wt% Ru/SBA-15 is 1.1 nm ± 0.2 nm, and that of the 10.0 wt% Pt/SBA-15 is 1.3 ± 0.3 nm (Fig 3.3).

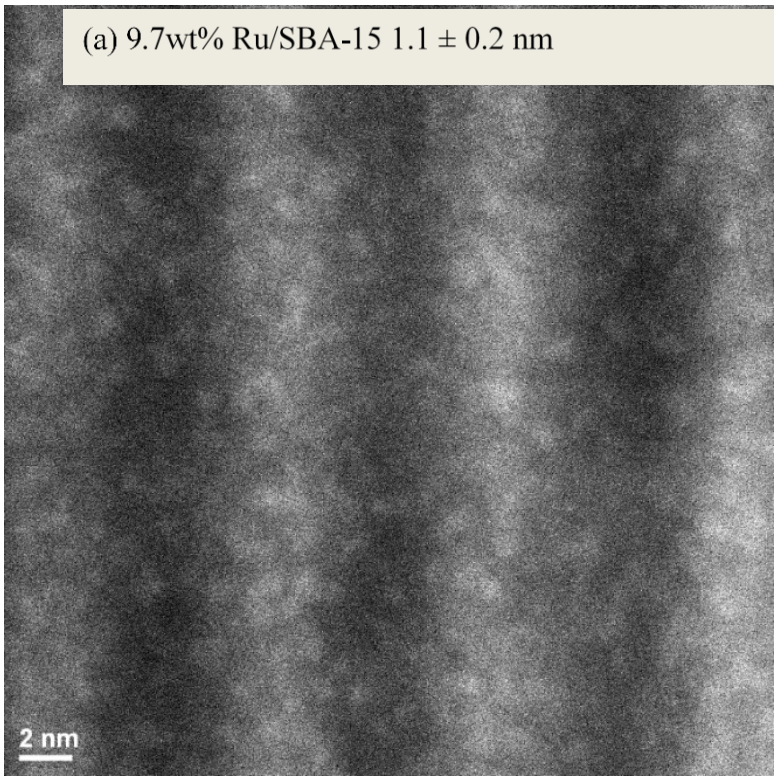

Figure 3.3.a) Representative STEM images and corresponding particle size distribution of Ru/SBA-15; bar scale 2 nm.

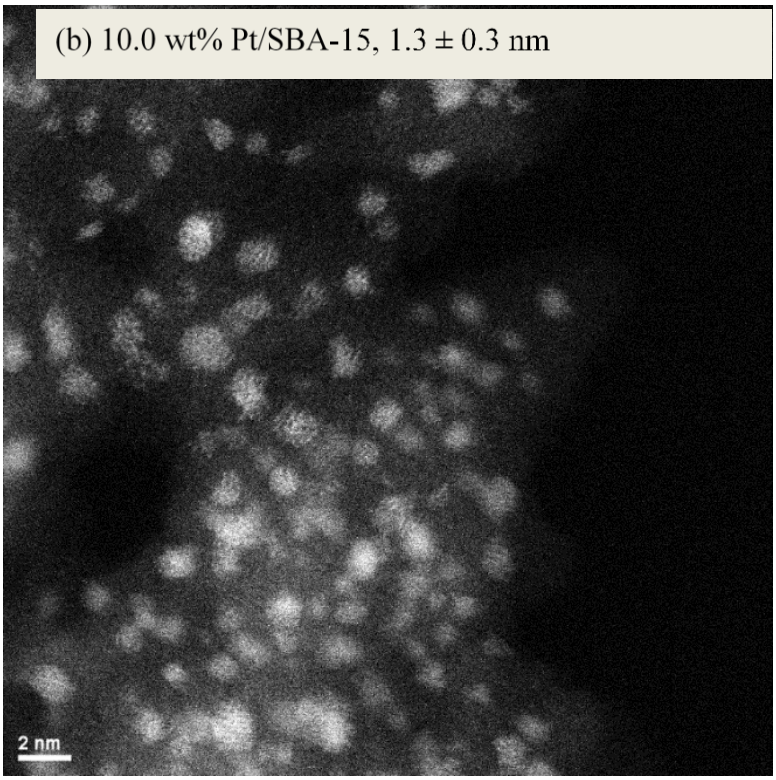

Figure 3.3.b) Representative STEM images and corresponding particle size distribution of Pt on SBA-15; bar scale 2 nm.

3.2.2 Synthesis of Ru and Pt catalysts on hydrothermally-stable supports and their stability tests

It has been reported in literature that introduction of heteroatoms such as Zr, Al, Ti, and Nb can improve the stability of silica in boiling water. In the following experiments, various loading of Zr ranging from 0.92 to 13% were added into silica, 0.33wt% of Al was incorporated into SBA-15 matrix. Carbon coating corresponding to 10wt% carbon from PFA was deposited onto Zr-modified silica. Mesoporous alumina was synthesized as reported in literature with minor modifications. The PZCs and fresh BET surface areas are listed in Table 3.1.

For supports with PZC below 7, RuHA, PTA was used as precursor, and anionic complex, RuHCN, PtHC was used on high PZC support of Al_2O_3.

Table 3.1. Basic properties of various supports.

Hydrothermal supports	PZC	BET surface area (m^2/g)
0.92%Zr-SiO_2	5.6	401
4.8%Zr-SiO_2	5.7	416
13.0%Zr-SBA-15	5.5	558
0.3%Al-SBA-15	3.3	454
10%C-4.8%Zr-SiO_2	3.6	229
Meso-Al_2O_3	8.5	237

a) Zr-SiO2

Typical volcano-shape metal uptakes were seen on Zr-SiO_2 in Figure 3.4. The amount of Zr had no effect on metal adsorption which was consistent with PZC determinations displayed in Table 3.2, the maximum uptakes were 1.43, 1.64 and 1.57 umol/m^2 on 0.93% Zr-SiO_2, 4.8% Zr-SiO_2 and 13% Zr-SBA-15 respectively, and minor variations were observed in optimal pHs as shown in Figure 3.4. 5.3% Ru/0.93%Zr-SiO_2, 5.5% Ru/4.8% Zr-SiO_2 and 6.0% Ru/13% Zr-SBA-15 were synthesized at pH 11.6, 11.9 and 12.2 respectively. These three catalysts were reduced in 20% H_2/He at 300^{o}C for 1 hour before further characterization, such as XRD and STEM.

Ru diffractions were absent in XRD profiles revealing Ru particles of below 1.5 nm in all three catalysts (representative pattern in Figure 3.5a). The minor distortion in the range of 26-38^o in 6.0% Ru/13% Zr-SBA-15 was attributed to the small ZrO_2 patches on silica. ZrO_2 XRD pattern was provided at the bottom in Figure 3.5a. And the existence of dispersed small ZrO_2 in fresh support was proved in the STEM in Figure 3.6.

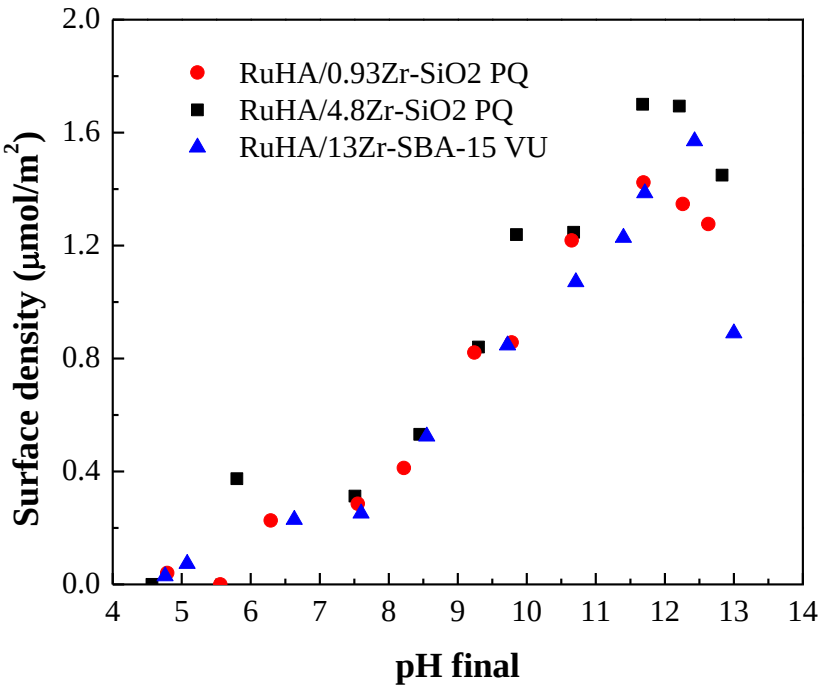

Figure 3.4. RuHA uptake surveys on SiO_2 support with various amount of Zr doping.

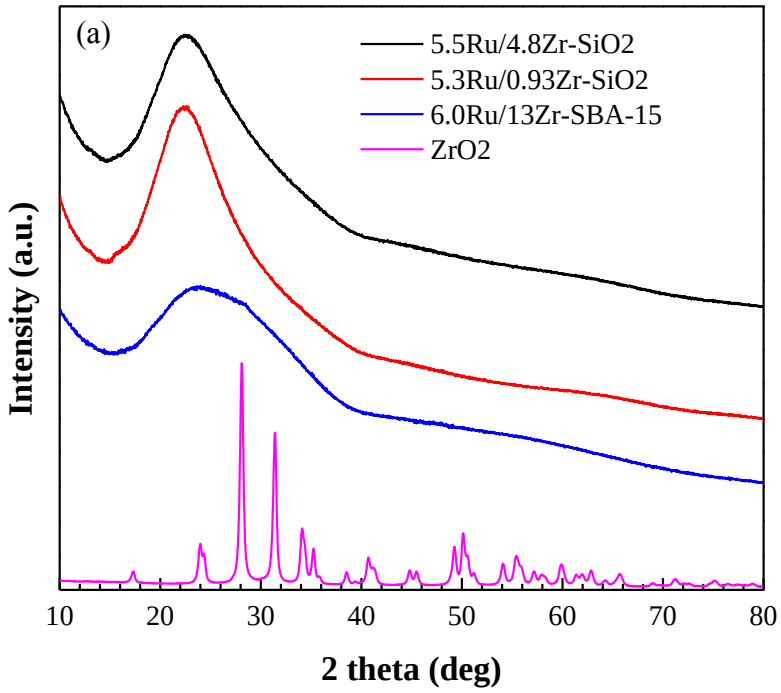

Figure 3.5.a) XRD patterns of fresh Zr/silica supported Ru catalysts.

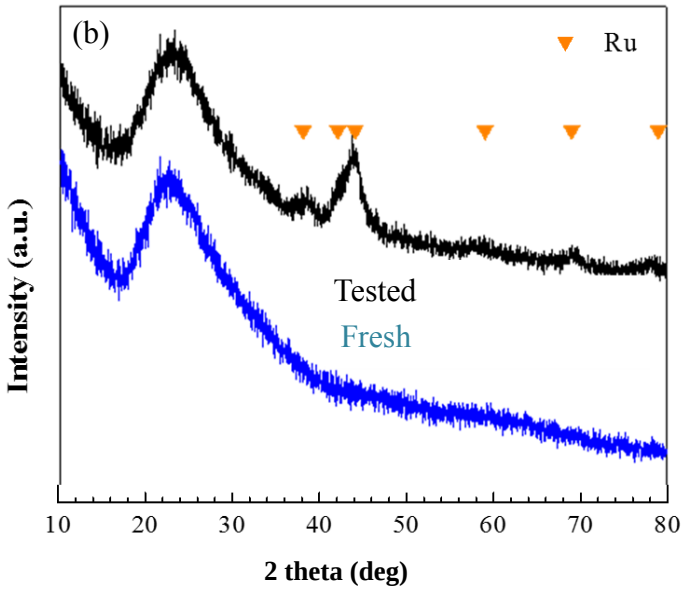

Figure 3.5.b) XRD patterns of spent 5.5%Ru/4.8%Zr-SiO_2.

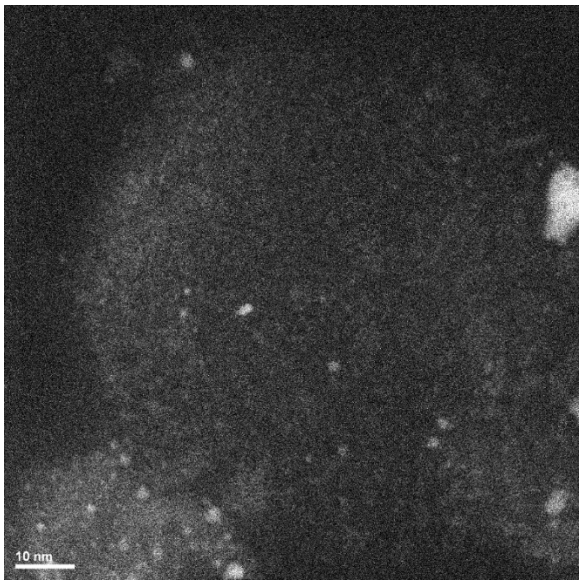

Figure 3.6. A representative STEM image of 13%Zr/SBA-15.

The stability of pure Zr-modified SiO_2 was improved by Zr modification compared to pure silica which lost 90% of its surface area at 220°C for 4 hours. After 16 hours

hydrothermal test in water at 220°C, there was 50% loss in surface area in 4.8%Zr-SiO_2 as measured by BET surface area analysis. However, the metal particle anchoring against sintering was weak: Ru particles sintered from 1.2 nm to 4.2 in 5.5%Ru/4.8%Zr-SiO_2 during 2 hours test at 300°C as shown in Figure 3.5b.

b) Al-SiO_2

The small amount of Al (0.7wt%) introduced in SBA-15 showed no effect on metal adsorption, the volcano-shape of PTA uptake survey was shown in Figure 3.7, with maximum of 0.9 μmol/m^2 at pH value of 10.6 corresponding to 8.1% Pt/ Al-SBA-15. A broad peak centered at 36° was observed in XRD pattern (Figure 3.8) which was indexed as Pt_3O_4. It has been reported that room temperature Pt oxidation occurs very often on small particles. Pt_3O_4 was sized as 1.5 nm based on Scherrer equation. STEM image in Figure 3.9 clearly displayed that homogenous Pt particles were highly dispersed on the support with and average size of 1.3 nm which is in a good agreement with XRD.

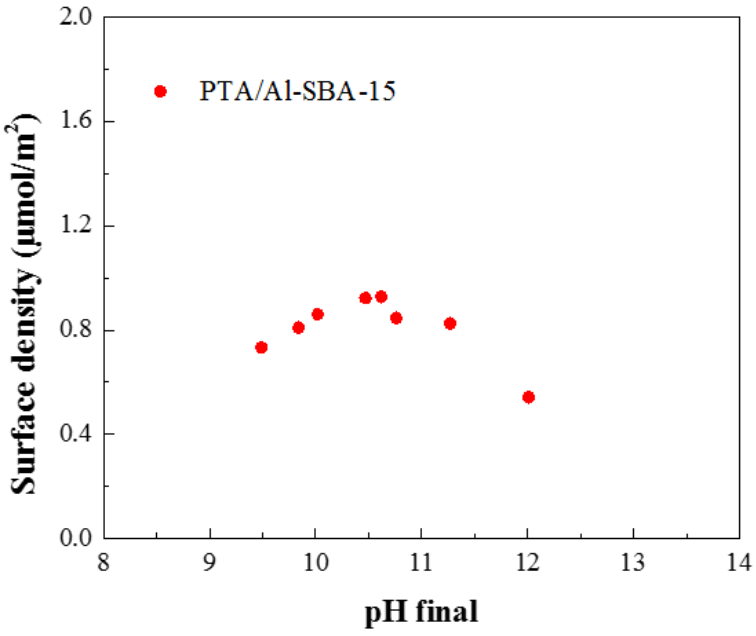

Figure 3.7. PTA uptake survey on Al-SBA-15.

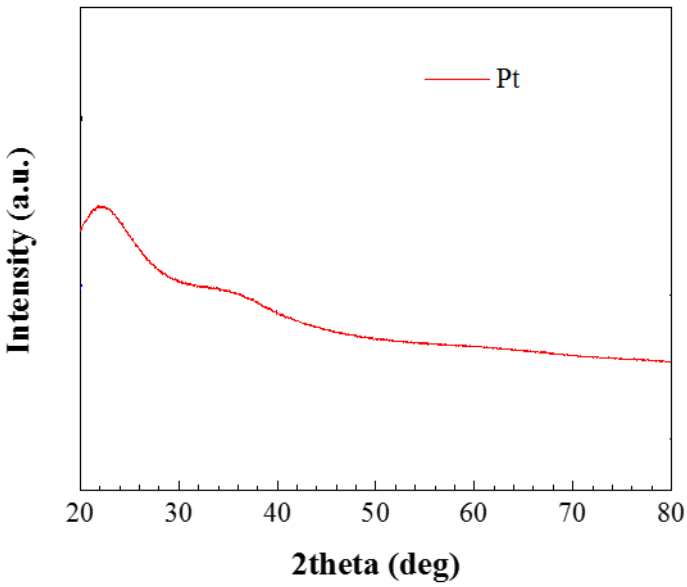

Figure 3.8. XRD pattern of 10%Pt/Al-SBA-15.

The surface area of Al-SBA-15 dropped from 454 to 342 m^2/g (25% loss) after 24 hours hydrothermal tests at 220°C. However, hydrolysis of Al-SBA-15 was accelerated at 300°C leading to complete support dissolution, metal sintering could therefore not be studied.

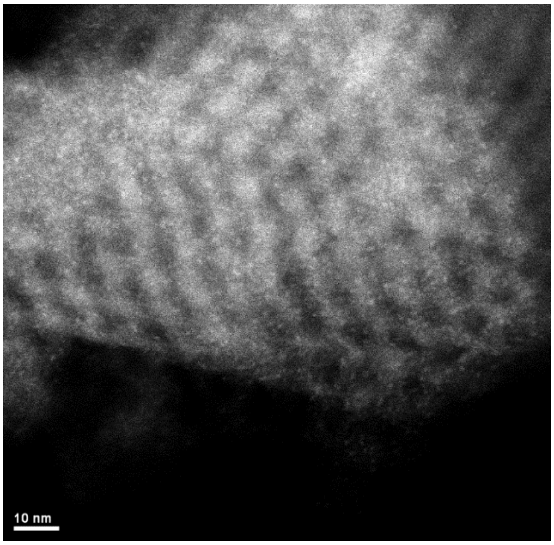

Figure 3.9. STEM of 10%Pt/Al-SBA-15.

c) C-Zr-SiO_2

Based on the metal uptake survey in Figure 3.10, 4.3%Ru/10%C-4.8%Zr-SiO_2 was prepared at pH 12. As revealed in XRD pattern in Figure 3.11, small Ru particles were deposited by SEA method.

10% carbon was coated on the 4.8%Zr-SiO_2 followed by the method in literature [51]. The hydrothermal stability of this support was enhanced by the hydrophobicity of carbon, only 16% loss in surface area at 220°C for 16 hours. Ru and Zr signals disappeared in XPS profiles (Figure 3.12a and b) after treatment 300°C for 2 hours indicating a severe metal leaching in 4.3%Ru/4.8%Zr-SiO_2.

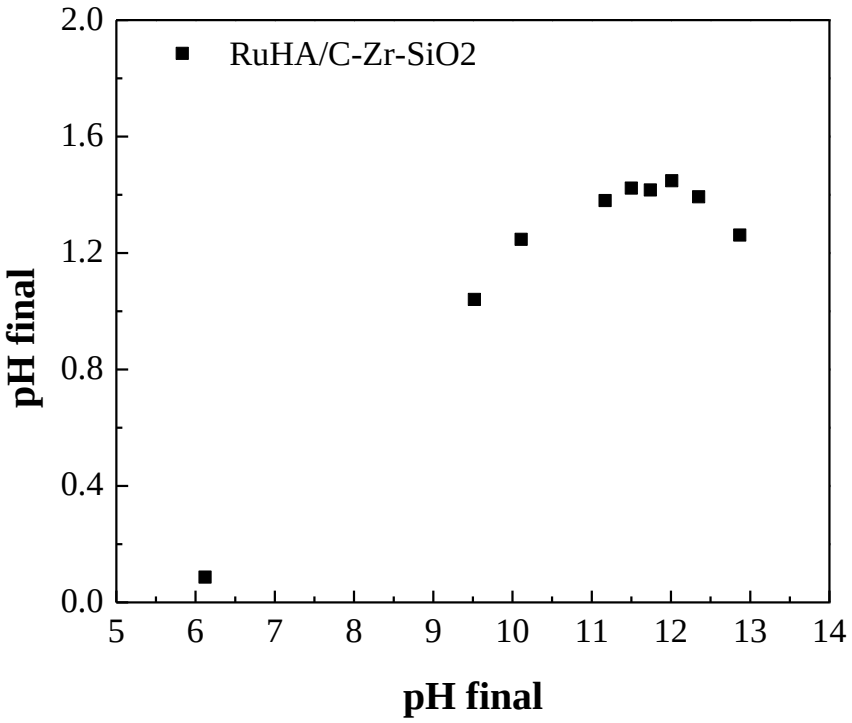

Figure 3.10. RuHA uptake survey on 10%C-4.8%Zr-SiO_2.

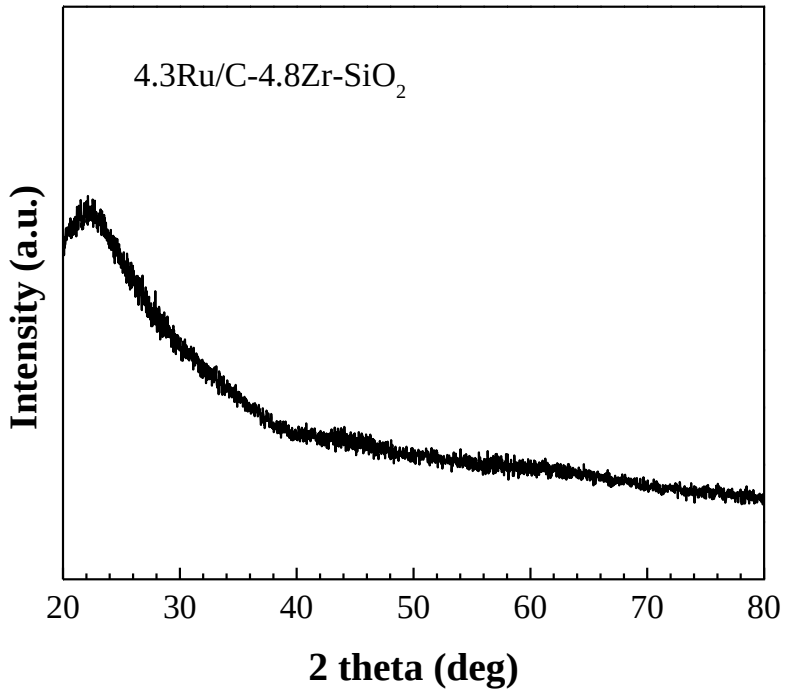

Figure 3.11. XRD of 4.3%Ru/10%C-4.8%Zr-SiO_2.

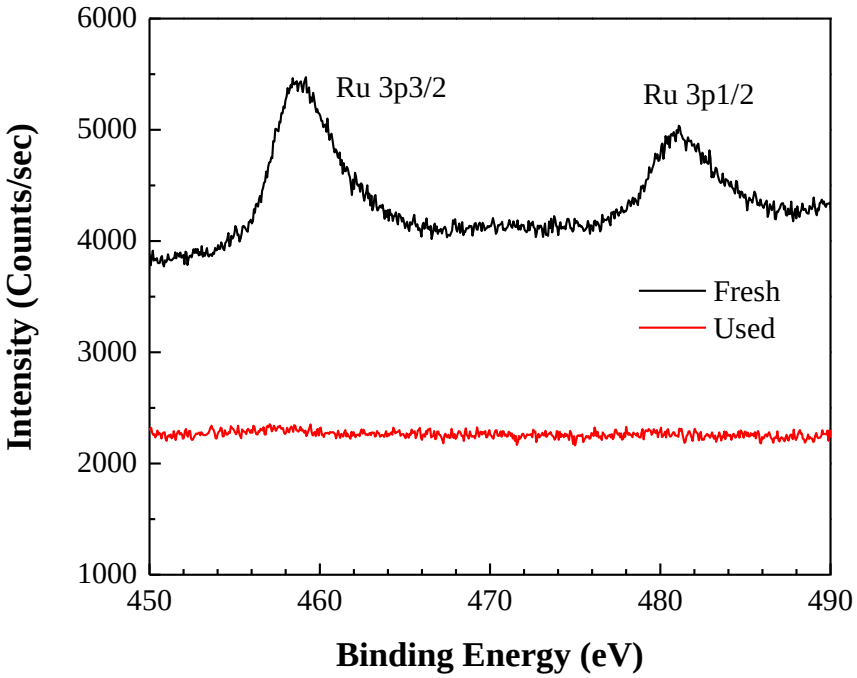

Figure 3.12.a) Ru signal in XPS profile of fresh and spent catalysts of 4.3%Ru/10%C-4.8%Zr-SiO_2.

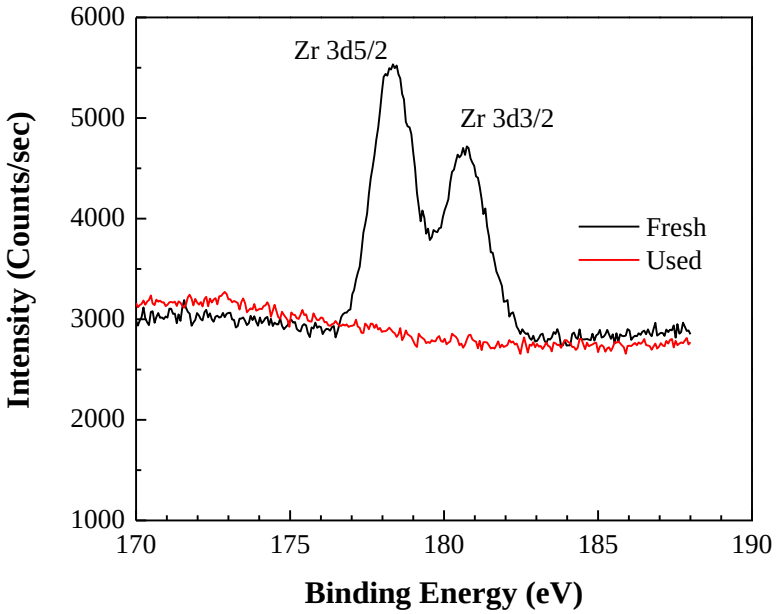

Figure 3.12.b) Zr signal in XPS profile of fresh and spent catalysts of 4.3%Ru/10%C-4.8%Zr-SiO_2.

d) meso-Al_2O_3

For high PZC supports, anionic complexes such as potassium hexacyanoruthenate ($[RuK_4(CN)_6]$) and hexachloroplatinate ($[H_2PtCl_6]$) were used in SEA. The uptake versus pH of 200 ppm anionic platinum hexachloride (PtHC, $[PtCl_6]^{2-}$) and ruthenium hexacyanide (RuHCN, $[Ru(CN)_6]^{4-}$) complexes over 1000 m^2/L alumina support was shown in Figure 3.13, with PtHC displaying the typical volcano shape of Figure 3.13. Monometallic RuHCN and CPA uptake survey on meso-Al_2O_3electrostatically adsorbed precursors with the downturn of uptake at low pH due to high ionic strength [94]. The quadruply valent Ru complex, on the other hand, does not show this downturn, likely due to its higher charge. Fresh single metal Ru and Pt catalysts were also characterized by XRD (Figure 3.14) after being reduced at 500°C and 350°C. In the XRD pattern of the fresh 3.0wt%Ru/m-Al_2O_3 catalyst (Figure 3.14), virtually no difference is detected

compared to pure mesoporous Al_2O_3 support, indicating ultra-small Ru particles have been deposited on the support by SEA. The broad peak observed in the 4.2wt%Pt/m-Al_2O_3 sample (Figure 3.14) is assigned to Pt (111), located at 39.9° 2θ, gives 1.4 nm from the Scherrer equation.

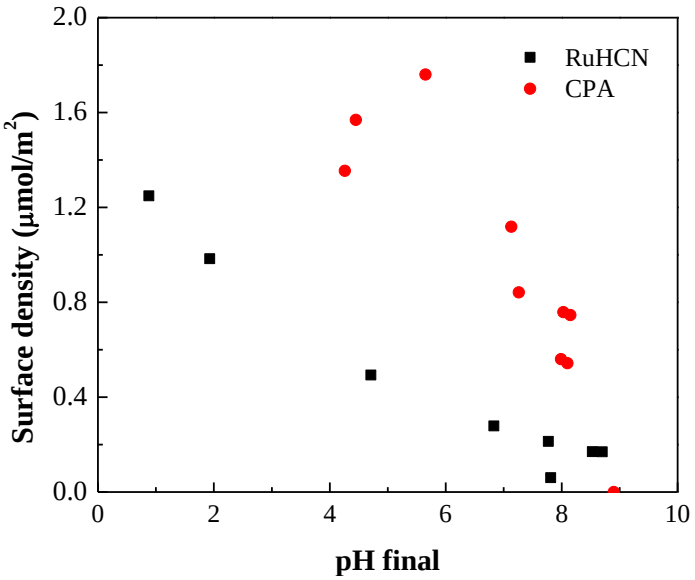

Figure 3.13. Monometallic RuHCN and CPA uptake survey on meso-Al_2O_3.

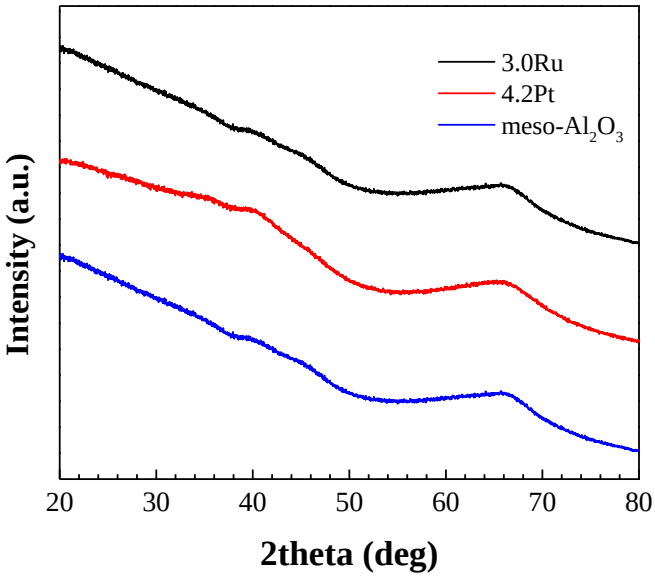

Figure 3.14. XRD of monometallic 3.0%Ru/ meso-Al_2O_3 and 4.2%Pt/ meso-Al_2O_3.

Overall, meso-Al_2O_3 proved to be the most stable support under hydrothermal test (220°C) and reaction (300°C) conditions. While its BET surface area decreased about 20% from 247 m^2/g to 197 m^2/g in the 220 °C test, its surface area appeared to increase by this amount at 300°C to 306 m^2/g. This has been reported in literature [95] and occurs with a transformation of amorphous alumina into to crystalline hydrated boehmite which is believed as the most stable alumina phase in water. This surface also displayed the greatest metal particle anchoring ability; Ru size increased only to 2.5 nm as shown in the Ru deconvolution analysis of Figure 3.15b.

3.2.3 Catalytic evaluation of noble and base metal single and bimetallic hdo catalyst synthesis and evaluation

The meso-alumina support showed superior stability as well as metal anchoring ability under the rigorous hydrothermal conditions of the HDO reaction and was chosen as the support to compare noble metal (Pt and Ru) single and bimetallic catalysts versus base metal (Cu and Ni) single and bimetallic catalysts for the HDO reaction. To confirm the superior selectivity of oxide supports, a parallel set of base metal catalysts was also prepared over a carbon support.

a) Pt and Ru Single and Bimetallic Catalysts on meso-Alumina

For bimetallic catalyst synthesis, when mesoporous alumina was placed in solution containing 100 ppm of each metal precursor (Figure 3.16), the more strongly charged RuHCN was preferentially adsorbed over the PtHC. To achieve a 1:1 atomic ratio of Pt:Ru, the concentrations of Pt and Ru were adjusted to 50 and 25 ppm respectively, which resulted in a simultaneous uptake of 45 and 25 ppm, corresponding to 1.0 and 0.5 wt%. To increase the total metal loading at constant metal ratios, the co-SEA process was repeated after the first deposition of precursors was reduced at 350°C. The second application of

metals resulted in an additional 1.0 wt% of Pt and 0.5 wt% of Ru, for a total weight loading of 2.0 wt% Pt and 1 wt% Ru, in a 1:1 atomic ratio.

XRD patterns in Figure 3.17a (middle 2 patterns) show that PtRu bimetallic catalyst is also very highly dispersed, with no notable difference between 1st and 2nd SEA cycles. Post reaction, the alumina again converts to boehmite and the particle size grows a bit, though the metals are still alloyed at evidenced by the position of the peak at 40.4 º2 , which is between Pt (111) at 39.8 º2 and the Ru (101) at 44.2 º2 . Figure 3.17b shows a deconvolution analysis of the boehmite peak at 38.6 º2 and the Pt rich Pt/Ru alloy (111) peak at 40.4 º2 , which is comprised of small (1.7 nm) and larger (4.8 nm) alloy particles. From an area average of the XRD peaks the overall average size of the particles is 3.0 nm.

When mesoporous alumina was placed in solution together at 100 ppm each (Figure 3.16), the more strongly charged RuHCN was preferentially adsorbed over the PtHC. To achieve a 1:1 atomic ratio of Pt:Ru, the concentrations of Pt and Ru were adjusted to 50 and 25 ppm respectively, which resulted in a simultaneous uptake of 45 and 25 ppm, corresponding to 1.0 and 0.5 wt%. To increase the total metal loading at constant metal ratios, the co-SEA process was repeated after the first deposition of precursors was reduced at 350ºC. The second application of metals resulted in an additional 1.0 wt% of Pt and 0.5 wt% of Ru, for a total weight loading of 2.0 wt% Pt and 1 wt% Ru, in a 1:1 atomic ratio.

XRD patterns in Figure 3.17 (middle 2 patterns) show that PtRu bimetallic catalyst is also very highly dispersed, there was minor difference between 1st and 2nd SEA cycles.

The reducibility of the catalysts was examined by H_2-TPR analysis. In Figure 3.18, the main reduction peak of the RuHCN precursor on alumina is seen to be about 530ºC,

while the PtHC precursor reduces as much lower temperature. Ru reduction in the PtRu sample is shifted down to 400ºC, which can be attributed to hydrogen spillover from closely interacting Pt sites.

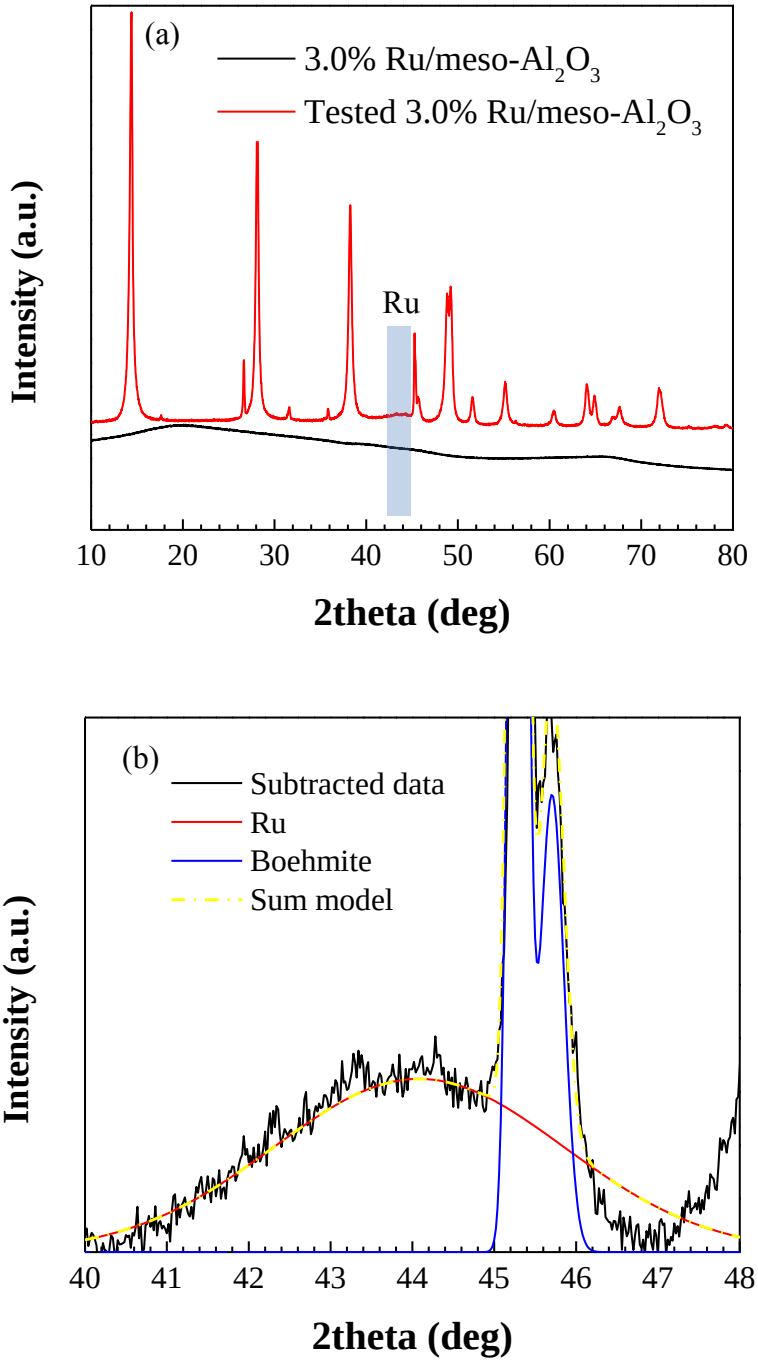

Figure 3.15.a) XRD pattern of fresh and tested (300ºC) 3.0%Ru/ meso-Al_2O_3 and b) Ru deconvolution from boehmite in tested 3.0%Ru/ meso-Al_2O_3.

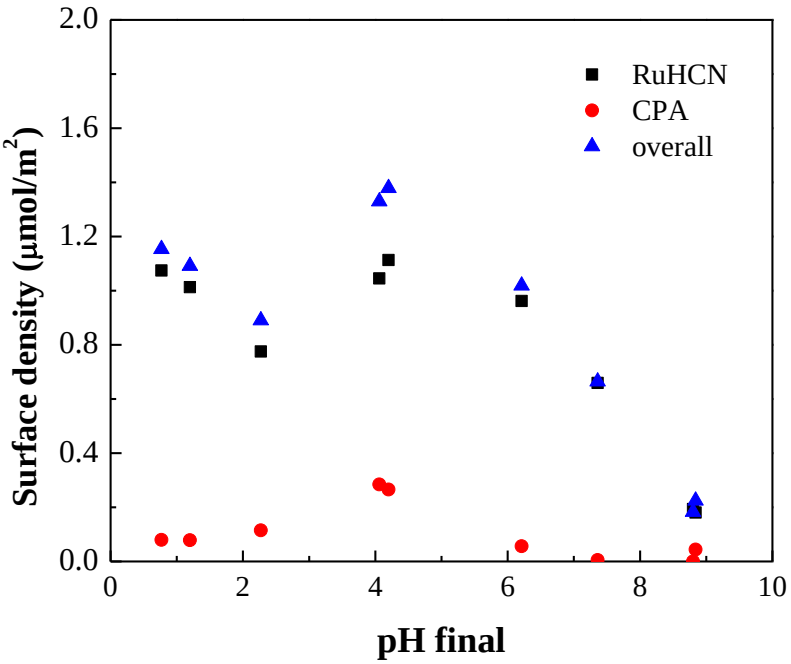

Figure 3.16. Bimetallic uptake of RuHCN and PHC on meso-Al_2O_3.

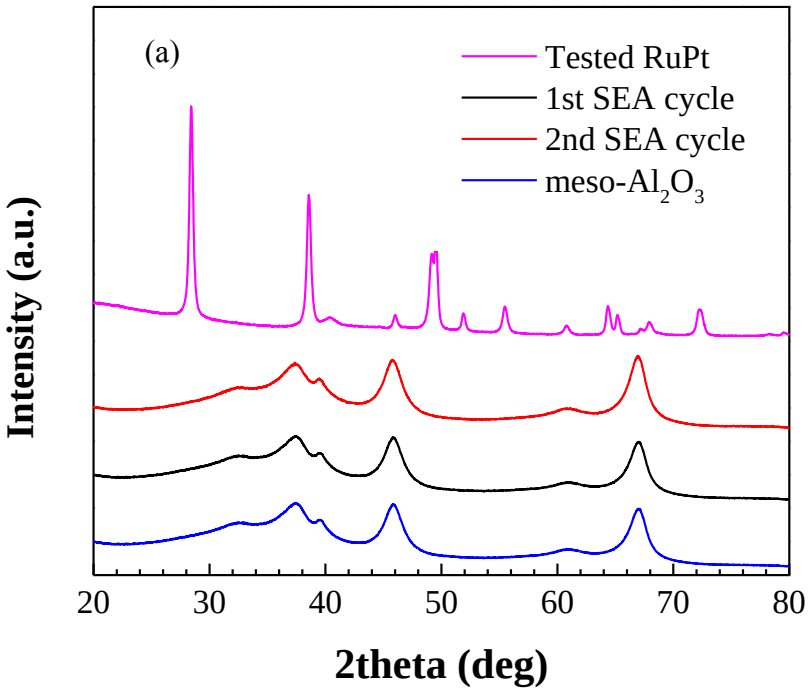

Figure 3.17.a) XRD patterns of fresh and spent bimetallic 1%Ru2%Pt/ meso-Al_2O_3.

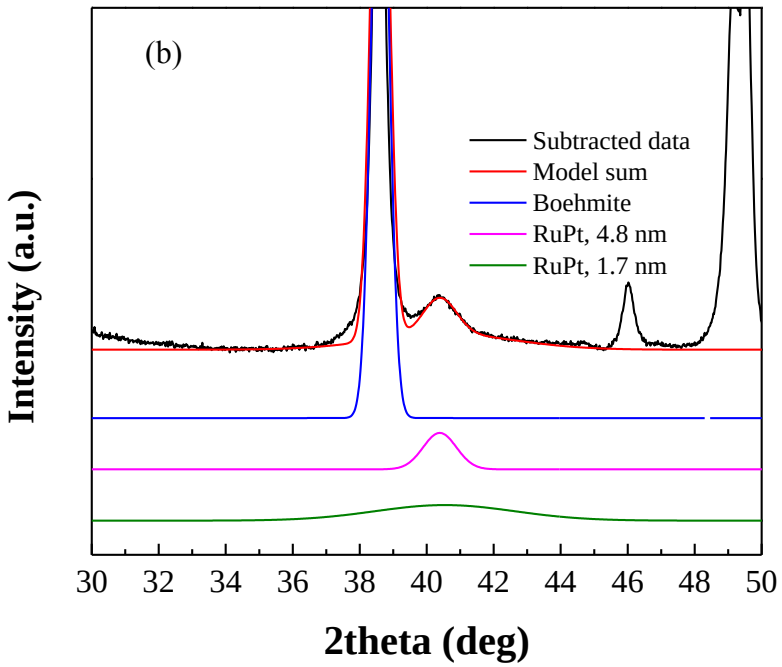

Figure 3.17.b) peak deconvolution of spent bimetallic 1%Ru2%Pt/ meso-Al_2O_3.

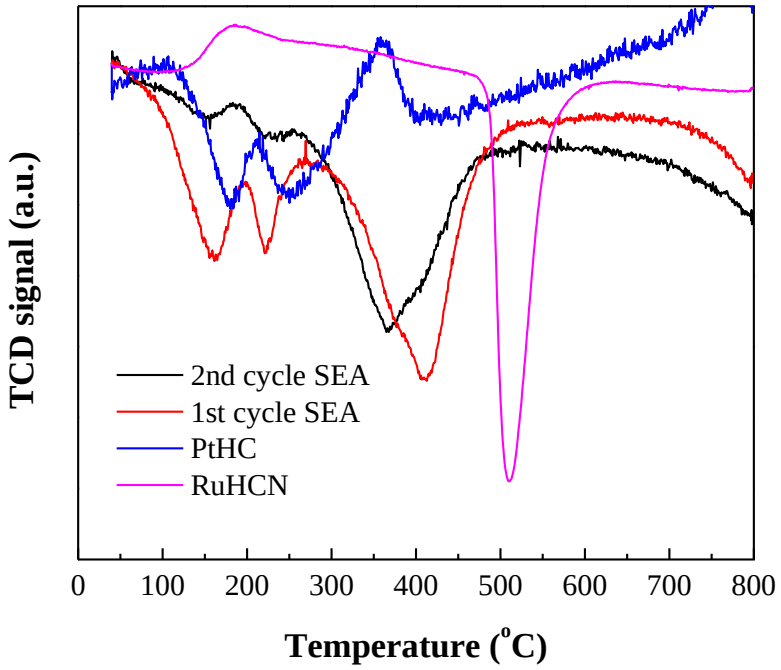

Figure 3.18. TPR profiles of monometallic Ru, Pt and bimetallic RuPt catalysts.

The alloying of metals in 1.0%Ru-2.0%Pt/meso-Al_2O_3 was further characterized by STEM (Figure 3.19). In the sample of fresh PtRu bimetallic catalyst (Fig. 3.19 a and b), the majority of nanoparticles are less than 2 nm, while small numbers of larger aggregates were as big as 4.3 nm. Those were identified as Pt-rich as shown in the representative elemental maps (Fig 3.19a, blue square). The volume-averaged STEM size (1.9 nm) is in reasonable agreement with the XRD result in Fig 3.17 (middle 2 patterns), which showed no metal peaks. The absence of PtRu peaks from XRD pattern can be attributed to the high portion of very small nanoparticles in Figure 3.19. The minor difference among Dv, Ds and Dn further implies a tight particle size distribution and confirms the small percentage of large aggregates in the sample (Figure 3.19c). When taking a close look at STEM images of the smaller (<2 nm) bimetallic nanoparticles, speckling was observed consistent with heavier and therefore brighter Pt atoms (red circles in Figure 3.19b) intermixed with Ru atoms. Close contact between Pt and Ru is also consistent with the TPR results in Figure 3.18 showing enhanced reducibility of the alloyed sample. Numerous ultra-small clusters are also evidenced in the images and the X-ray maps (to the figure of Figure 3.19a). The X-ray maps reveal that the larger particles are mostly Pt, with Ru being distributed more evenly over the support, but seemingly in relatively close contact with Pt.

STEM images and maps of used catalyst are shown in Figure 3.20 and are consistent with XRD patterns: noble metal particles slightly sintered after 2 hours reaction aging at 300^{o}C. In the spent PtRu catalyst, an average size of 2.2 nm is obtained for a representative sample. More significant overlap between Ru and Pt is seen in the spent

catalyst's elemental maps in Figure 3.20a. The small clusters of atoms have disappeared from the spent samples.

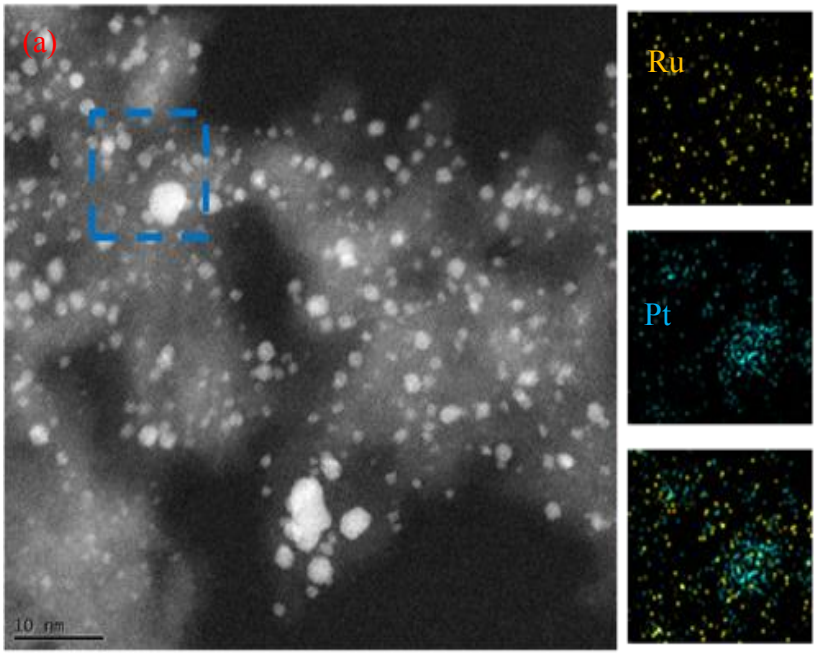

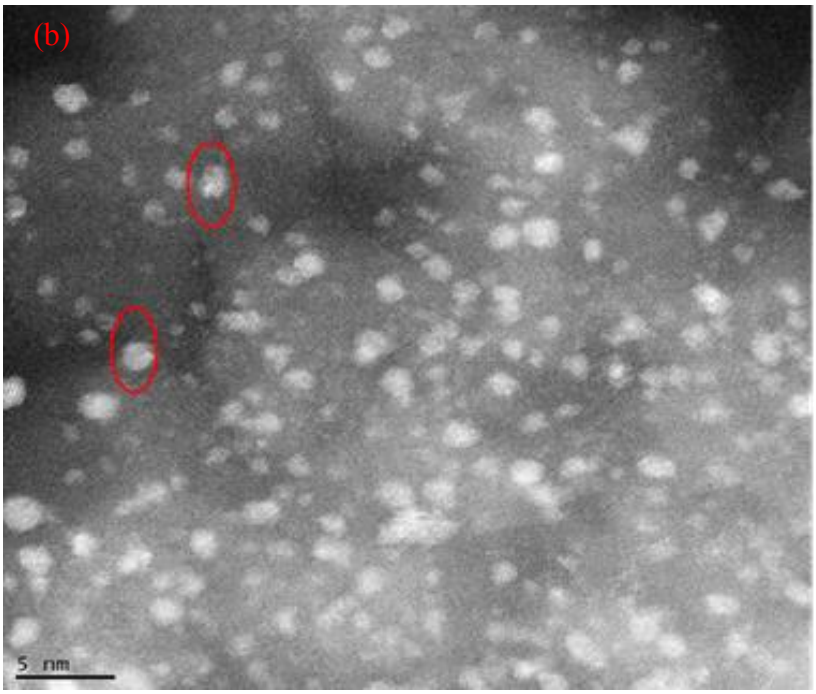

Figure 3.19. STEM of Pt/Ru on meso alumina catalysts, (a) and EDXS elemental maps (blue=Pt, yellow=Ru) and (b) STEM images of fresh PtRu bimetallic nanoparticles.

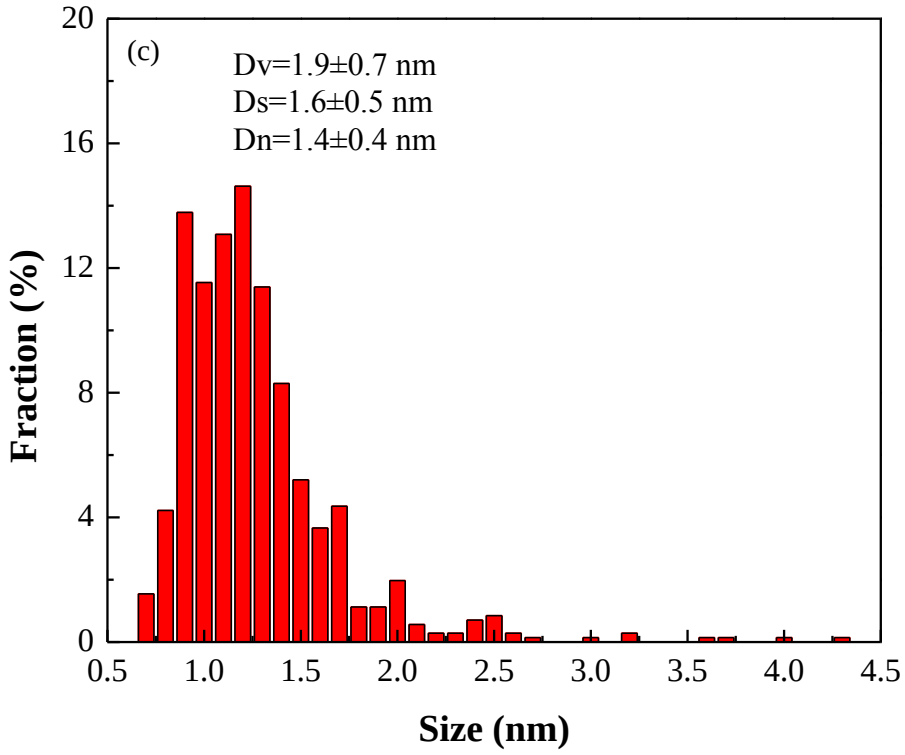

Figure 3.19.c) Fresh particle size distribution in.STEM images of fresh PtRu bimetallic nanoparticles.

b) Cu and Ni Single and Bimetallic Catalysts on meso-Alumina

An effective shortcut version of SEA termed "Charge Enhanced Dry Impregnation" was used for the simultaneous deposition of Cu and Ni onto mesoporous alumina. In this preparation, the Cu and Ni-containing precursor solution pH was acidified with citric acid; the citrate complexes with the metals to form anionic complexes and these electrostatically adsorb over a protonated and positively charged alumina surface. Cu and Ni concentrations of 185 ppm and 201 ppm were used in 0.85 ml of solution along with 0.0634 g citric acid for 1.00 g of support, giving resulting weight loadings of 1.0 and 1.0% Cu and Ni. The wet paste was dried in muffle furnace at 100^{o}C overnight and reduced in 20% H_2/He at 400^{o}C for 1 hour.

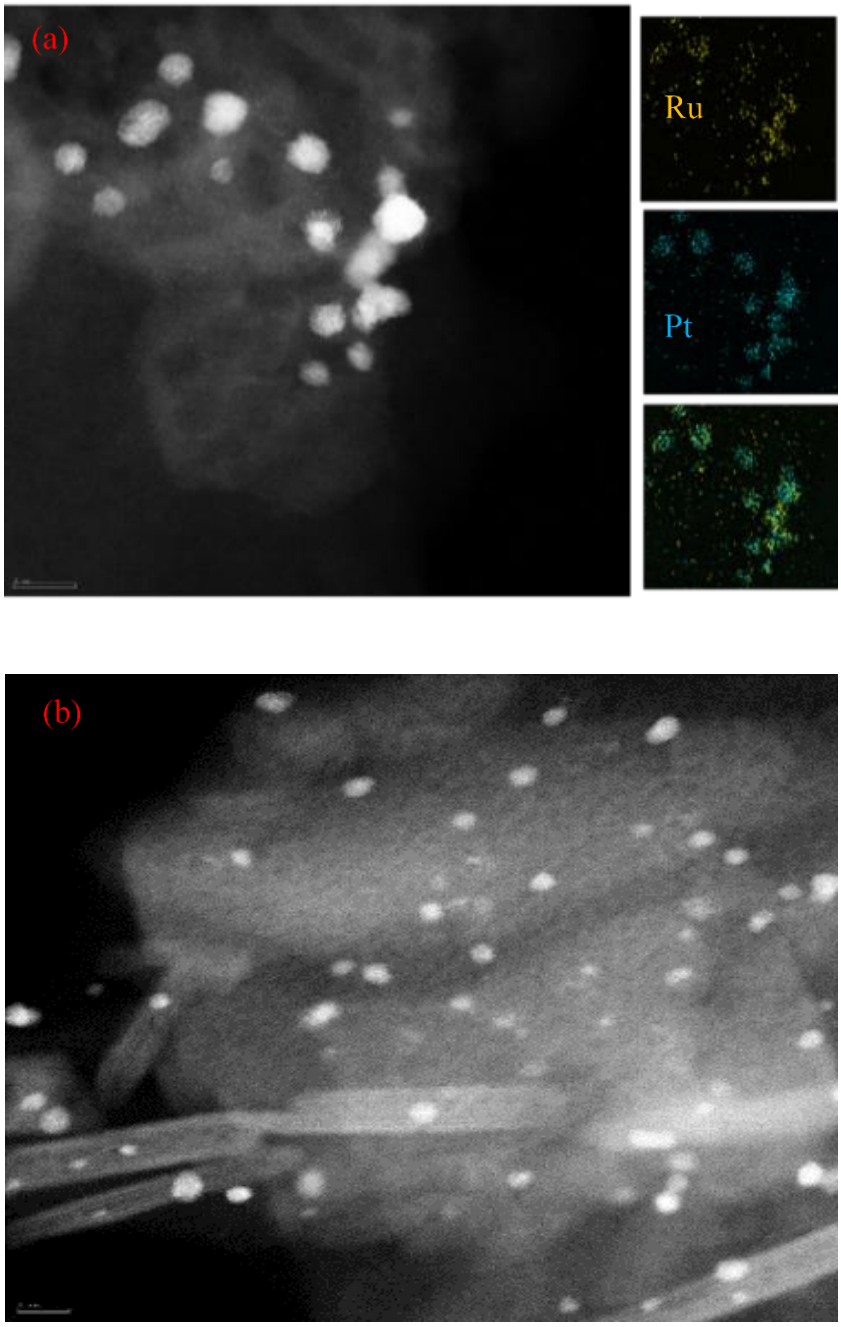

Figure 3.20.a) EDXS elemental maps (blue=Pt, yellow=Ru) and b) STEM images of spent PtRu bimetallic particles.

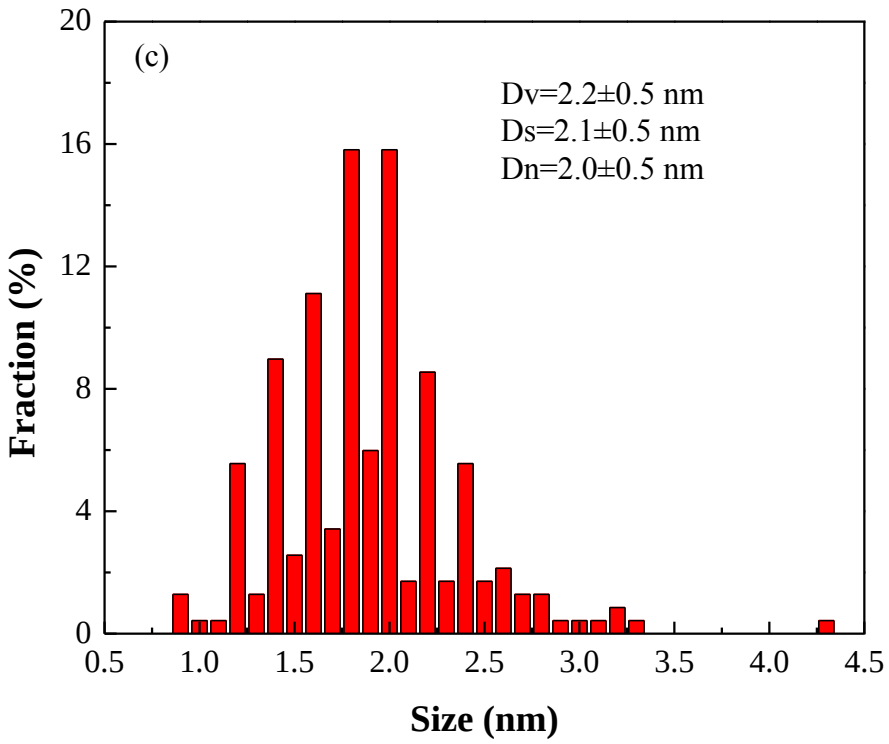

Figure 3.20.c) Spent particle size distribution in spent PtRu bimetallic catalyst.

The XRD analysis of fresh and spent 1.0% Ni-1%Cu/meso-Al_2O_3 catalysts is shown in Figure 3.21a. The peak around 43.6 $^o2\theta$ is between that of Cu and Ni metals and implied NiCu alloy formation during synthesis. The estimated size corresponding to these alloyed particles was 4.4 nm. In the spent NiCu/meso-Al_2O_3 catalyst, alumina hydration to boehmite occurs as before. In addition, separate, sharper reflections centered at 43.6 $^o2\theta$ (same species as in fresh catalyst), 44.1 $^o2\theta$ (Ni-rich alloy) and 44.5 $^o2\theta$ (separate Ni) appeared which implies NiCu sintered and dealloyed during the high temperature test. The same CuNi alloy species as in fresh catalyst sintered to 14.1 nm after use; a large portion of Ni dealloyed from CuNi alloy and a small portion Ni-rich alloy appeared as a result. The dealloyed particle size was determined as 24.6 nm Ni-rich alloy and 16.3 nm Ni

particles. The detailed deconvolution of fresh and tested catalysts was shown in Figure 3.21b and c respectively. Compared with noble metal catalysts in Figure 3.19, base metal catalysts are less resistant to sintering and dealloying under the same conditions.

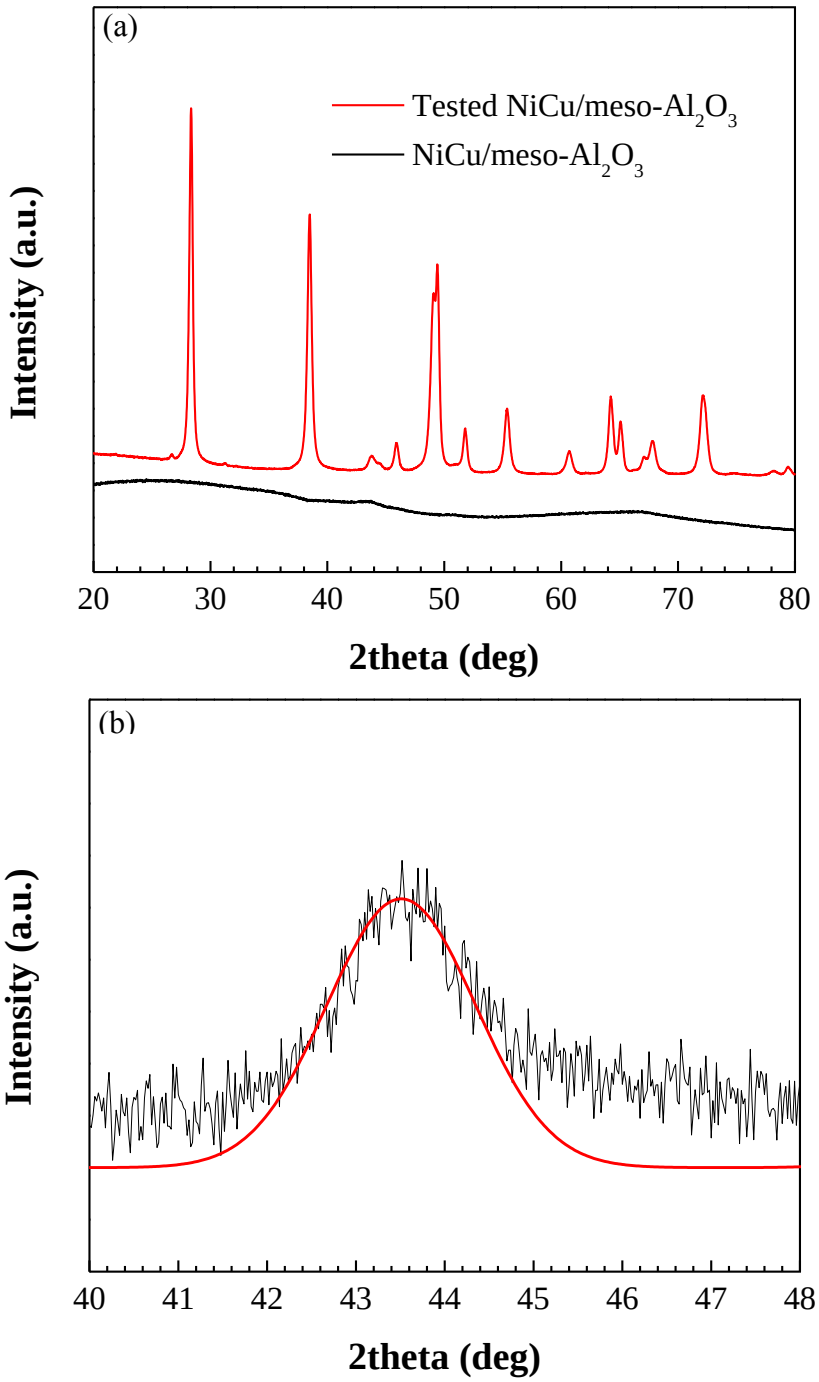

Figure 3.21.a) XRD profiles of bimetallic 1Ni1Cu/mA catalysts before and after reaction; b) deconvolution of fresh bimetallic 1Ni1Cu/mA catalyst.

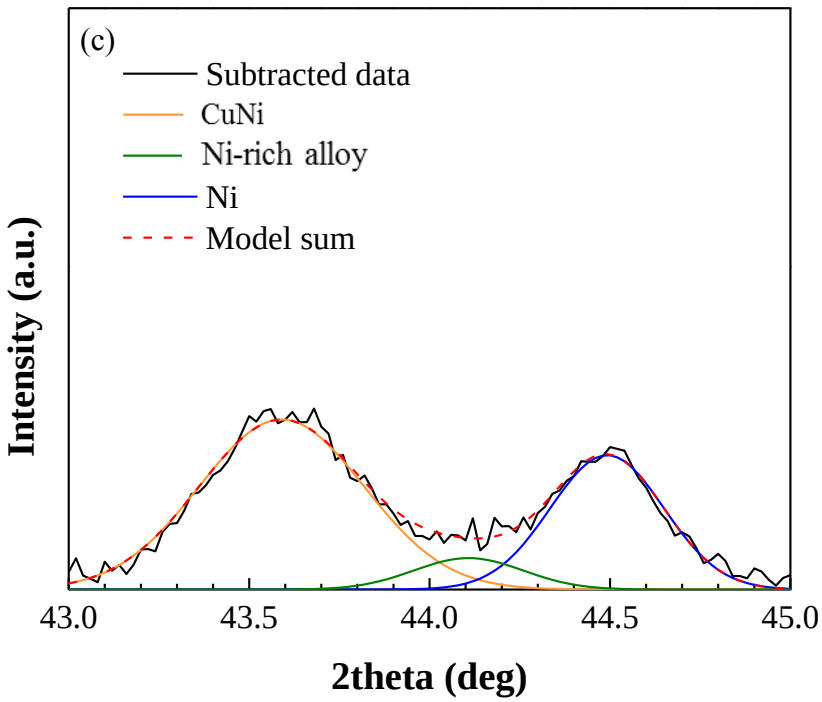

Figure 3.21.c) Deconvolution of spent bimetallic 1Ni1Cu/mA catalysts.

c) Cu and Ni Single and Bimetallic Catalysts on Carbon

Carbon supported base metal catalysts were also compared considering its strong hydrophobicity. 1.0%Ni-1.0%Cu/carbon TRX was synthesized by the same method as 1.0%Ni-1.0%Cu/meso-Al_2O_3.

STEM images of Cu/Ni/carbon catalysts are shown in Figure 3.22. A core-shell structure becomes discernable in the STEM images and EDXS elemental maps of the larger particles, as outer shell structures appear in the images and the Ni maps are broader than the Cu maps in Figure 3.22a. Meanwhile Cu particles, of size less than 1 nm (yellow in elemental maps) are highly disperse on the support. Ni is not directly associated with these smallest particles but cannot be precluded, given their small size and the small Ni signal which would arise from them. The average size (4.4 nm) is larger (Figure 3.22b) than the

noble bimetallic catalyst which can be attributed to the modified CEDI preparation method, which is not as effective as SEA as producing ultra-small nanoparticles [75, 80]. The volume average size is larger than the one estimated from XRD (3.3 nm) in Figure 3.23a and b, this can be explained in STEM and elemental maps: ultra-small Cu particles (yellow in elemental maps) spread homogeneously on the support, which were not counted when sizing the sample images, whereas these contributed to a smaller size estimation in bulk technique.

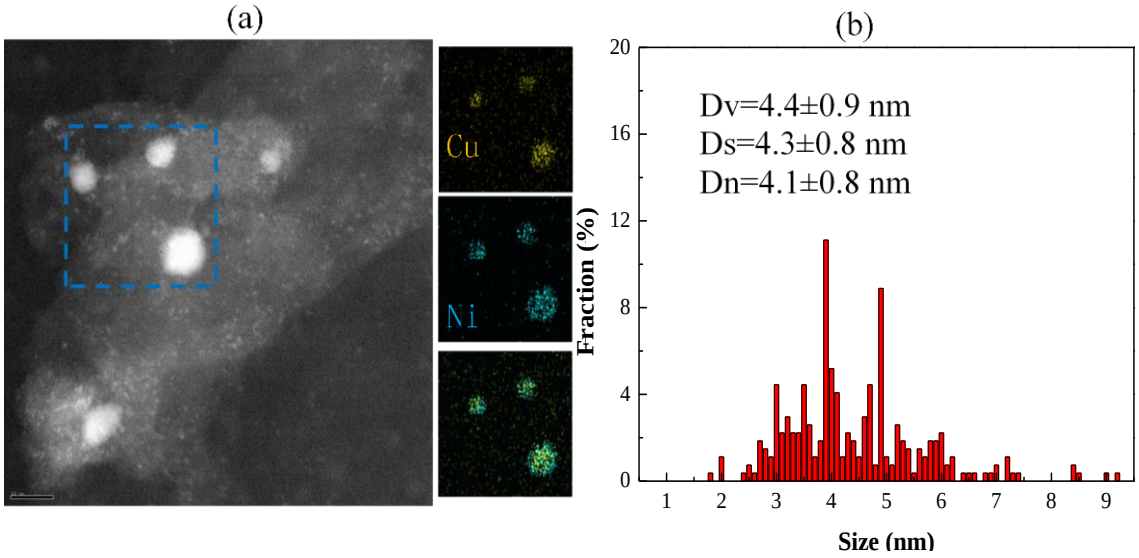

Figure 3.22.a) STEM images and EDXS elemental maps of fresh NiCu bimetallics, blue=Ni, yellow=Cu, (b) fresh particle size distribution.

The XRD analysis of fresh and tested Ni/Cu/C catalysts is shown in Figure 3.23. The peak around 43.8 $^{o}2\theta$ is between that of Cu and Ni metals and implies NiCu alloy formation during synthesis. The estimated size corresponding to these alloyed particles is 3.3 nm (Figure 3.23b). A very similar situation to spent NiCu/meso-Al_2O_3 was noticed in the spent NiCu/C catalyst; the majority of the NiCu formation in fresh catalysts dealloyed and sintered, seen as separate sharper reflections at 43.4 $^{o}2\theta$ and 44.4 $^{o}2\theta$. The particle size

is determined as 16.2 nm for the Cu-rich alloy, 22.1nm for the original CuNi alloy (same species as in fresh one) and 17.4 nm for the Ni-rich alloy particles (Figure 3.23c). STEM images further confirmed that large particles formed and that the majority of NiCu core-shell structure dealloyed with use (Figure 3.24). Additionally, XRD revealed Ni oxide and Cu oxide in the spent catalysts, indicated by the shaded 2 range of Figure 3.23a.

Figure 3.25 summarizes characterization the three sets of fresh and spent HDO catalysts. In fresh catalyst, NiCu particles were ~ 3 times larger than RuPt particles in size. Noble metal catalysts showed better resistance to sintering and dealloying than base metals; and base metals sintered to the similar level on both supports.

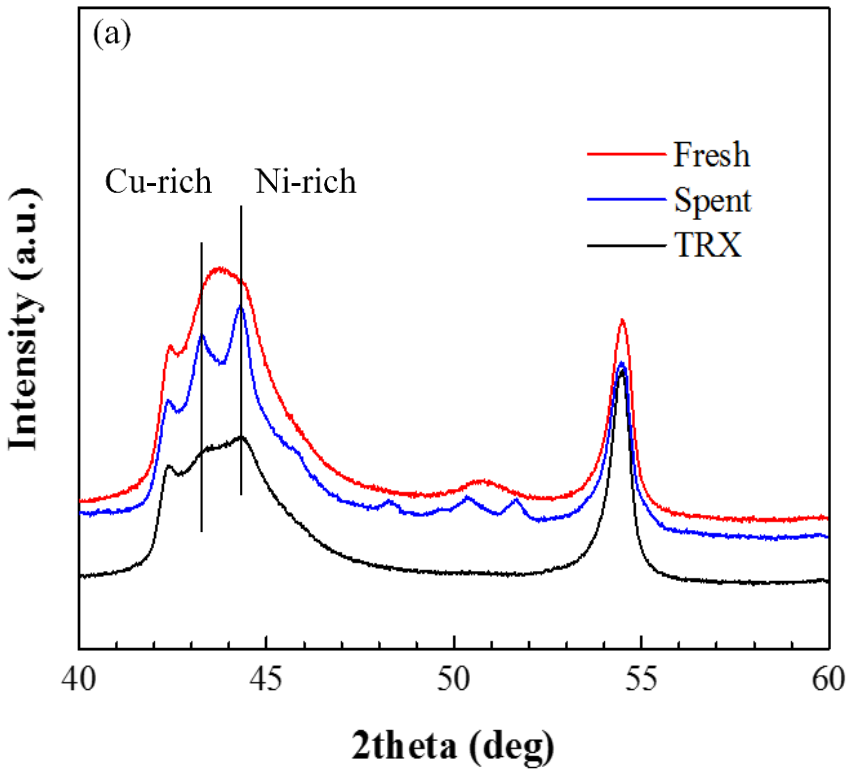

Figure 3.23.a) XRD profiles of bimetallic 1Ni1Cu/C catalysts before and after reaction.

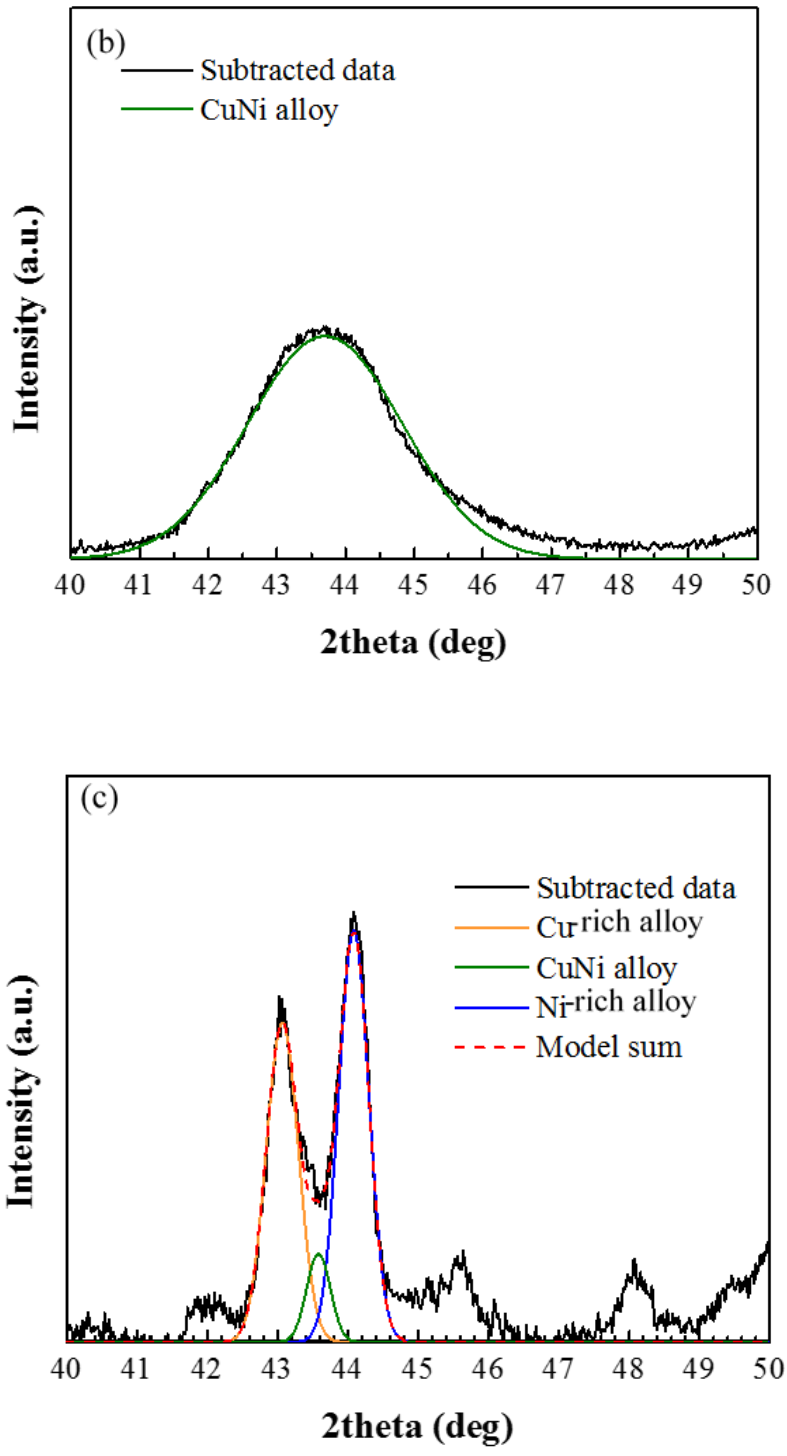

Figure 3.23.b) Deconvolution of fresh bimetallic 1Ni1Cu/c catalyst; and c) deconvolution of spent bimetallic 1Ni1Cu/C catalysts.

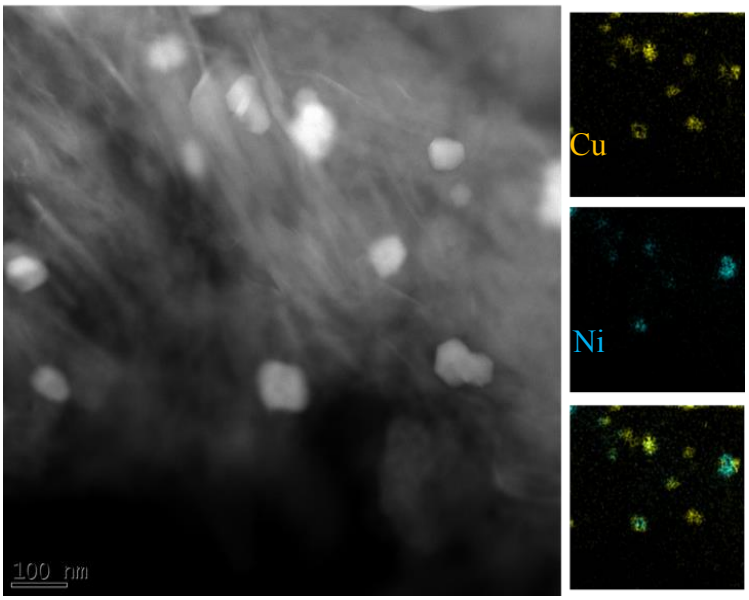

Figure 3.24. STEM images and EDXS elemental maps of spent NiCu/C.

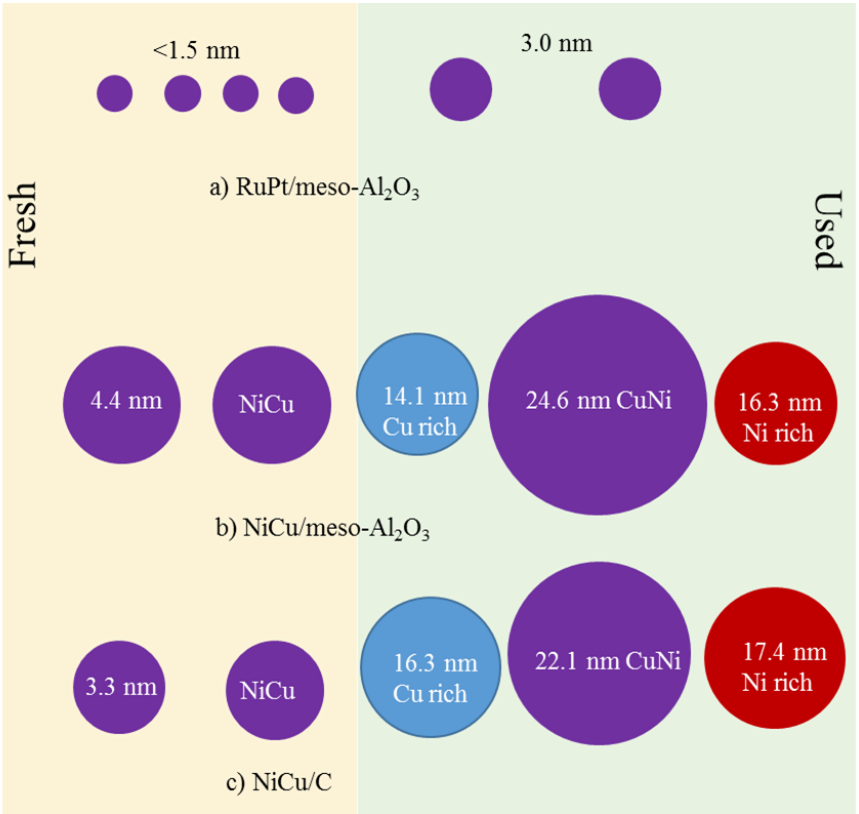

Figure 3.25. Particle size sintering of three bimetallic catalysts during HDO reactions.

d) HDO Evaluation

The three series of catalysts, Pt/Ru/meso-alumina, Cu/Ni/meso-alumina, and Cu/Ni/carbon were evaluated in USDA-ARS for hardwood-derived bio-oil HDO according to the detailed procedures provided in Chapter 2. For data comparison, the catalyst: bio-oil loading is defined as:

$$CL_i = \left(\frac{x_{cat} w_{cat}}{w_{oil}}\right) \times 100$$

The cat:oil of base metal catalysts were 3 times of that of noble metal catalysts due to the particle sizes in fresh catalysts as demonstrated in Figure 3.25 to keep the total metal surface constant. The full comparison of single to bimetallic noble and base metal catalysts, prepared by CEDI as well as dry impregnation, is to be found in a collaborative publication with the team of Dr. Yaseen Elkasabi at USDA-ARS [96]. In this thesis, reactivity data is reported only for the CEDI-prepared bimetallic catalysts which in all cases performed better than the single metal and DI-prepared catalysts in terms of lowering oxygen content and increasing aromatic product yield.

GC-MS and NMR were utilized to analyze the whole sample (gas phase and liquid phase) directly from the reactor, which allows for separation of the catalyst by dissolution into the deuterated solvent, without loss of lighter compounds. Concentrations of specific compounds that are more abundant in pyrolysis oil and HDO products were measured on GC-MS. A preliminary comparison can then be made with regards to catalyst selectivity. Tables 3.2 displays the GC-MS concentrations of specific compounds for which calibrations were carried out. Due to the complexity of composition in bio-oil and its HDO, concentrations of the most abundant compounds provide an accurate projection on the overall chemical nature and reactivity.

Highly reactive compounds like acetic acid, furfural, and acetol significantly reduced compared with bio-oil, with the latter two almost reducing down to zero. Cyclopentanone and its methyl derivatives were observed in product analysis which might be from the hydrogenation of species in starting bio-oil or subsequent intermediate species.

Table 3.2. GC-MS concentrations of some dominant compounds detected in bio-oil HDO reactions with base metal catalysts.

	bio-oil	2%Pt1%Ru/mA	1%Ni1%Cu/mA	1%Ni1%Cu/C
Cat:oil	---	0.267	0.768	0.777
Acetic acid	5.54	1.92	1.92	0.64
Acetol	2.06	0.02	-	0.03
Furfural	0.7	0.17	-	0.02
Levoglucosan	2.66	0.04	-	0.03
Cyclopentanone	0.03	0.25	0.27	0.19
2-methyl-2-cyclopenten-1-one	0	0.58	0.71	0.07
2-methyl-cyclopentenone	0.02	0.50	0.36	0.47
Phenols/cresols	1.5	6.79	3.45	5.82
Methoxyphenols	0.12	0.81	2.07	0.58
Aromatic hydrocarbons	0.05	0.21	1.63	0.42
BTEX	0.05	0.09	0.76	0.26

When comparing concentrations of phenols (which is one of the most abundant chemicals in bio-oil, including phenol, cresols, and 4-methylphenol) with the elemental analyses, the oxygen contents directly correlate with proportionally varying concentrations of phenols and methoxylated phenols. When a mass balance is calculated, the total weight of phenols post-reaction outweighs the total phenols concentration in the original bio-oil which likely stems from the catalytic breakdown of higher molecular weight compounds. precious metal RuPt bimetallic catalysts gave significant increases in phenols

concentrations (6.79% v.s.1.5% in bio-oil); for NiCu bimetallic catalysts, 5.82% of phenols were yielded on 1%Ni1%Cu/C and that on 1%Ni1%Cu/meso-Al_2O_3. This suggests that, for alkyl phenol production, bimetallic base metals improve the yield for carbon supports, while the effect of mesoporous alumina support dominates the effect of metal type.

The GC-MS measurements of aromatic hydrocarbons have the greatest significance in catalytic performance. The production of hydrocarbons was observed on all three bimetallic catalysts and half of which categorized into BTEX. The concentration of aromatic hydrocarbons increased 4 times on 2%Pt1%Ru/meso-Al_2O_3, and NiCu/C yielded 7 times higher than the starting bio-oil; in particular, NiCu/meso-Al_2O_3 catalyst produced the highest amounts (1.63% v.s. 0.05% in starting bio-oil). As is in the case with phenols, the effect of support dominates the effect of metal type. The effect of meso-Al_2O_3 on NiCu is additive, producing the highest level of aromatic hydrocarbons.

Table 3.3. Percentages of hydrogen belonging to functional groups, based on 1HNMR spectra integration.

Chemical group(s)	(hetero-) aromatics	Alcohols, methoxy	-aliphatics	Alkanes
	8.0 - 6.0 ppm	4.8 - 3.4 ppm	3.0 - 1.5 ppm	1.5 - 0.5 ppm
bio-oil	8.7	34.8	44.3	12.2
2%Pt1%Ru/mA	15.3	3.1	51.1	30.6
1%Ni1%Cu/mA	25.2	4.2	48.9	21.7
1%Ni1%Cu/C	19.8	3.6	51.6	25.0

While the GC-MS results provide a window into the selectivity of compound formation, the compounds measured are only finite in number and of low absolute concentration. For a more comprehensive observation on aromaticity and deoxygenation, we employed NMR spectroscopy. Using previously established criteria for bio-oil

analysis[97], all spectra demonstrate varying changes in the amounts of aromatics (8.0 – 6.0 ppm), alcohols/methoxy groups (4.8 – 3.4 ppm), -aliphatics (3.0 – 1.6 ppm), and alkanes (1.6 – 0.5 ppm). Generally, all samples increased in aromatics and aliphatics/alkanes and decreased in oxygenated hydrogens after 3 hours HDO reactions. Specifically, Table 3.3 displays the peak integration percentage values for the aforementioned regions. All catalysts produced significant amounts of alkane hydrogens compared to starting oil (2-3 fold increases), and the amount of -aliphatics showed minor variations from bio-oil. All catalysts had comparable performance in significantly lower alcohols and methoxy hydrogens. As for the production of aromatics, consistent with GC-MS results, meso-Al_2O_3 supported NiCu presented the highest aromatic hydrogen amount, showing 25.2% of hydrogen in aromatic rings. Those for NiCu/C and PtRu/meso-Al_2O_3 were 19.8% and 15.3% respectively, 2-3 fold greater than bio-oil.

Based on the characterization in the previous section, NiCu/C and NiCu/ meso-Al_2O_3 sintered and dealloyed to a similar extent (16.2 nm Cu, 22.1 nm NiCu and 17.4 nm Ni on C, 14.1 nm Cu, 24.6 nm NiCu and 16.3 nm Cu on meso-Al_2O_3). Given the similar metal nanoparticle compositions, it is seen that the alumina support is superior to the carbon support for enhanced yields of aromatic products. And on the same alumina support, it is the base metal catalyst and not the noble metal catalyst that has the better performance even though the noble metal nanoparticles remained relatively well dispersed and well alloyed.

3.3 Conclusion

Highly dispersed Ru and Pt monometallic catalysts were synthesized on SBA-15, Zr-SiO_2, Al-SBA-15 and mesoporous Al_2O_3 by SEA, as seen in XRD and STEM. The hydrothermal stability of SiO_2 was improved by Zr and Al incorporation and carbon

coating; and such decoration had no effect on metal uptake and metal particle size. However, the modified SiO_2 became unstable in high temperature tests (300 ^oC): Ru particles sintered to 4.2 nm on 4.8%Zr-SiO_2; Ru and Zr leached out with carbon coating in 10%C-4.8%Zr-SiO_2; Al-SBA-15 dissolved during the test. The self-synthesized meso-Al_2O_3 was proved to be most promising support under high temperature hydrothermal conditions: 24% loss in surface area at 220 ^oC after 24 hours in water, and the BET surface area slightly increased from 245 m^2/g to 306 m^2/g after tested at 300 ^oC for 2 hours. In the high temperature, tested Ru catalyst, the amorphous Al_2O_3 transformed into boehmite, meanwhile, Ru particle size increased from 1.2 nm to 2.5 nm. 1%Ru-2%Pt/meso- Al_2O_3 was prepared by co-SEA, showing highly dispersed and well alloyed formation by XRD, STEM and elemental mapping. Particle sizes for precious metals exhibited minimal sintering under hydrothermal condition: showing an average size of 3.0 nm. 1.0%Cu-1.0%Ni/meso-Al_2O_3, 1.0%Cu-1.0%Ni/C were prepared by citric acid dry impregnation, with 4.4 nm and 3.3 nm CuNi alloy particles respectively. Base metals sintered up to 25 nm, and only a minor fraction of bimetallic nanoparticles remained after reaction. Despite this, NiCu bimetallic catalysts yielded higher production of aromatic hydrocarbons than the noble metal catalyst. Alumina was a much better support than carbon for the base metal catalyst. Utilization of bimetallic base metal SEA catalysts on the stable mesoporous alumina support for HDO is a promising, inexpensive alternative but will require further stabilization.

Chapter 4

Metal particle size control by 'hard' and 'soft' chemistry and size determination by powder XRD [1,2]

4.1 Introduction

Supported noble metal catalysts have been widely used in chemical and energy production as well as environmental protection [22]. The number of active metal sites in catalyst is often described in terms of dispersion, or the ratio of metal sites existing at nanoparticle surfaces, divided by the total number of metal atoms. Metal nanoparticles with 1 nm are considered to have 100% dispersion. This is desirable in many cases; however, many reactions exist for which larger particle sizes give higher overall activity by virtue of greater numbers of certain sites such as terrace sites present only on larger particles. The size dependence of many chemical reactions has not been studied in a systematic way (for example, there have been no reports on the systematic control of metal particle size); thus, it is important to have a method to produce a smoothly varying set of particle sizes which can be synthesized over the same support. Two methods to tune metal

[1] Subsection 4.2.1: reproduced from Ref. 70 (Q. Liu, U. A. Joshi, K. Über and J. R. Regalbuto, Phys. Chem. Chem. Phys., 2014, 16, 26431, DOI: 10.1039/C4CP02714K) with permission from the PCCP Owner Societies.

[2] Subsection 4.2.2: reprinted from Catalysis Today, Volume 280, Part 2, Qiuli Liu, Jadid Samad, John E. Copple, Somayeh Eskandari, Christine Satterwhite, John R. Regalbuto, A pinch of salt to control supported Pt nanoparticle size', 1 February 2017, Pages 246–252. Copyright (2017)

particle sizes will be introduced in this session. The first method is called as 'hard chemistry' where SEA prepared metal catalysts are treated at elevated temperature in humid reducing flow for extended time to sintered the particles to larger and larger sizes. In this way, series of catalysts with well-controlled ranges of particle sizes can be prepared over commercially viable, high surface area mesoporous SiO_2 using common metal precursors.

The other method was involving salt impregnation, named as 'soft chemistry'. In the course of the latter study we noticed a profound effect of the residual balancing ions from the precursor [75]. When cationic Pt tetraammine hydroxide, $(NH_3)_4Pt(OH)_2$, was used as precursor with CEDI over silica, particles <1.5 nm could easily be synthesized over silica by drying the contacted paste and reducing in flowing hydrogen. However, when Pt tetraammine chloride, $(NH_3)_4PtCl_2$, was employed at the same conditions and pretreated in the same manner, the particles averaged 8.2 nm in size. The size could be lowered back to <1.5 nm by eliminating the residual chloride by washing the $(NH_3)_4PtCl_2$-based sample after impregnation [75 in Supplementary Information]. Chloride is often used to redisperse sintered Pt nanoparticles through an oxychloride intermediate [98-100]. In the current study, however, we demonstrate that it as well as nitrate can be used to influence nanoparticle formation from the adsorbed ammine precursors and so sinter the evolved nanoparticles to a controllable extent. This provides a simple way to synthesize a variety of particle sizes at constant metal loading. In this way series of catalysts can be easily prepared to allow the study particle size on reactivity, which is a critical aspect of catalyst design for many reactions [71, 101-103]. We examine the effect of chloride and nitrate ions on Pt particles generated from tetraammine precursors over alumina, silica, silica-alumina, titania, and

carbon supports. Pt particle size was determined by XRD, STEM and H_2-chemisorption, which gave consistent results, and is correlated with Cl^-/Pt and NO_3^-/Pt atomic ratios; the residual ions have the greatest effect over carbon, and least effect over alumina and titania. X-ray powder diffraction is widely utilized in the field of catalysis. To obtain precise XRD data analysis, it is a requirement to separate background and noise from sample signal. Even though a better signal/noise ratio can be achieved by increasing the measuring counts, due to the limitation of standard scintillation counter detector, nanoparticles below 2 nm are barely visible in XRD patterns, especially when the metal loading is low. The detection limit of conventional X-ray powder diffraction for nanoparticles in heterogeneous catalysts is 2-2.5 nm. The application of silicon strip detector improves signal to noise ratio and ultra-small metal particles (down to 1 nm) can be detected thus. The comparison between scintillation detector a) and latest D/tex Ultra b) are presented in Figure 4.1: Pt size is estimated as 8 nm with silicon strip detector, while the same sample shows worse-shaped diffraction buried by noise under the conventional detector, leading to complexities in size estimation.

Characterization by conventional XRD barely provides no information on Pt particle size determination, especially for low Pt loading due to the poor detection sensitivity and large noise to signal ratio. In the case of Pt/Al_2O_3 and Pt/Mo_2C, utilization of XRD is further confined by the fact that γ-Al_2O_3 and Mo_2C diffraction peaks overlap with Pt ones (Table 4.1). Accurate metal particle size in Pt/Al_2O_3 often relies on chemisorption [104-107] and TEM [104-105, 108-110], those techniques either requires energy input or time and money consuming. On the other hand, the utilization of latest generation Si strip detector improves the sensitivity of XRD by a better signal to noise ratio, and small

particles (< 2 nm) can be detected. Assisted by deconvolution software, we can separate support background from sample pattern regardless of the superposition of Pt and Al_2O_3, a much accurate HWHM value are achieved this way leading to a more accurate Pt particle size determination.

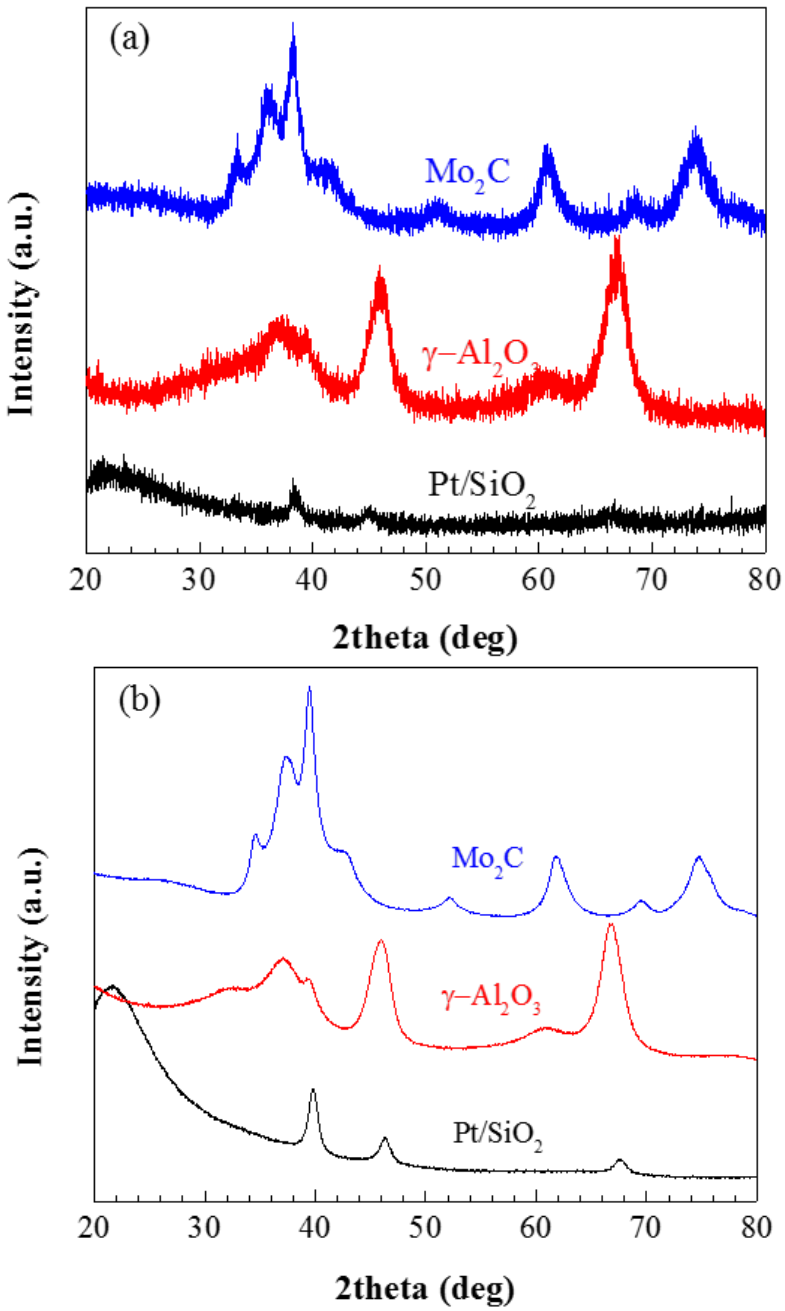

Figure 4.1. XRD patterns of Pt/SiO_2, γ-Al_2O_3 and Mo_2C under scintillation detector a) and silicon strip detector b).

Table 4.1. Summary of diffractions of Pt, γ-Al_2O_3 and Mo_2C.

2θ (°)	γ-Al_2O_3 hkl	2θ (°)	Pt hkl	2θ (°)	Mo_2C hkl
31.94	220	-	-	34.47	100
37.60	311	-	-	38.10	002
39.49	222	39.76	111	39.49	101
45.86	400	46.24	200	52.23	102
60.90	511	-	-	61.80	110
67.03	440	67.45	220	69.57	103

4.2 Results and discussion

4.2.1 Particle size controlled by 'hard chemistry'

7.6%Ru/SBA-15 and 5.4%Pt/SBA-15 were synthesized by SEA. Thermal treatment was first applied to these two catalysts. XRD analysis was performed with a high sensitivity Si slit detector (D/teX Ultra, Rigaku) allowing detection of particles as small as about 1 nm. The patterns for Ru/SBA-15 and Pt/SBA-15 are shown in Figures 4.2a and b respectively. The broad peak around 21 degrees 2θ is due to amorphous silica. The metal nanoparticles are below the detection limit of XRD, consistent with STEM results in Figure 3.3. No significant increase in particle size has been observed for the Ru/SBA-15 samples reduced at 500°C for 2h and 700°C for 2h. The Ru/SBA-15 samples reduced at 900 °C for 2h yields about 1.4 nm Ru particles. Similar thermal treatment carried out for Pt/SBA-15 is shown in Figure 4.2b: the average particle sizes do not change much up to reduction temperatures of 700°C. Sintering of Pt on SBA-15starts at 800°C, and at 900°C samples show mixed platinum-silicon phases ($Pt_{64}Si_{36}$ and Pt_2Si, top pattern in Fig 4.2b).

As there was no significant sintering of metallic Ru and Pt up to 700°C and 900°C, respectively, harsher conditions were required. A steaming-reduction process was employed using hydrogen saturated with water vapor for various times. Based on the

results of Figure 4.2, 900 and 800°C reduction temperatures were selected for Ru/SBA-15 and Pt/SBA-15 respectively. Figure 4.3 displays the XRD patterns for the two metals at various steaming reduction times. As the reduction time increases a gradual increase in particle size is observed. For Ru/SBA-15 (Figure 4.3a), steaming reduction at 900°C for 1 h gives particles of ca. 1.4 nm. At 12 hours, size is 2.8 nm, and at 2h, particles of 4.5 nm are obtained as shown in Table 4.2.

Table 4.2. Properties of Ru/SBA-15 and Pt/SBA-15 catalysts.

Ru/SBA-15			Pt/SBA-15		
Time (h)	Particle size (nm)	Surface Area (m^2/g)	Time (h)	Particle size (nm)	Surface Area (m^2/g)
0[d]	1.1	468	0[d]	1.3	340
1	1.4	155	2	2.0	NA
12	3.8	207	10	2.8	NA
24	4.5	201	16	3.3	292

A similar steaming-reduction process was performed at 800°C on Pt/SBA-15 with time varied from 2 to 16 h (Figure 4.3b). This yielded particle sizes ranging from 1 nm to 3.3 nm (Table 4.2). The broad peak observed at $2\theta = 38.72^o$ in pattern a of Figure 4.3b can be deconvoluted as Pt_3O_4 (211) (35.92^o) and Pt (111) (39.76^o) (Fig 4.3c). It appears that the smallest Pt particles (which are about 1.0 nm) can be substantially oxidized at room temperature. Small particles of Pt have been shown by past EXAFS analysis to oxidize at ambient conditions; the current study indicates that the phase is Pt_3O_4.

These results demonstrate that the size of noble metal particles supported on silica can be tailored with time and temperature of steam reduction. However, these harsh conditions affected the pore structure of the SBA-15 support as revealed by surface area measurements before and after the reduction treatment.

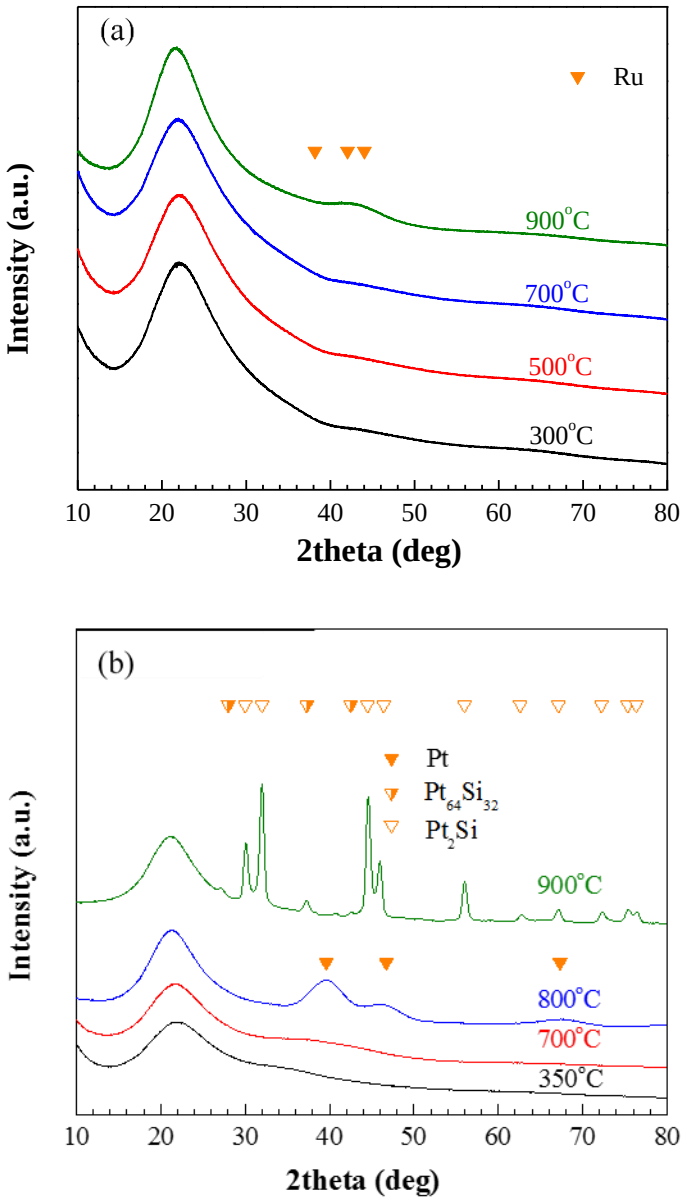

Figure 4.2. The XRD pattern showing the effect of heat treatment on the a) Ru/SBA-15, all reduction proceeded 2 hrs at 300 °C, 500°C, 700 °C and 900 °C; and b) Pt/SBA-15 catalysts, reduction proceeded 2 hrs at 350°C, 700°C, 800°C and 900°C (3 hrs). No significant increase observed up to 700°C in both cases.

Table 4.2 summarizes the BET analysis. The pure SBA-15 support used with Ru had a surface area of about 486 m2/g with uniform pore size around 5 nm. For Ru/SBA-15 catalysts, the 900°C steaming-reduction rapidly (one hour) diminished the surface area to

200 m^2/g or below and the pore structure was completely destroyed. The SBA-15 employed for Pt had an original surface area of 340 m^2/g and did not collapse so significantly (about 15%) at the 800°C steaming-reduction treatment for Pt.

Table 4.3. Support properties.

Support	PZC	BET surface area (m^2/g)	CEDI pore volume (mL/g)
γ-Al_2O_3	8.6	185	1.04
SiO_2	3.9	300	2.6
TiO_2 (calcined)	4.7	77	0.75
Carbon	4.2	185	0.85
Al-SBA-15	4.5	563	3.10

HAADF-STEM images of Ru particles following steam reduction treatment at 24h in Figure 4.4 clearly show Ru sintering. The particle size of 5.1 ± 0.6 nm was consistent with the XRD size estimate (4.5 nm) obtained from Fig 4.3a. In many areas Ru particles smaller than 1 nm were observed to coexist with much larger particles as shown in Fig 4.4b. This is consistent with the Ostwald ripening mechanism of sintering as found recently by the Datye group for Ni particle sintering in hydrogen and moisture [111-112]. In the present case, metal sintering is complicated by support sintering, even though the silica supports calcined at 900°C for 6h had an intact pore structure. STEM images of the 24 h steam-reduced samples (not shown) revealed no hexagonal pore structure. The moisture content was thus responsible for the instability of the silica phase at 900°C.

For catalytic applications, the collapse of pore structure is undesirable and so a method to sinter the well dispersed metal phase at lower temperature was devised, where only pinch salt was impregnated during catalysts synthesis by CEDI.

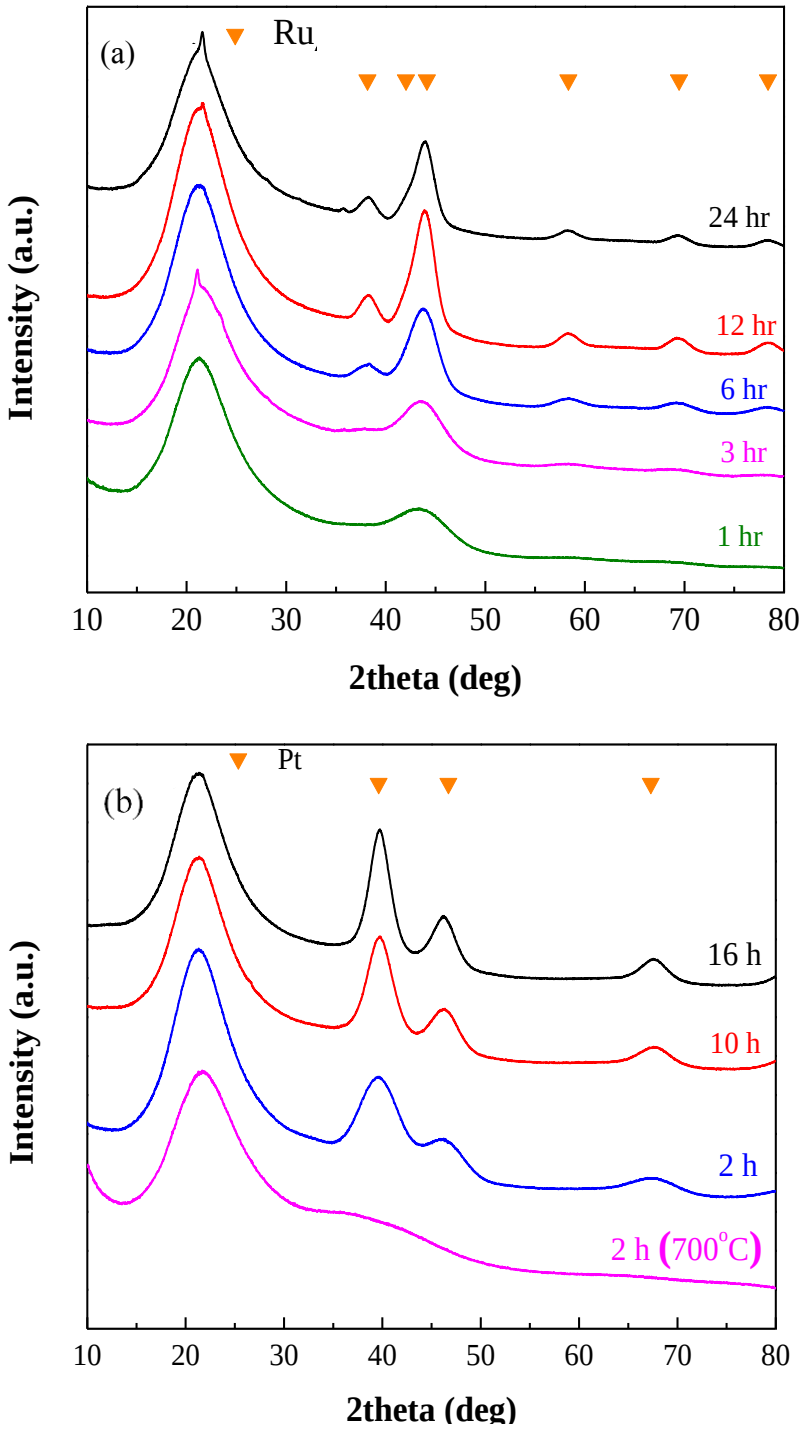

Figure 4.3. The effect of steaming-reduction time on particle size of a) Ru/SBA-15 at 900°C 1 hr, 3 hrs, 6 hrs and 12 hrs SR, b) of Pt/SBA-15 at 800°C, 2 hrs, 10 hrs and 16 hrs SR; orange triangle shows the position of Ru and Pt peaks respectively; particle size in Table 4.2.

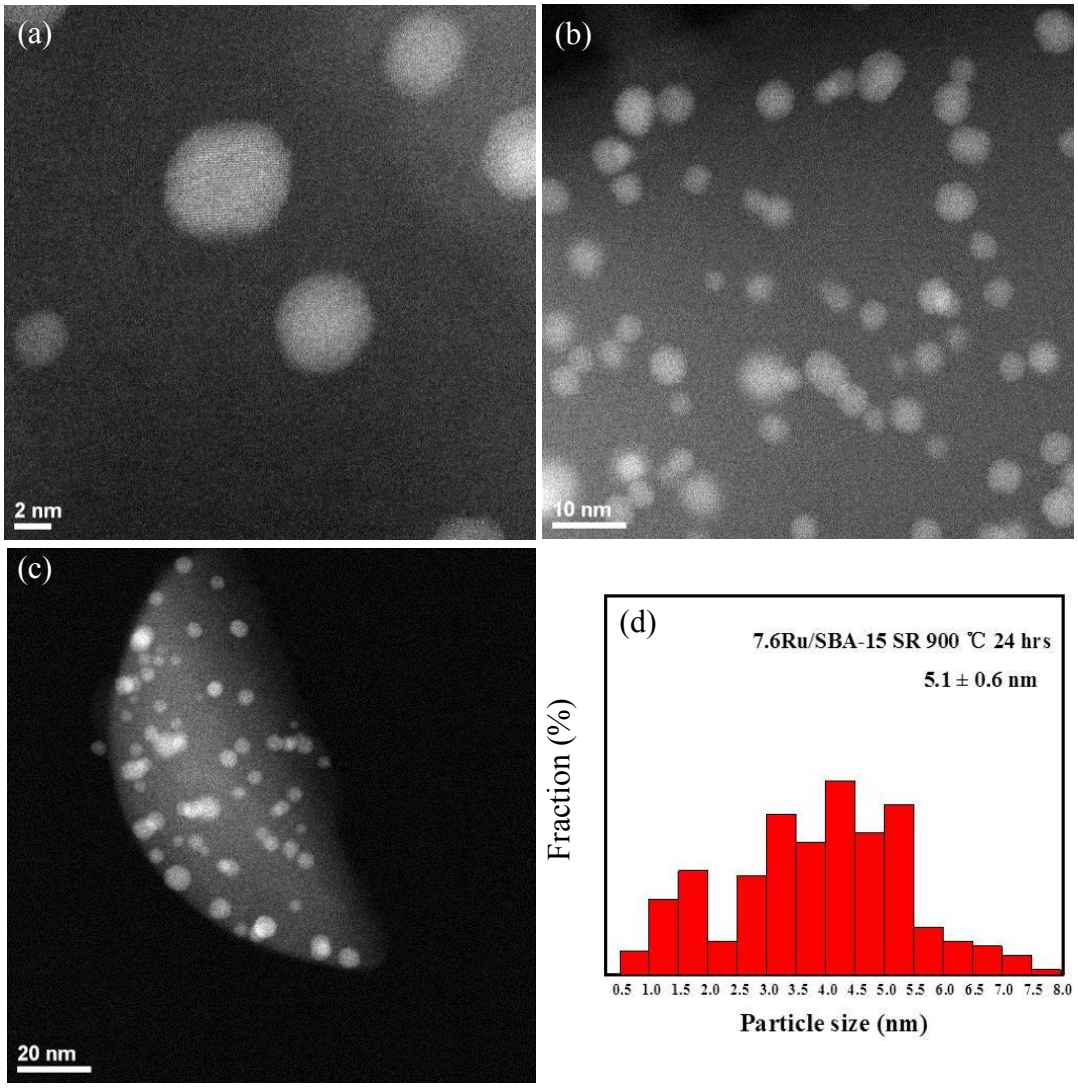

Figure 4.4. HAADF-STEM images of Ru/SBA-15 after steaming reduction (a-c) and Ru particle size distribution (d).

4.2.2 Particle size controlled by 'soft chemistry'

Platinum (II) tetraammine hydroxide ($Pt(NH_3)_4(OH)_2$, PTA-OH) and platinum (II) tetraammine nitrate ($Pt(NH_3)_4(NO_3)_2$, PTA-NO_3), purchased from Sigma Aldrich, were used as Pt precursors without any purification. As supports, SiO_2 Aerosil 300, Carbon Timrex, γ-Al_2O_3 SBa-200 and TiO_2 Hombikat were used. The high surface area TiO_2 was first calcined at 400°C for 4 hours to avoid structure collapse during reduction process; the

other supports were used as received. The properties of the supports, including PZC, BET surface areas and pore volumes are presented in Table 4.3.

All samples were synthesized by the method of Charge Enhanced Dry Impregnation (CEDI) as reported before [73]: PTA-OH or PTA-NO_3 was dissolved into a pore volume's worth of 1M NH_4OH. With the exception of the mesoporous silica support, the amount of metal used corresponds to the amount able to be adsorbed on the respective surface by electrostatic adsorption, or about 0.8 micromoles/m^2 for amorphous silica and titania (5 and 1 wt% respectively), and about 0.5 micromoles/m^2 for alumina and carbon (1 and 2 wt% respectively). For the very high surface area Al-dopes mesoporous silica, the metal content was limited to that of the amorphous silica to make 5 wt%. Sodium chloride (NaCl) was added into the solution to achieve Cl^- loadings from 0.1 to 1 wt%. After thorough mixing, the thick slurries were oven dried at 85°C for 2 hours to evaporate excess water. The dried powder was then reduced for 1 hour in 10% H_2/He at the optimal temperature determined by temperature programmed reduction (TPR), using a ramp rate of 5°C/min.

a) Silica Supports

A 5 wt% Pt/SiO_2 series were made by CEDI using different amounts of NaCl and $NaNO_3$ in the pH-adjusted PTA-OH solution for 0.1, 0.25, 0.5, and 1.0 wt% Cl^-, and 0.8, 1.7, and 3.4wt% NO_3^-. Cl^- and NO_3^--free samples were included as controls. XRD characterization of these samples is shown in Figure 4.5. Both salt-free control experiments show no XRD crystallinity, evidence that Pt particles less than 1.5 nm in size were prepared by CEDI. With increased amounts of residual ions, Pt diffraction peaks become discernable. In Figure 4.5a Pt particle size increased from <1.5 nm for the Cl^- free

control to 7.2 nm for the 1 wt% Cl^- sample. NaCl was detected in the two highest loadings of Cl^- (0.5 and 1.0 wt%).

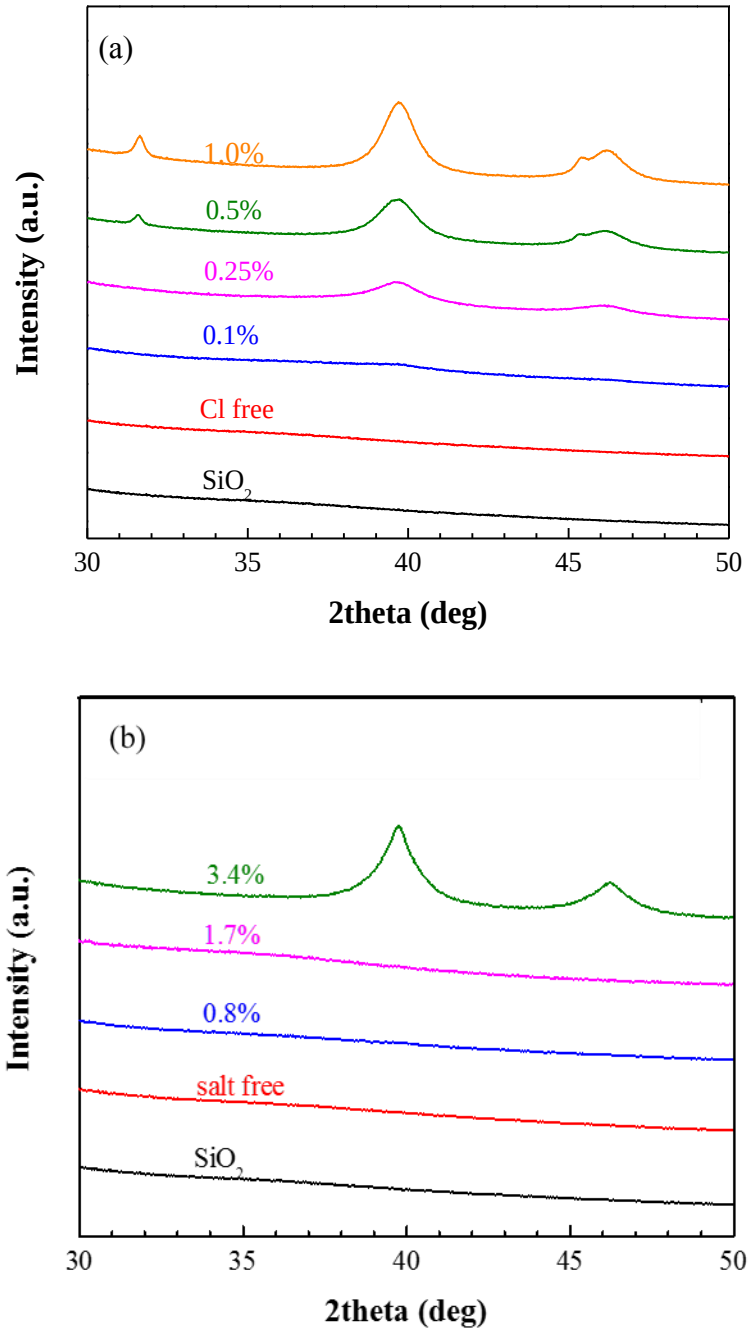

Figure 4.5. Salt effect on silica supported Pt particle size growth: Cl^- ions a) cause a stronger aggregation than NO_3^- ions b).

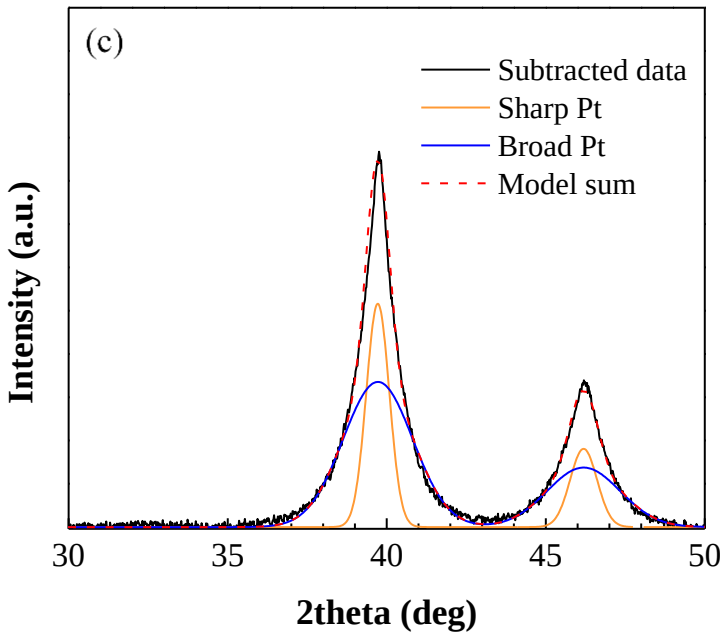

Figure 4.5.c) Pt deconvolution in 3.4% NO_3^- impregnated sample.

NaCl was replaced by $NaNO_3$ in the samples prepared by the same procedure and the XRD patterns of the reduced materials are shown in Figure 4.5b. The absence of $NaNO_3$ from XRD patterns at higher $NaNO_3$ loadings might be due to the lower melting point than that of NaCl. The effect of nitrate was milder than that of chloride, but at the highest loading particles of average size was seen to be 5.6 nm (with 1.7 and 0.8wt% NO_3^-, Pt particles remain small at 1.7 nm and <1.5 nm respectively). The nitrate-added samples contain much more sodium than the chloride samples but are smaller in size; this suggests that Pt aggregation is mainly affected by the Cl^- or NO_3^- anions and not cationic Na^+.

The unusual sharp top of the Pt (111) peak, seen with a closer inspection of the 3.4wt% NO_3^- sample in Figure 4.5b suggests that the particles have a bimodal size distribution, and in fact a fit for this sample in Figure 4.5c is well represented by a convolution of 3.3 and 10.1 nm particles. STEM characterization of the chloride free and a 0.25wt% chloride

containing silica supported sample supports the wider distribution as well as the particle size trend. Images and particle size distributions of these two samples are shown in Figure 4.6a and b. The chloride free sample has a relatively small average particle size and tight size distribution. With the addition of chloride, not only is the average size larger, but the size distribution is much broader. The STEM surface and volume size averages agree reasonably well with the chemisorption and XRD estimates for the silica supported samples, as summarized in Table 4.4.

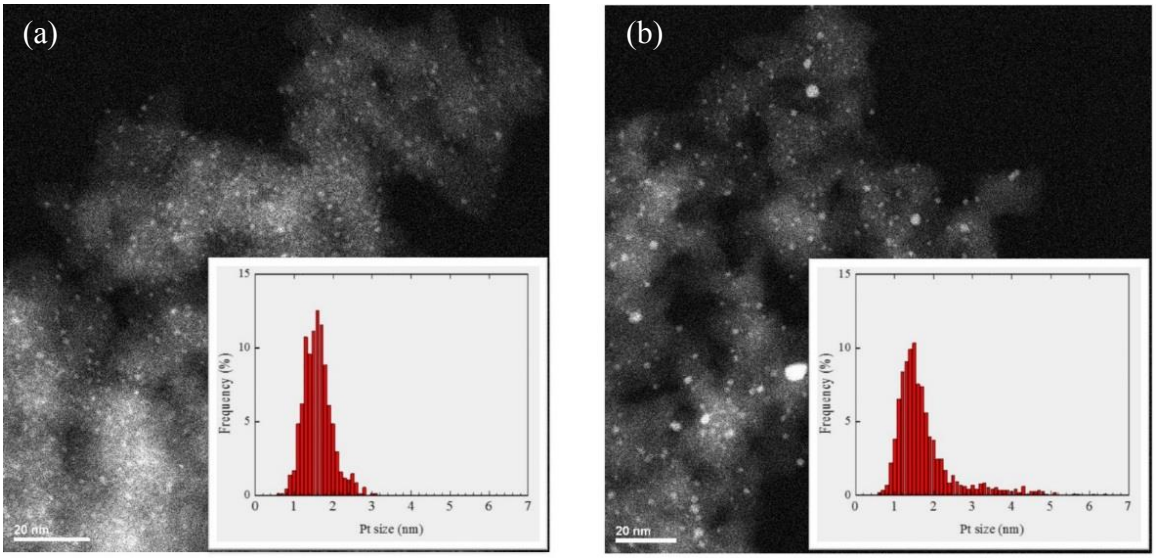

Figure 4.6. STEM images and particle size distributions for 5 wt% Pt/silica a) without chloride b) with 0.25 wt% chloride; insets are particle size distribution.

Temperature programmed reduction can be used to diagnose metal-support interactions [72, 113-115]. TPR profiles of the 5 wt% Pt/SiO_2 samples dosed with NaCl and $NaNO_3$ are shown in Figure 4.7. The addition of both salts causes the Pt precursor to reduce at lower temperature, and the chloride has greater effect than the nitrate. Thus the reduction temperature is inversely proportional to particle size: lower reduction temperature

translates to larger particle size. Reduction at lower temperatures might imply a weaker interaction of the precursor with the support surface, allowing more migration of Pt atoms during reduction.

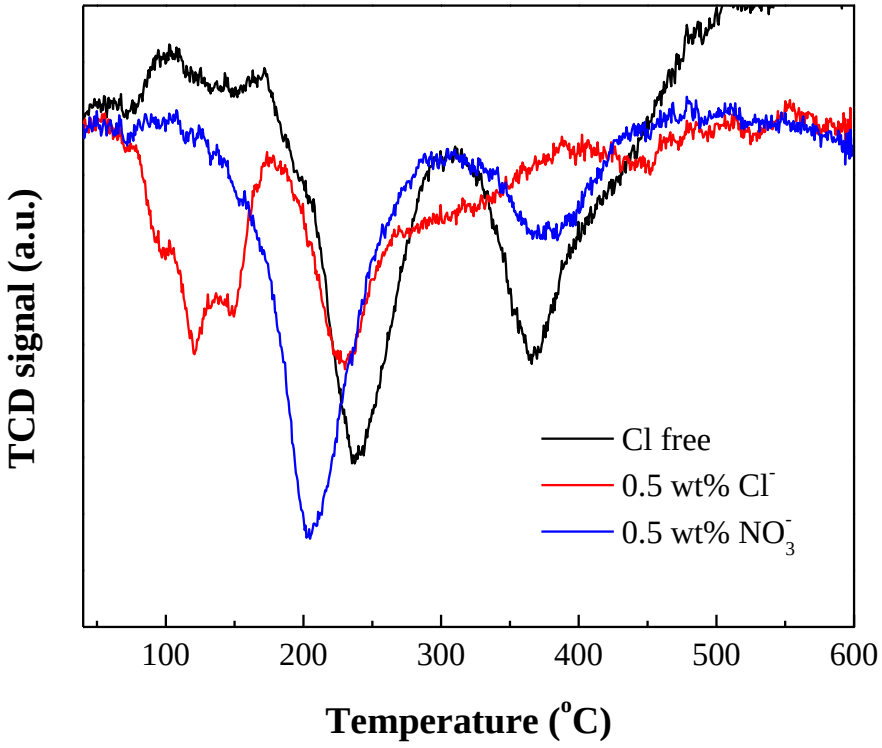

Figure 4.7. H_2 consumption at lower temperature was absent in $NaNO_3$-dosed and salt free samples.

a) Alumina and Al/Mesoporous Silica Supports

Series of SBa-200 Al_2O_3 and Al-doped SBA-15 mesoporous silica catalysts containing chloride in the same weight percents as the silica samples were synthesized via CEDI. Powder XRD characterization of these two series is shown in Figure 4.8a and b for the alumina and Al-doped SBA-15 supports respectively. As alumina's PZC is high, the electrostatic adsorption capacity for this material is low and a 1 wt% Pt loading was chosen

to stay within alumina's adsorption capacity. The Al/SBA-15 sample has the capacity to adsorb 7.7 wt% Pt; 5 wt% was used for the sake of comparison with silica.

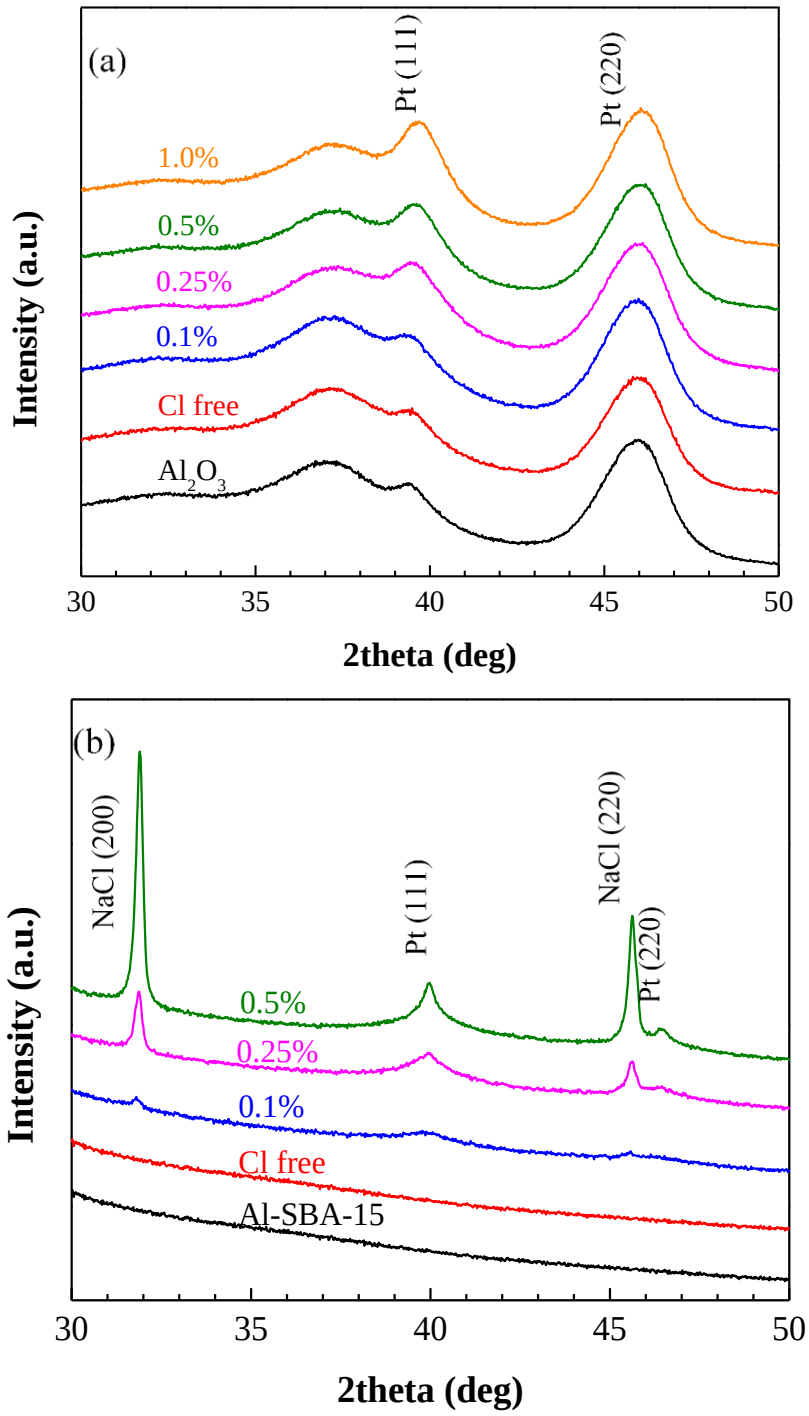

Figure 4.8. XRD patterns from CEDI-prepared series of NaCl-doped a) 1w%%Pt/Al_2O_3 and b) 5wt% Pt Al/SBA-15.

With Cl^- wt% increasing from 0.1 to 1.0 over the alumina (Figure 4.8a), fcc Pt peaks became evident. Size was estimated from the Pt (111) peak, which can be accurately deconvoluted from the (311) peak of the alumina support at 37.6° with the high sensitivity detector on the diffractometer [3] (A detailed discussion of this support subtraction and peak deconvolution procedure is given in the next section.). Size was estimated to increase from 1.8 to 5.6 nm as the chloride concentration increased (see Table 4.4). Crystalline NaCl was not detected by XRD in any sample likely due to the higher affinity of chloride for the alumina surface. The 5 wt% Pt Al/SBA-15 samples display more sensitivity to chloride concentration. The Pt nanoparticles are larger at equivalent chloride loadings even though they start out smaller in the chloride free sample (1.1 vs. 1.4 nm as confirmed by STEM in Figure 4.9). At 0.25 wt% Cl^-, the alumina support yielded 3.1 nm particles, whereas over Al/SBA-15 the particles grew to 6.1 nm.

STEM analysis on these samples was performed to gauge the effect of chloride on particle size and also on breadth of size distribution. Representative STEM Z-contrast images and particle size distributions (insets) are shown in Figure 4.9a and b for the chloride free and chloride containing alumina support, and Figure 4.9c and d for the chloride free and chloride containing SBA-15 catalyst. The smaller average size of the chloride free sample on Al/SBA-15 is confirmed (1.1 to 1.4 nm) and the 0.1 wt% Cl^- Al/SBA-15 sample size, at 2.7 nm, is almost as large at the 0.25 wt% Cl^-, alumina supported sample at 3.5 nm. Furthermore, the wider distribution of both chloride-containing samples is seen.

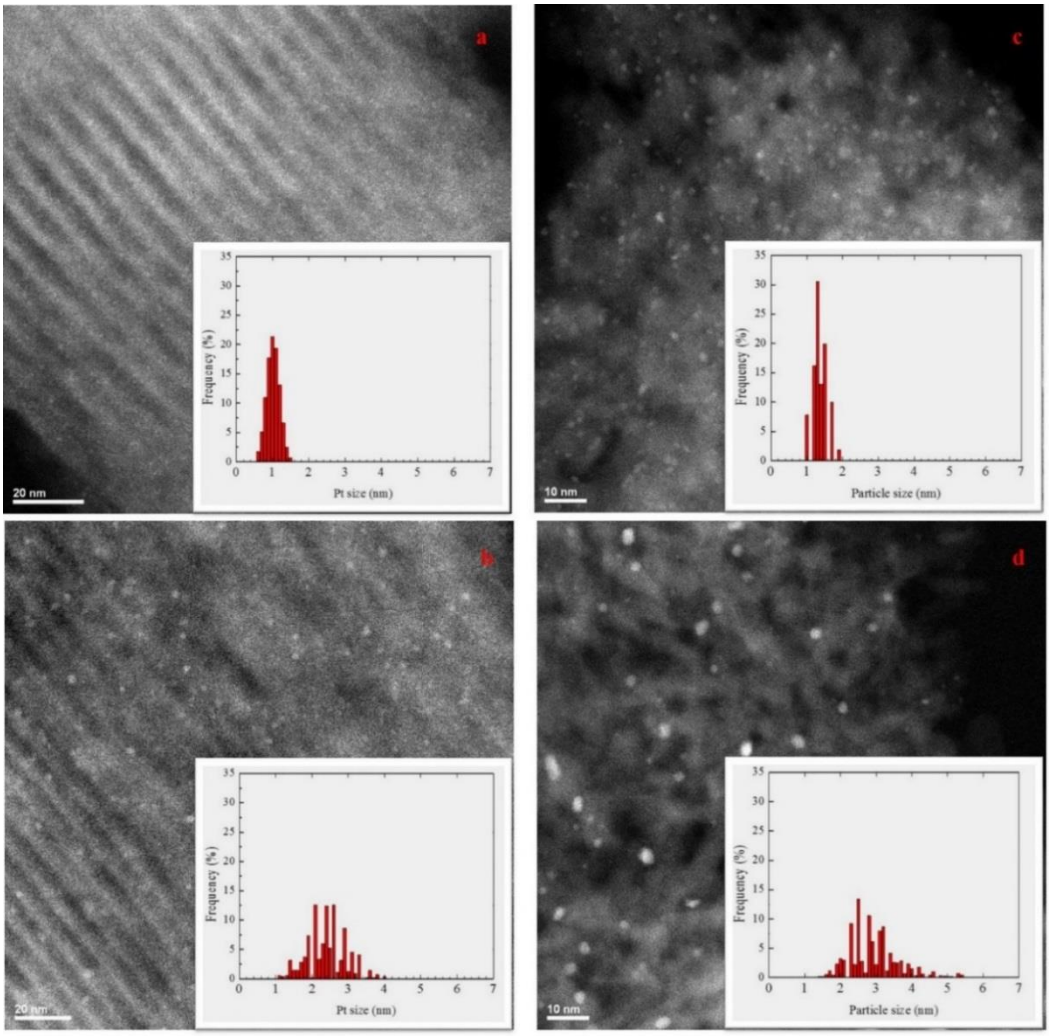

Figure 4.9. Wider particle size distribution with presence of Cl^- in 1wt% Pt/Al_2O_3 (d), 5wt% Pt/Al-SBA-15 (b) than their salt free counterparts (c and a).

The agreement of XRD, chemisorption, and STEM particle size estimates is quite satisfactory. The values given in Table 4.4 for the silica and alumina supports show good overlap between the methods. It is interesting that for the silica support, XRD size estimates are higher than chemisorption estimates, while for alumina, chemisorption estimates are higher than XRD estimates. A possible explanation is that the Cl^-, more

strongly adsorbed over alumina, transports from alumina to Pt in a reducing flow [116], blocking sites and leading to less H_2 chemisorption.

Table 4.4. Summary of Pt size on SiO_2, Al_2O_3, and Al-SiO_2 determined by different techniques.

	5 wt% Pt/SiO_2				
	XRD	Chem	STEM (nm)		
Cl^- wt%	(nm)	(nm)	Dv	Ds	Dn
0	<1.5	1.5	1.9 ± 0.4	1.8 ± 0.4	1.6 ± 0.4
0.1	<1.5	2.0	-	-	-
0.25	4.4	3.6	4.0 ± 2.4	2.9 ± 1.5	1.8 ± 0.9
0.5	6.1	4.6	-	-	-
1.0	7.2	6.6	-	-	-
	1 wt% Pt/Al_2O_3				
	XRD	Chem	STEM (nm)		
Cl^- wt%	(nm)	(nm)	Dv	Ds	Dn
0	1.5	1.8	1.4 ± 0.2	1.4 ± 0.2	1.4 ± 0.2
0.1	1.8	3.3	-	-	-
0.25	3.1	3.7	3.5 ± 0.9	3.3 ± 0.8	2.9 ± 0.7
0.5	4.3	5.3	-	-	-
1.0	5.9	5.6	-	-	-
	5 wt% Pt/Al-SBA-15				
	XRD	Chem	STEM (nm)		
Cl^- wt%	(nm)	(nm)	Dv	Ds	Dn
0	<1.5	-	1.1 ± 0.2	1.1 ± 0.2	1.0 ± 0.2
0.1	2.9	-	2.7 ± 0.9	2.6 ± 0.7	2.4 ± 0.5
0.25	6.1	-	-	-	-
0.5	6.9	-	-	-	-

b) TiO_2 and Carbon Supports

XRD was used to analyze the effect of chloride on two further supports, titania and carbon (See Table 4.3 for properties); these results are shown in Figure 4.10a and b respectively. To stay below the electrostatic uptake limit, 2 wt% Pt/C and 1 wt% Pt/TiO_2 were prepared. 1 wt% Pt/TiO_2 samples were reduced at 350°C, while the 2 wt% Pt/C series were reduced at 300°C to avoid methanation of the support.

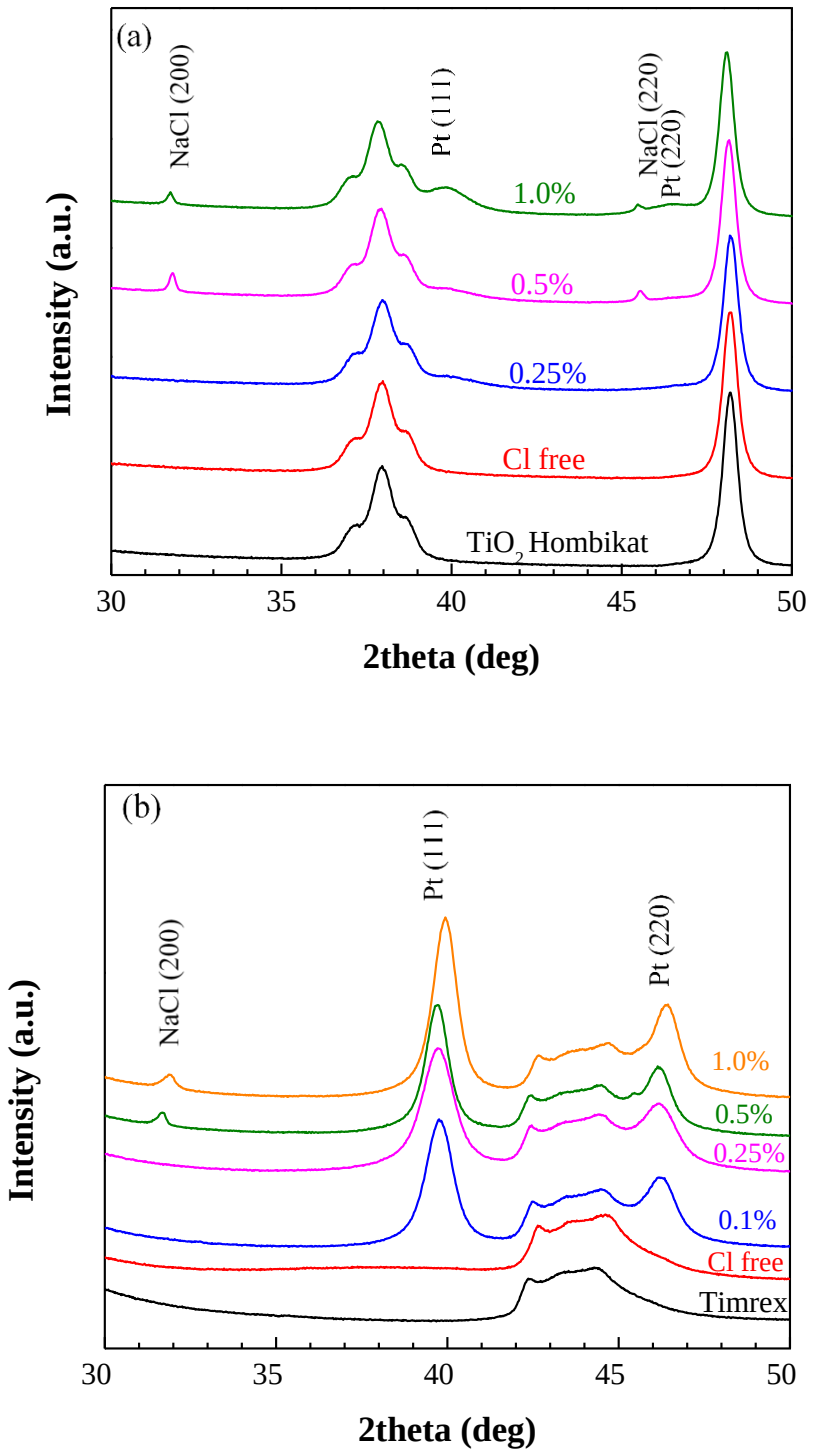

Figure 4.10. XRD patterns from CEDI-prepared series of NaCl-doped a) 1 wt% Pt/TiO_2 and b) 2 wt% Pt/C.

Sodium chloride crystals accumulated over both supports at high salt loadings. The pure anatase phase of titania is evident in Figure 4.10a, while peaks for graphitic carbon are evident for the Timrex material. In both of these chloride free samples, Pt particles were below the limit of detection by XRD. With increasing NaCl, Pt particles grew up to 5.1nm on TiO_2 (Figure 4.10a) and up to 11 nm on carbon (Figure 4.10b). Of all the supports, carbon showed the greatest sintering sensitivity to chloride. Detailed Pt size determined by XRD are summarized in Table 4.5.

Table 4.5. Summary of Pt size on carbon and titania.

Cl^- wt%	**2 wt% Pt/C**	**1 wt% Pt/TiO_2**
	XRD (nm)	XRD (nm)
0	<1.5	<1.5
0.1	11.0	-
0.25	8.2	3.5
0.5	7.9	3.7
1.0	10.5	5.1

A comprehensive comparison of support sensitivity to chloride-induced precursor sintering is made in Figure 4.11 by plotting the particle size versus Cl^-/Pt ratio for each support. Size increases most rapidly for the carbon support tested, and almost as rapidly for the Al doped SBA-15. Silica is also quite sensitive, not surprisingly like the Al doped mesoporous silica. The supports which appear to best anchor the tetraammine precursor against sintering in the presence of chloride during reduction are alumina and titania. Continuing research is underway to understand the mechanism of nanoparticle genesis

from adsorbed precursors and how it is affected by residual anions. One possible factor is the presence of hydroxyl groups serving as anchors to the metal particles; it is believed that the density of hydroxyl groups affects the rate of aggregation [101]. This would fit the observed trend reported here; alumina and titania are thought to have relatively high hydroxyl densities, of 8 and about 10 OH/nm^2 respectively [117-118], values of 5 OH/nm^2 are typically cited for silica [81, 119], and graphitic carbon has relatively little oxygen surface functionalities [120]. In Figure 4.12, Pt particles sintering is correlated with OH densities on various supports with same Cl^- loading (0.5wt% Cl^-). Pt particles sintered up to 8 nm on carbon and remained relatively small (3.7 nm) on TiO_2. Al-SBA-15 is assumed to possess the same OH density as SiO_2 since the Al loading is very low.

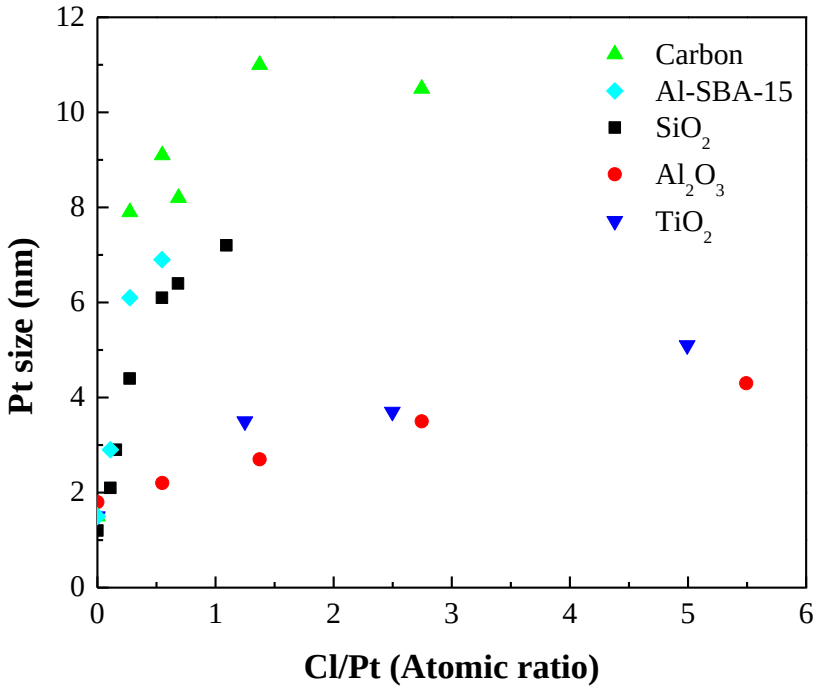

Figure 4.11. Pt particle size versus Cl/Pt ratio for all supports studied.

An alternate explanation of the effect of Cl^- could be electric double layer compression. This is a key feature of the strong electrostatic adsorption mechanism we have employed in the past [72-73, 75-76]. The presence of Cl^- or NO_3^- at the adsorption layer might reduce the strength of the precursor-support interaction by locally increasing ionic strength. However, if this was the case, the supports with relatively low pore volume, C, Al_2O_3 and TiO_2 (pore volumes are shown in Table 4.3) would experience higher ionic strength and greater weakening of electrostatic interaction, and more sintering. This is not observed: Al_2O_3 and TiO_2 show the best ability of anchoring Pt precursor at higher ionic strength.

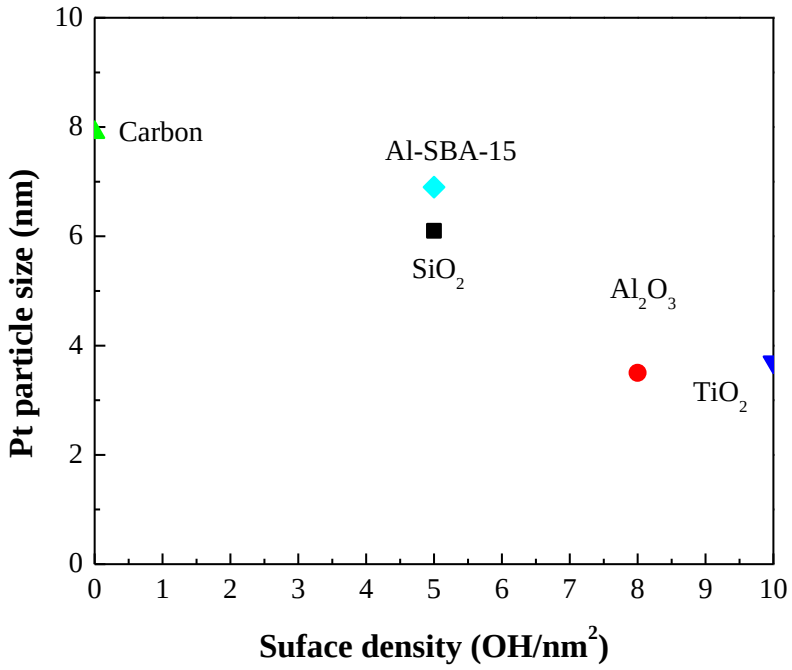

Figure 4.12. Cl^- effect on Pt sintering related with hydroxyl group densities on various supports.

As a practical matter, for the purpose of testing the dependence of reactivity on particle size, it would be best to have a monodisperse size distribution. While the ion-free

samples do possess a relatively tight size distribution, this is not the case for the larger sizes. Research on the production of more monodisperse sizes is continuing; it is hoped that further insight into the mechanism of nanoparticle formation and growth in the presence of residual ions will allow this finer level of control to be achieved.

4.2.3 Supported Pt Particle Size Determination by Powder XRD with High Sensitivity Silicon Slit Detectors

The enhanced sensitivity of silicon strip detector has been reported in literature [3]: a series of Au catalysts supported on carbon were prepared at various weight loading (0.33 to 3.0 wt%) by strong electrostatic adsorption (SEA) which is a simple and reproducible method to synthesize small nanoparticles [3, 70, 76], and characterized by both standard scintillation detector and silicon strip detector (D/teX Ultra), 1.3 nm Au particles were detected only by D/teX Ultra in 1 wt% Au/Carbon and the small particles were consistent with that from HRTEM which is 1.2 nm. In this paper, we demonstrate that the higher accuracy of Si slit detector is extendable to supported Pt particles.

The series of Al_2O_3 supported Pt catalysts synthesized in Chapter 4.2.2 were characterized by powder XRD. The superposition between Al_2O_3 and Pt peaks renders complexity to particle size calculation. With the smooth data collected by high sensitivity silicon slit detector which allows an improved signal to noise ratio to detect particles around 1 nm, Pt (111) peak ($2\theta=39.76^o$) can be deconvoluted from the γ-Al_2O_3 background, boehmite and Pt_3O_4 to yield particle sizes within the range of 1.8 to 4.3 nm. The results are compared with STEM and H_2-Chemisorption. Another example of Pt/Mo_2C also illustrates the accuracy of deconvolution. In this chapter, we demonstrate that the latest generation XRD detector provides a simple and quick way to determine Pt particle size

supported on alumina and molybdenum carbide. Meanwhile, genesis of transitional alumina during the synthesis of catalysts is revealed.

Mo_2C was synthesized by a temperature programmed reaction method previously developed [121-122]. Ammonium molybdate (para) tetrahydrate ($(NH_4)_6Mo_7O_{24}.4H_2O$, 81-83% as MoO_3, Alfa Aesar) was sieved to obtain particle sizes between 125 and 250 µm. The Pt solution contained 500 ppm Pt using PTA-OH precursor and was sparged with He for 20 min prior to addition of Mo_2C. With continuous He sparging, the support could contact the solution for 5h while stirring every 15-20 min. Solution was then poured out and analyzed by ICP to determine amount of Pt deposition. Remaining sludge was transferred back to quartz tube and dried under H_2 flow, followed by passivation as mentioned in supportive materials. 5.4 wt% Pt/Mo_2C was prepared as described.

As seen from Fig 4.13a to e, Pt particles are gradually growing bigger with NaCl loading increase, volume-based diameters are increasing from 2.1 nm (0.1 wt% Cl^-) to 5.1 nm (1.0 wt% Cl^-), which will be compared with XRD results later. Dv, Ds and Dn are listed in Table 4.6. Besides the evident increasing trend, as NaCl is doped, particle shape is becoming irregular and particle size distribution is turning into broader, standard deviations increase from 0.5 (0.1 wt% Cl^-) to 1.2 nm (1.0 wt% Cl^-). In Fig. 4.13e, Pt particles are in bimodal, both small (1-2 nm) and large (5-8 nm) particles can be seen.

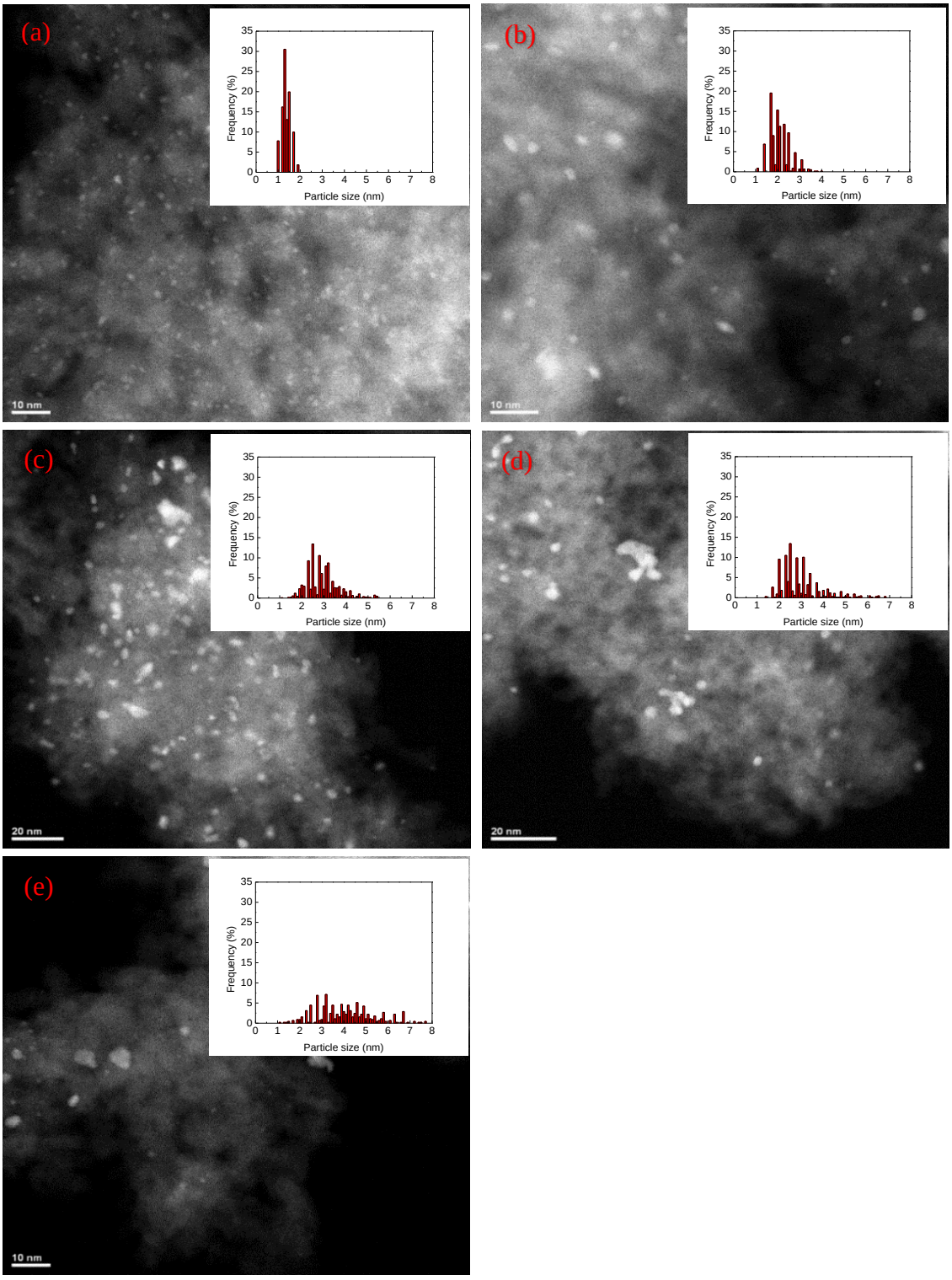

Figure 4.13. STEM of 1 wt%Pt on γ-Al_2O_3 with a) 0 wt%, b) 0.1 wt%, c) 0.25 wt%, d) 0.5 wt% and e) 1.0 wt% Cl^-, insets are Pt particle size distribution.

Results from H_2-chemisorption are gathered in Table 4.6. A pronounced difference between D_S and D_{chemi} can be noticed on four Cl^- added samples, particle sizes estimated by H_2 chemisorption are larger than those by STEM, in the sample with 0.5 wt% Cl^-, D_{chemi} is almost 1.5 times larger than D_S. On the other hand, in the Cl^- free sample, D_S and D_{chemi} match very well with each other. The striking discrepancy is also observed in fuel cell. It is believed that Cl can block Pt surface therefore leading to a low reactivity [123]: when H_2PtCl_6 was deposited onto carbon by strong electrostatic adsorption, a lower dispersion was derived from CO chemisorption than TEM, and reactivity was increasing after Cl was removed in post treatment in He flow at higher temperature (up to 750°C); Cl contamination was also reported when tetrochloroethylene which would decompose under redox condition was introduced to Pt/C, resulting in a significant loss in Pt surface atom availability [124]. In this work, it is assumed that chloride ions (from NaCl) impregnated during synthesis remain on the metal surface after 350°C reduction in H_2 flow, and more Cl^- added, more loss in accessible surface Pt. Cl poisoning may occur resulting in a discrepancy in particle size determination between STEM and H_2 or CO chemisorption. Further investigation on location of Cl^- adsorption may help to explain why the difference between D_S and D_{chemi} shrinks in 1.0 wt% Cl^- sample.

All five samples along with pure γ-Al_2O_3 were reduced in H_2 flow and then characterized by D/tex detector. The XRD patterns of Cl^- impregnated Pt/Al_2O_3 in Fig. 4.8a are presented here again as reported in previous publication [78], and dash lines are showing the position of Pt peaks. Compared with pure support pattern, the one without Cl^- impregnation shows barely no difference, indicating Pt particles are highly dispersed onto the surface of Al_2O_3 via the method of CEDI. As increasing the Cl^- loading in the sample,

the intensity of peak located at 39.7° which is assigned as Pt (111) is gradually increasing, and larger Pt particles are expected, but it is still masked by the (222) peak of the gamma alumina. Therefore, background subtraction and peak deconvolution are necessary to yield accurate Pt particle sizes.

Table 4.6. Pt particle size determination by different techniques.

	D_n	σ	D_s	D_v	D_{chemi}	D_{XRD}
Cl free [28]	1.4	0.2	1.4	1.5	1.8	1.8, 2.2*
0.1 Cl	2.1	0.5	2.3	2.4	3.3	2.2, 2.1*
0.25 Cl [28]	2.9	0.7	3.3	3.5	3.7	2.7, 1.7*
0.5 Cl	3.0	0.9	3.6	4.0	5.3	3.5, 1.8*
1 Cl	4.0	1.2	4.7	5.1	5.6	4.3, 1.8*
Pt/Mo_2C	-	-	-	-	-	5.0

With the utilization of D/tex detector, a smooth XRD pattern was achieved, which is the premise to following deconvolution and obtain reasonable HWHM values. Supports' patterns were subtracted from all Pt deposited samples using Fityk software. Pt (111), (200) and (220) were fit using Gaussian to achieve FWHM values and particle size were calculated by Scherrer equation with a shape factor of 0.94. The detailed subtraction and deconvolution procedure is described in Figure 4.14.

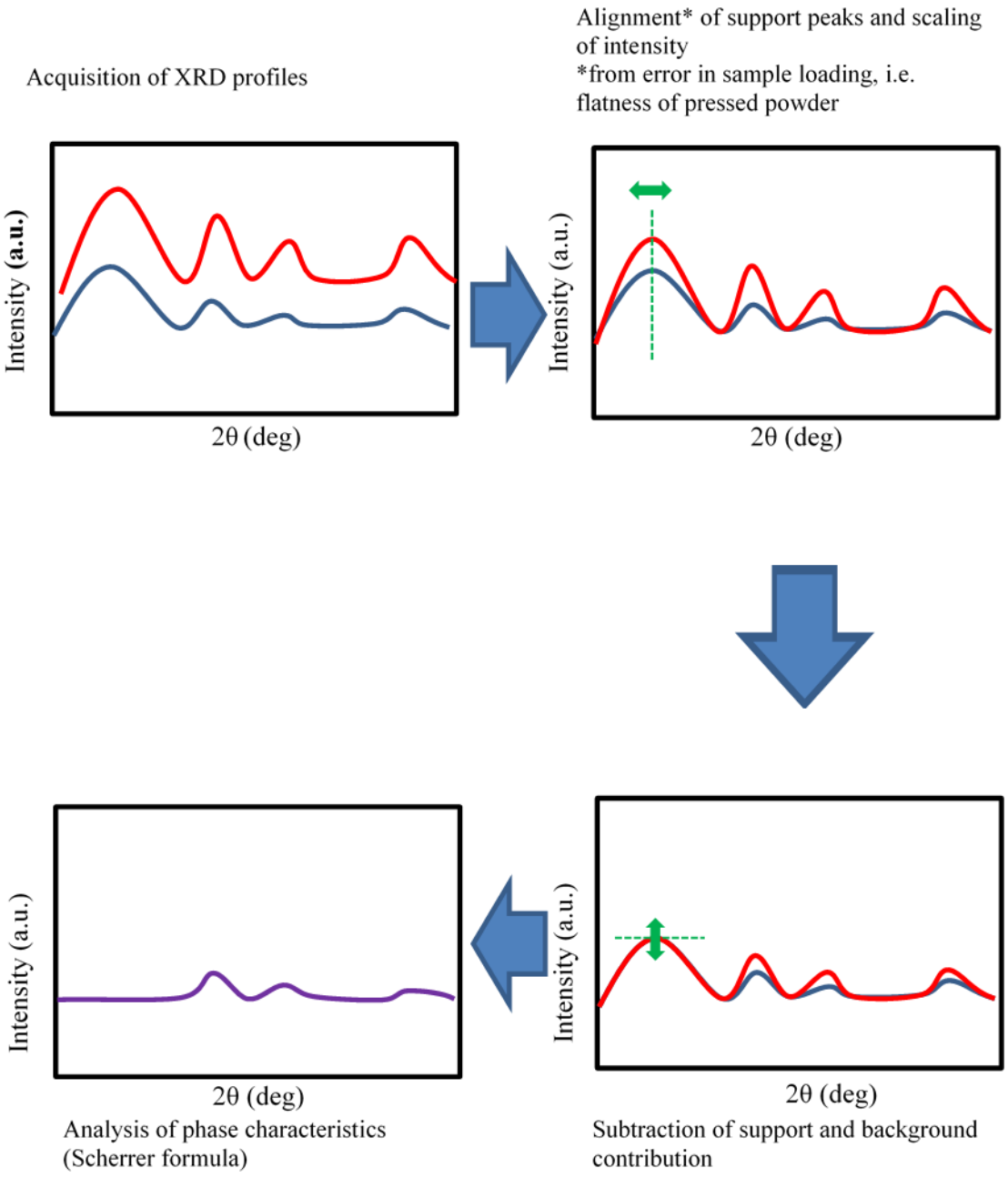

Figure 4.14. Schematic diagram of deconvolution on Fityk.

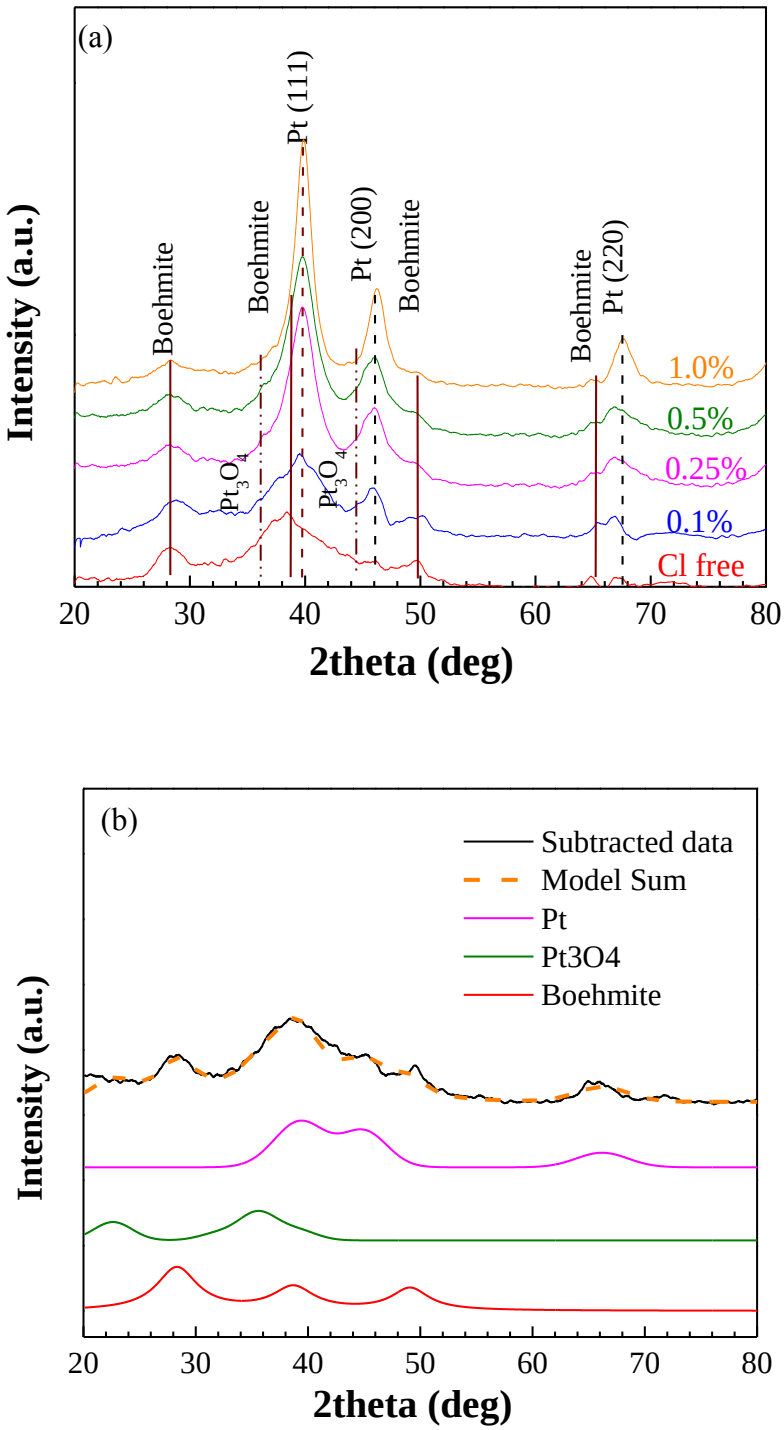

Figure 4.15. Background-free XRD patterns of Cl^- impregnated Pt/γ-Al_2O_3 a), example of deconvolution of Pt from boehmite and Pt_3O_4 in the sample with 0.5 wt% Cl^- impregnated b) and Cl^- free catalyst; dash lines: Pt.

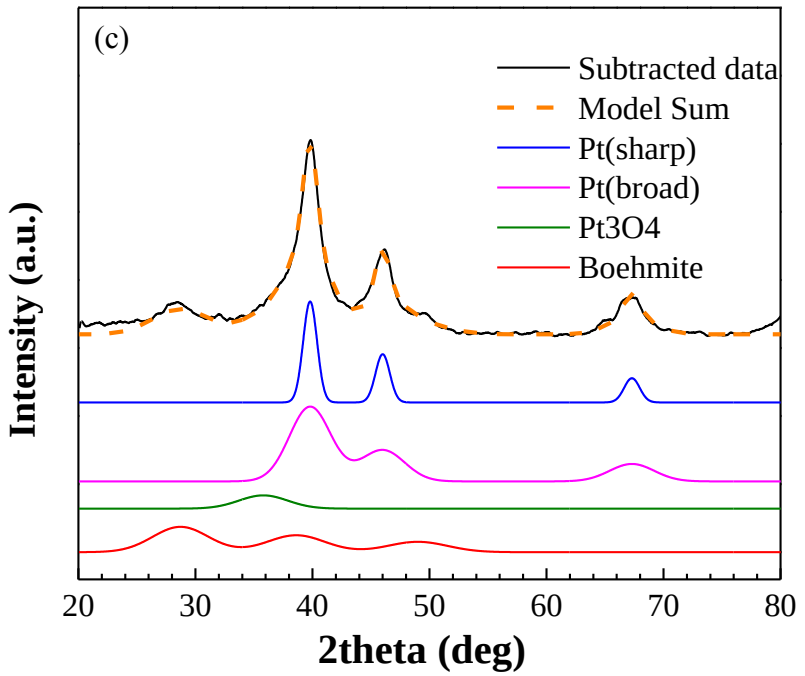

Figure 4.15.c) Background-free XRD patterns of Cl^- free catalyst. Solid lines: boehmite; dash lines: Pt.

The background-free patterns (Figure 4.15a) were obtained by following the same procedure as described in Figure 4.14. Estimated from Scherrer equation, Pt particle sizes range from 1.8 to 4.3 nm with 0-1 wt% Cl^- impregnated in the sample. Like wide distribution in STEM results, bimodal distribution was observed in those samples impregnated more than 0.10% Cl^-: 4.5 and 1.6 nm, 6.3 and 2.1 nm7.3 and 2.4 nm. The weighted average size is presented in Table 4.6. Meanwhile, Pt_3O_4 was also noticed (Fig. 4.15b and c), which was consistent with our recent submitted paper that Pt particles smaller than 2.5 nm are easily to be oxidized at room temperature leading to a mixture of metallic Pt, Pt_3O_4 shell-Pt core and pure Pt oxide [125]. Similarly, the Pt oxides in this case were from the oxidation of smaller Pt particles. Due to the smaller size (1.8 nm, entry 4 in Table 4.6) in the 0.5% Cl^- impregnated catalyst, only one Pt_3O_4 diffraction located at 36° was

considered (Figure 4.15b); whereas two were taken into consideration in Cl^- free sample due to the larger size estimation as 2.2 nm (Figure 4.15c).

As demonstrated in Fig. 4.15b, three broad peaks other than three Pt diffractions became discernible in all patterns, located at 28°, 38° and 50° (solid lines in Fig. 4.15b) which are indexed as phase transitional alumina. The indiscernible transitional alumina peaks in original patterns indicate a minor phase transition during Pt catalysts synthesis. The appearance of the phase transition in the subtracted patterns signifies the low noise/signal ratio of D/tex detector. In Tettenhorst's work [126], boehmite was the only alumina hydrate shown in a series sample prepared from room temperature to elevated temperature and dried in oven; At lower temperature, XRD patterns showed broadened diffraction peaks with low intensity which were considered as finely crystallined beohmite.

In the control experiments, where pure γ-alumina was impregnated with 1M NH_4OH with same following treatments as Cl^- doped series, there barely no difference from the fresh alumina can be observed in the raw patterns (Fig. 4.16a); the hydrated phase revealed by subtracting fresh γ-alumina pattern in the oven-dried sample (Fig.4.16b, red pattern); and the disappearance of transitional boehmite (Fig. 4.16b, blue pattern) in the sample reduced at indicates that complete dehydration occurred at such conditions. It is assumed that 1M NH_4OH solution speeds up the hydration of γ-Al_2O_3 to form oxi-hydroxide (AlO(OH)), the base facilitation has been reported previously [127]; then the majority of transitional alumina transforms to γ-Al_2O_3 during the H_2 reduction at 350°C. While in the series with deposition of Pt particles, dehydration of boehmite is believed to be retarded, especially where is in close vicinity of metal particles, leading to the occurrence of boehmite in the XRD patterns even after reduction at higher temperature.

When taking a close look at the boehmite signals in Figure 4.15a, from bottom to top, we observed that the intensity of boehmite signals decreased with Pt size, which is consistent with the assumption, the less Pt blockage resulting from reduced perimeter cause less boehmite retention.

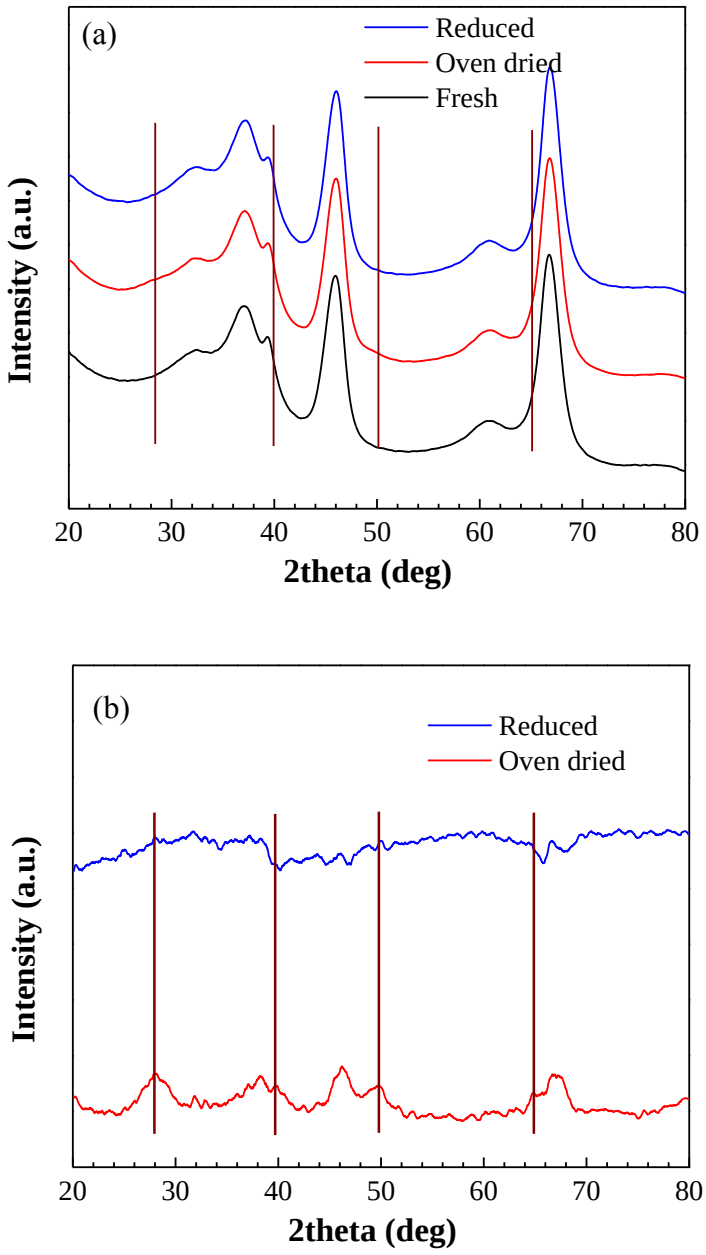

Figure 4.16. a) NH_4OH impregnated γ-Al_2O_3 subjected to low and high temperature treatment; b) Hydration and dehydration of γ-Al_2O_3.

It has been reported that chemisorption cannot be used to determine metal size in Pt/Mo_2C where chemisorption of typical probe molecules (H_2 and CO) proceeded non-selectively [122], on the other hand, powder XRD technique shed the light on Pt size determination in the case of 3.0wt%Pt/ Mo_2C. XRD patterns of Pt/Mo_2C and deconvolution are presented in Fig. 4.17. The self-synthesized molybdenum carbide shows a typical pattern of β-Mo_2C as reported in literature [128-129]. Dash lines are where Pt peaks are located. Pt particle size is uncertain regardless of the manifest signal increase at 39.7° in the pattern of Pt/Mo_2C. Followed by the same procedure, Pt peaks are deconvoluted from Mo_2C (Fig. 4.17b) and reveal a bimodal particle size distribution (Fig. 4.17b), 8.2 nm and 2.7 nm from Scherrer equation with average size of 5.0 nm. A broad hump shows up in the range of 20-38° can be assigned to the phase transformation during thermal treatment of sample.

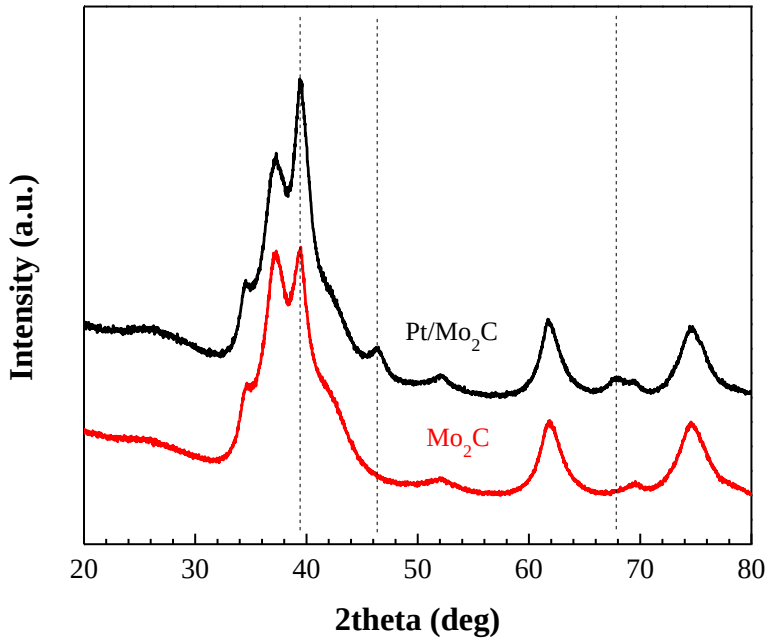

Figure 4.17.a) Example of Pt size determination in Pt/Mo_2C: Pt (111) diffraction overlaps with Mo_2C (101).

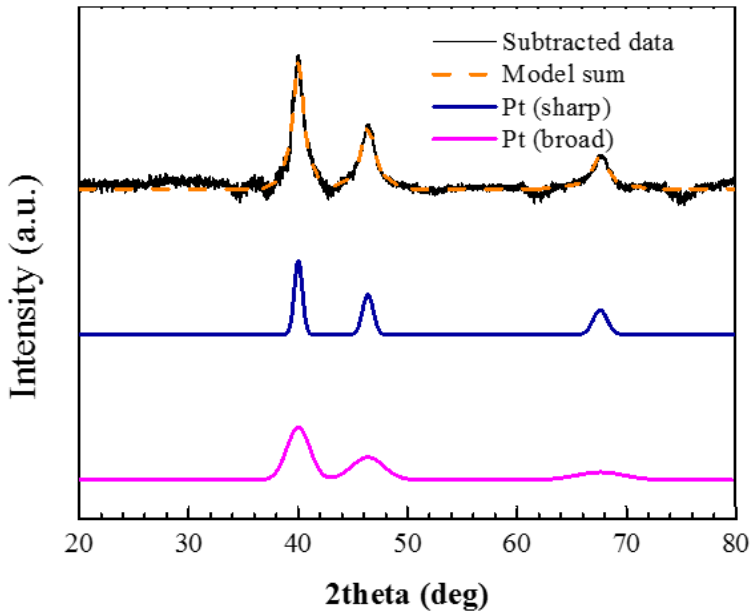

Figure 4.17.b) Example of Pt size determination in Pt/Mo_2C: Pt bimodal distribution after Mo_2C subtraction and deconvolution. Dash lines: Pt diffractions.

4.3 Conclusion

In conclusion, supported Pt and Ru nanoparticle size series were synthesized by using strong electrostatic adsorption procedure followed by two thermochemical treatments. A high temperature steam reduction yielded particles from 1.1 nm to 4.5 nm. However, the steaming reduction procedure significantly affects the pore structure of SBA-15 and drastically reduces the surface area. A lower temperature oxidation – reduction procedure better preserves the support and gives a good size distribution of Pt nanoparticles, but cannot be effectively used with Ru due to ruthenium oxide volatilization.

CEDI is a simple and reproducible method to deposit ultra-small metal particles on oxides as well as carbon. It has been demonstrated that the Pt aggregation is caused by Cl^- and NO_3^- anions and not Na^+ cations. Compared with NO_3^-, Cl^- accelerates Pt particle growth more. A series of Pt catalysts with controlled particle size by doping NaCl are

synthesized on SiO_2 (1.5~7.2 nm), Al-modified SiO_2 (1.1~6.9 nm), TiO_2 (1.5~5.1nm), and Al_2O_3 (1.5~5.9 nm). The Cl^- effect is most pronounced on carbon; with 0.1wt% Cl^-, Pt particle size increased to 8 nm and reached a plateau of around 10 nm. Pt particle size is correlated with the atomic ratio of Cl^-/Pt. This ratio is more important to Pt agglomeration than absolute Cl^- loading. A more gradual increase in Pt size with Cl^-/Pt was observed in Al_2O_3 and TiO_2 supported catalysts. Further investigation into the "soft chemical" control of nanoparticle size is being made, including efforts to synthesize larger particles with more monodisperse size distributions.

With the application o f D/tex detector, ultra-small metal particles (1.5 nm Pt) became detectable in XRD pattern which were invisible under conventional detector, and smooth patterns were guaranteed. Highly dispersed and uniform Pt particles were deposited onto γ-Al_2O_3 by the method of CEDI. A series of catalysts with various Pt particle sizes (from 2-5 nm) were prepared by controlling Cl^- loading during synthesis. XRD patterns confirmed the growth of Pt particles, and accurate Pt particle sizes were obtained by Pt (111) deconvolution of smoothed XRD pattern from γ-Al_2O_3 (222) and boehmite. Pt particles were assumed to prevent complete dehydration of transitional alumina which presented in the background-free patterns. The deconvoluted results were consistent with STEM: D_{XRD} matched volume-averaged particle size (D_V) of STEM, and the discrepancy between surface-averaged particle size and H_2-chemisorption might result from chloride contamination. Pt peaks were deconvoluted from Mo_2C and showed a bimodal particle size distribution in the sample of 3.0wt% Pt/Mo_2C. Further investigation needs to be proceeded to study the mechanism of chloride ions effect on metal particle growth.

Chapter 5

Rational synthesis of Pd bimetallic catalysts for furfural conversion

5.1 Introduction

With diminishing non-renewable fossil resources, the production of hydrocarbon fuels and chemicals from renewable biomass resource has become more pressing in recent decades [27, 29, 130]. Furfural ($C_5H_4O_2$), produced from acid-catalyzed hydrolysis and dehydration of hemicellulose in lignocellulosic biomass [27-28], is considered a key platform molecule in biomass conversion. With multiple functional groups, furfural can be catalytically transformed into a variety of valuable chemicals through various routes [29], including furan, tetrahydrofuran, 2-methyl furan, 2-methyl tetrahydrofuran, furfuryl alcohol (FAL), tetrahydrofurfural alcohol(THFAL), cyclopentanone (CPO), and cyclopentanol (CPL).

Cyclopentanone (CPO), a cyclic ketone, is a key intermediate chemical in the production of pharmaceuticals, fragrances and cosmetics, rubber chemicals and agrochemicals. CPO can be prepared by various methods from multiple materials [131] and it is traditionally produced from adipic acid at 285-295°C in the presence of barium hydroxide, followed by distilling, extracting with ether and fractionating [132]. Driven by the rapid growth of pharmaceutical industry, the global demand for cyclopentanone market was valued at USD 100.0 million in 2014, and is expected to reach USD 130.0 million in 2020 [33]. As one of the downstream products of furfural hydrogenation, the production of

CPO from biomass based FFA might be an efficient way to expand the industrial application of biomass.

FFA conversion has been widely reported in literature, including decarbonylation to furans [34], hydrogenation to alcohols [35-36] and rearrangement to ketones [133]. Bimetallic Pd-based catalysts have recently been employed for these reactions, with the idea being that noble metal catalyzes hydrogenation and base metal sites participite C=O activation. However, little effort has yet been expended to optimize these catalysts. The purpose of the work reported here is to demonstrate the effectiveness synthesis aimed at maximizing overall metal dispersion and metal1-metal2 interactions.

Strong Electrostatic Adsorption (SEA) has been reported as an effective way to prepare highly dispersed nanoparticles on oxides and carbon [70, 72, 76]. In SEA, hydroxyl groups populating on the surface of support are protonated/deprotonated by adjusting the pH of the solution in contact with support away from its neutral point (the Point of Zero Charge, PZC), and exploiting the electrostatic interaction which occurs between the charged support and oppositely charged metal precursor. The optimal conditions where maximum metal uptake occurs can be determined in a metal uptake vs. pH survey. The strongest interaction between support and precursor rendered from SEA leads to a lessened migration of during thermal treatment to remove ligands, which results in smaller catalysts. SEA can be extended to prepare bimetallic catalysts: introducing a secondary metal precursor complex in the solution, simultaneous adsorption of two precursors occurs, and bimetallic catalysts with homogeneously alloyed nanoparticles are formed, as has been demonstrated for PtPd silica and carbon supported catalysts [82-83].

A method to make core-shell bimetallic catalysts is electroless deposition (ED), through which a shell metal is deposited in partial or multi-monolayers on a core metal (which itself can be synthesized at high dispersion by SEA). Placing a second metal exclusively as a partial shell on a first metal core offers the ability to synthesize true bimetallic surfaces with no particles of each of the monometallic components. ED proceeds catalytically or autocatalytically whereby a shell of controllable coverage of metal can be deposited selectively onto pre-existing core particles (or seed nuclei) of a pre-existing metal. The solution phase reducing agent only activated on the surface of metal particles, therefore, deposition of secondary metal is targeted onto the base catalyst particles or itself. By controlling the base catalyst, secondary metal ion source, reducing agent, bath temperature, and pH, multiple bimetallic catalyst systems, such as Cu−Pd [86], Ag−Pt [87], Pt−Co [88], Au−Pd [84], and Ag−Pd [89] were successfully synthesized.

In this work, we studied the catalytic conversion of furfural to cyclopentanone in water over Pd-Co and Pd-Cu bimetallic catalysts with due attention paid to achieving high metal dispersion and intimate metal1-metal2 contact. Activity and selectivity are compared for silica supported Pd-Cu and Pd-Cu catalysts prepared by conventional dry impregnation (DI), simultaneous Strong Electrostatic Adsorption (co-SEA) and SEA followed by Electroless Deposition (SEA-ED). And rational sysnthesis effect on catalysts resistence against particles sintering and dealloying are also examined by XRD.

5.2 Results and discussion

5.2.1 Monometallic and bimetallic catalysts synthesis by SEA and co-SEA

The single metal uptake curves are shown in Figure 5.1. The silica slurry density was 1000 m^2/l, and the Pd, Cu, and Co concentrations were 120, 100, and 100 ppm

respectively. The surface density of Pd, Cu and Co cations adsorbed on SiO_2 to a maximum surface density around 1.2 μmol/m^2. The Pd curve presented the typical volcano-shape of SEA, with increasing uptake as the pH increases from the PZC (3.3 for silica), whereas uptake is retarded in extreme basic condition from the strong ionic strength [94]. The uptake of Co at high pH stays high due to formation of Co phyllosilicate [72]. The pH window of Cu ammine solubility is very narrow, permitting only a few points to be tested. The optimal pH to prepare monometallic Pd, Cu and Co catalysts are about 11, though a lower pH would be preferred for Co to prevent the formation of the phyllosilicate.

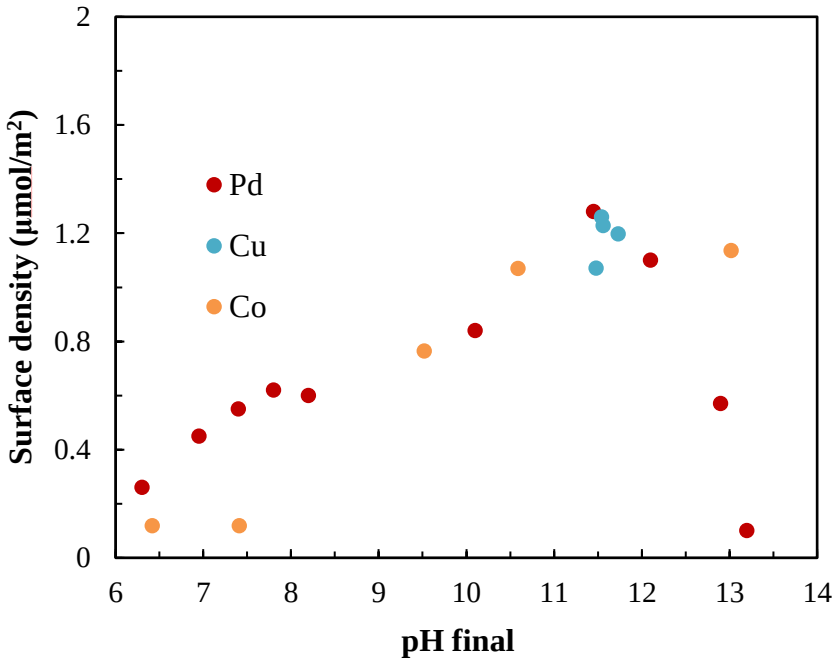

Figure 5.1. Adsorption surveys of cationic Pd, Cu and Co over silica.

Data for the simultaneous adsorption of metals is shown in Figure 5.2. In these experiments the silica slurry thickness was again 1000 m^2/l and the Pd, Co and Cu concentrations were 100, 40, and 40 ppm. The lowered Co and Cu ammine concentrations were employed in view of the ultimate aim of preparing Pd/Co and Pd/Cu atomic ratios

near 1:1. In co-SEA of Pd-Cu and Pd-Co, the total metal uptake topped at 1.2 μmol/m^2 which was consistent with that in single metal uptake. The maximum surface density of these metal precursors is around 1.2 umol/m^2 caused by steric hindrance in the method of SEA. This maximum surface density of 1.2 umol/m^2 corresponds with the retention of two hydration sheaths during adsorption, commonly observed in SEA. The metal adsorption density cannot be further increased with beyond this, even with the increase in metal concentration of the mother solution. In Fig. 5.2, we clearly observe the combined uptake of both metals totals to 1.2 umol/m^2. For cases where one metal adsorbs more strongly (Fig. 5.2a, Cobalt), we have a limited and fixed amount of cobalt at 0.5 umol/m^2 (24 ppm Co) to promote palladium adsorption. A narrower volcano-shaped curve also appears in the Pd-Cu experiment despite the narrow pH range of the survey. The horizontal line in Pd-Co uptake (Figure 5.2a) indicated a complete adsorption of Co ions over the entire pH range. That uptake of Co is as high as Pd, even though the Co concentration is lower, is explained by the higher valence of Co^{3+} versus Pd^{2+} [117]. Ultimately, two bimetallic Pd-Co and Pd-Cu catalysts were synthesized around pH 11.5 using 42 ppm Pd with 18 ppm Cu and 45 pm Pd with 24 ppm Co; these gave 1.2%Pd-0.5%Cu and 1.3%Pd-0.7%Co, corresponding to Pd and M2 (M2= Cu, Co) molar ratio of 1.4 and 1.0 respectively.

Two bimetallic catalysts with the same loadings were prepared by incipient wetness using the same precursors.

5.2.2 Bimetallic Pd-Cu catalysts synthesized by ED

To compare bimetallic core-shell particles to those prepared by co-SEA and co-DI, one additional series of Cu catalysts was prepared by applying Cu as partial shells to Pd cores, which are the highly dispersed Pd monometallic samples described above. The

development of ED bathes for Cu^{+} deposition have been described before [134] , where electroless deposition baths were prepared using Cu(CN) as the source of Cu^{+}, hydrazine as the reducing agent in pH 9.5 solution.

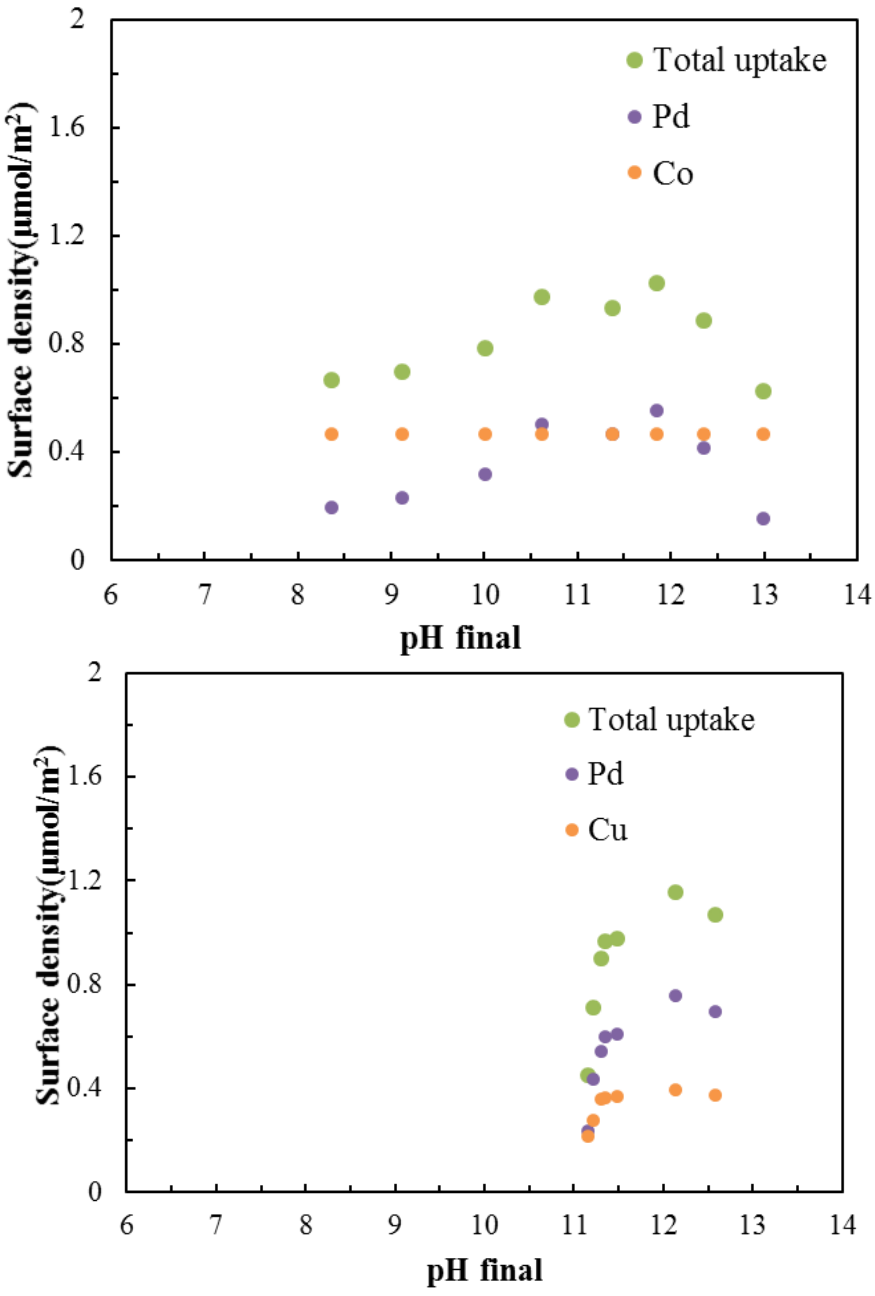

Figure 5.2. Simultaneous metal uptake of a) PdCo and b).PdCu on SiO_2.

One hundred mL of 20 ppm and 10 ppm Cu^+ were prepared, and after 0.4 grams of 1.3% Pd/SiO_2 was added into the ED solution, N_2H_4 was pumped into the ED bath continuously for 1 hour, with the molar ratio of reducing agent to Cu^+ of 4.1 and 8.2 at the end of the process. The depletion of Cu from the ED bath as a function of time is shown in Figure 5.3. Two Cu-Pd bimetallic catalysts were synthesized as such, corresponding to 0.4%Cu-1.3%Pd and 0.2%Cu-1.3Pd, with theoretical coverage of 0.9 and 0.5 monolayer of Cu on Pd. The actual Cu coverage determined by pulse hydrogen chemisorption closely agreed with these values, implying that the Cu deposition proceeded in catalytic pathway and Cu deposited selectively on Pd surface instead of itself or on SiO_2.

A total of five monometallic catalysts including Cu-only, Co-only, and Pd catalysts at three weight loadings and six bimetallic catalysts were synthesized for evaluation in furfural rearrangement. A summary of these catalysts and their characterization by XRD are summarized in Table 5.1.

5.2.3 Characterization by XRD, STEM and TPR

Fig.5.4a shows the XRD patterns of Cu, Co and Pd catalysts supported on SiO_2 from top to bottom. The broad feature at 22° stems from amorphous SiO_2. No Pd or Co peaks were observed in the XRD patterns, implying that Pd particles and Co particles are below the detection limit of the instrument, which is about 1.5 nm [3, 125][20]. On the other hand, in the sample of 2.3% Cu/SiO_2 (blue pattern), CuOx peaks (36° and 47°) became discernable. After support subtraction from the original pattern followed by the procedure in our previous work [78], CuOx peaks were clearly discernable (Figure 5.4b), and sized at 2.0 nm based on Scherer equation. It is well-known that small Cu particles tend to be oxidized at ambient conditions.

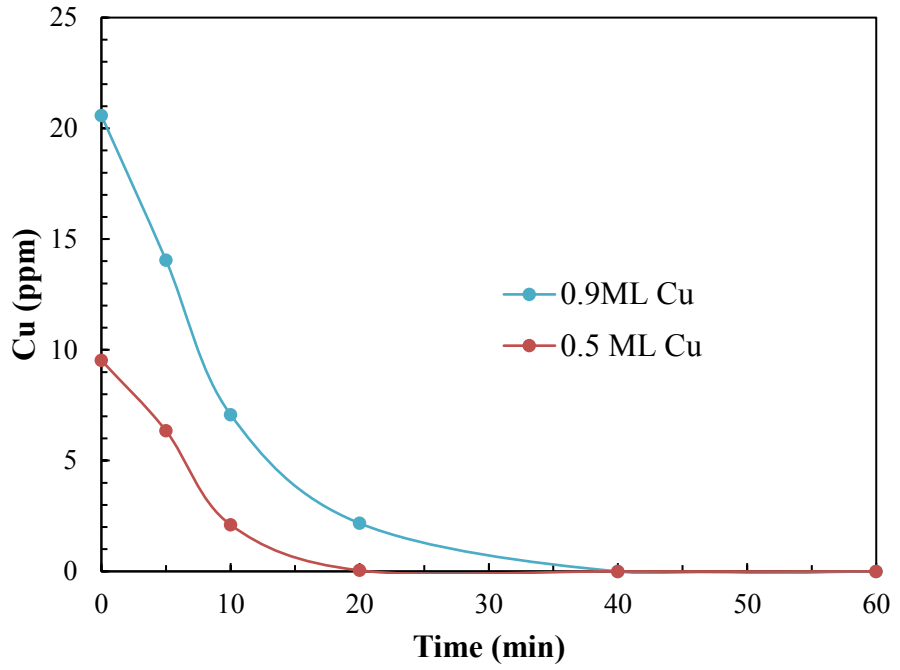

Figure 5.3. Cu deposition on 1.3%Pd/SiO_2 by electroless deposition.

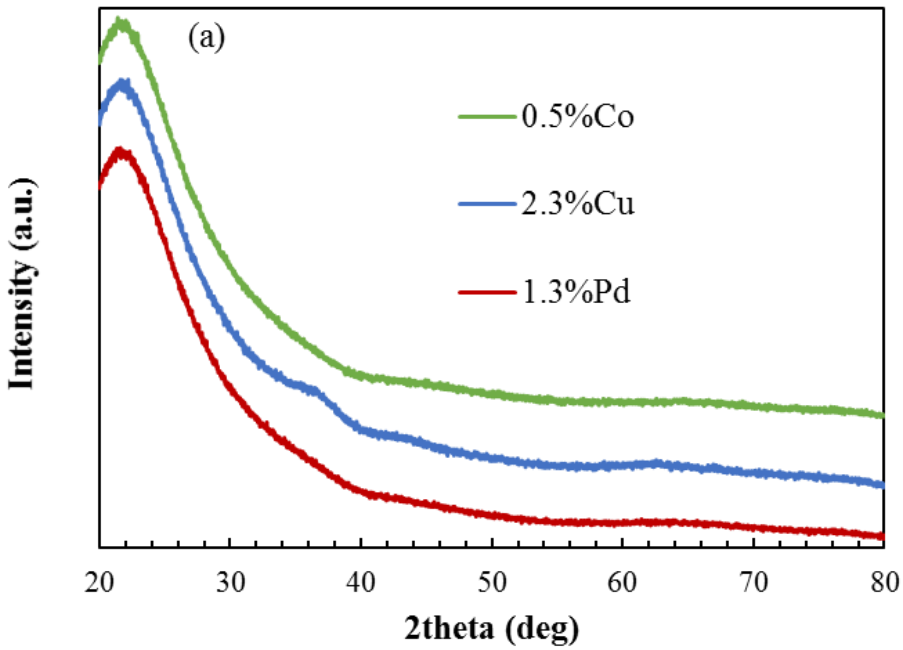

Figure 5.4 XRD profiles of a) SiO_2 supported monometallic Cu, Co and Pd.

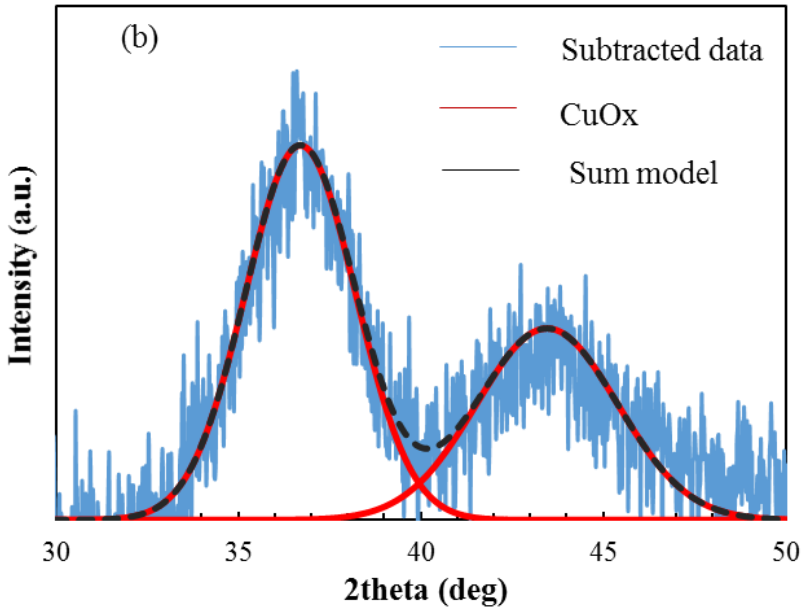

Figure 5.4.b) XRD deconvolution of CuOx from support and background.

XRD analysis of the bimetallic Pd-Co and Pd-Cu catalysts is given in Figure 5.5. Diffraction peaks were not observed for SEA- and ED-derived bimetallic Pd-Cu and Pd-Co catalysts, indicating bimetallic particles were less than 1.5 nm. Before Cu deposition, Pd size was smaller than 1.5 nm (Figure 5.4a), and bimetallic Cu-Pd remain small as the Cu coverage was less than 1 monolayer. Pd peaks appeared only in the two DI-prepared counterparts. In the 1.3%Pd-0.7%Co DI catalyst, metallic 8.1 nm Pd and 8.5 nm Co werge seen, and Pd and Co is believed to exist largely as separate clusters since the Pd and Co diffraction peaks appear unshifted from the pure metals. On the other hand, in the 1.2%Pd-0.5%Cu DI catalyst, four peaks are deconvoluted in the region between Pd(111) and Cu(111), and correspond to pure Pd, a Pd rich and a Cu rich Pd-Cu alloy and pure Cu, all metallic. (A diffractometer with a latest-generation, high sensitivity solid state detector makes the observation of sub-2 nm nanoparticles and such deconvolutions possible [3, 78].)

Peaks and peak breadths at 40.2°, 41.2°,42.4° and 43.0° were indexed as metallic Pd (8.6 nm), Pd-rich Pd-Cu alloy (12.9 nm), Cu-rich Pd-Cu alloy (6.7 nm) and metallic Cu (20.2 nm) respectively. There was no sign of CuOx in the DI catalyst which can be explained by the resistance to oxidation of larger particles. The weak interaction between metal precursors and support with the DI preparation account for the larger particles in the two DI catalysts. All metal particle sizes are summarized in Table 5.1.

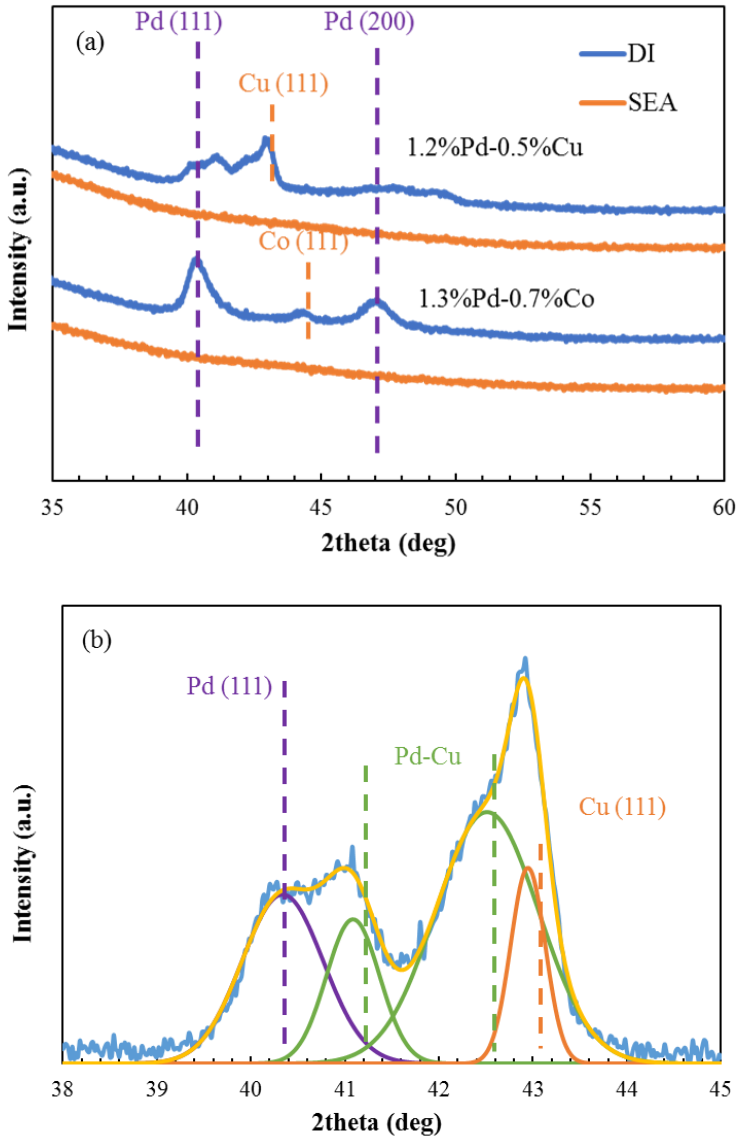

Figure 5.5.a) XRD patterns of bimetallic catalysts prepared by DI, SEA and ED XRD and b) deconvolution of Pd, Cu and PdCu alloy in DI prepared bimetallic catalyst.

Table 5.1. Catalysts synthesis and size determination.

#	Catalyst	Precursor	Prep. method	Part. size (nm)
1	0.7%Pd	$[Pd(NH_3)_4]^{2+}$	SEA	<1.5
2	1.3%Pd	$[Pd(NH_3)_4]^{2+}$	SEA	<1.5
3	3.3%Pd	$[Pd(NH_3)_4]^{2+}$	SEA	<1.5
4	2.3%Cu	$[Cu(NH_3)_4]^{2+}$	SEA	2.0 (CuO_x)
5	0.8%Co	$[Co(NH_3)_6]^{3+}$	SEA	<1.5
6	1.2%Pd-0.5%Cu	$[Pd(NH_3)_4]^{2+}$ $[Cu(NH_3)_4]^{2+}$	co-SEA	<1.5
7	1.2%Pd-0.5%Cu	$[Pd(NH_3)_4]^{2+}$ $[Cu(NH_3)_4]^{2+}$	DI	8.6 (Pd)
				12.9 (Pd rich-Cu)
				6.8 (Pd-Cu rich)
				20.2 (Cu)
8	[b]0.4%Cu-1.3%Pd	$[Pd(NH_3)_4]^{2+}$ $[Cu(CN)_2]^-$	SEA-ED	<1.5
9	[c]0.2%Cu-1.3%Pd	$[Pd(NH_3)_4]^{2+}$ $[Cu(CN)_2]^-$	SEA-ED	<1.5
10	1.3%Pd-0.7%Co	$[Pd(NH_3)_4]^{2+}$ $[Co(NH_3)_6]^{3+}$	co-SEA	<1.5
11	1.3%Pd-0.7%Co	$[Pd(NH_3)_4]^{2+}$ $[Co(NH_3)_6]^{3+}$	DI	8.1 (Pd) 8.5 (Co)

Figure 5.6 displays representative STEM images for 2.1%Pd-1.0%Cu and 1.3%Pd-0.7%Co by co-SEA and their corresponding particle size distributions. Homogeneously distributed metal particles with tight size distribution were seen in both catalysts. No agglomerates or large particles were seen in any image. The average size of each was 1.1 ± 0.2 nm by counting 500 particles. The small sizes are consistent with the particles being below the limit of XRD detection. The composition of seven individual nanoparticles was measured for each sample by spot x-ray analysis. For Pd/Co, all seven showed the simultaneous presence of Pd and Co, with an average atomic ratio of 0.6:1, lower than the nominal 1:1 ratio, while seven Pd-Cu nanoparticles all showed the simultaneous presence of Pd and Cu and averaged an atomic ratio of 1:1, again lower than the 1.4:1 nominal

loading, but higher than the Pd-Co ratio as expected. The limited number of particles for analysis could well be the source of absolute discrepancy in ratios.

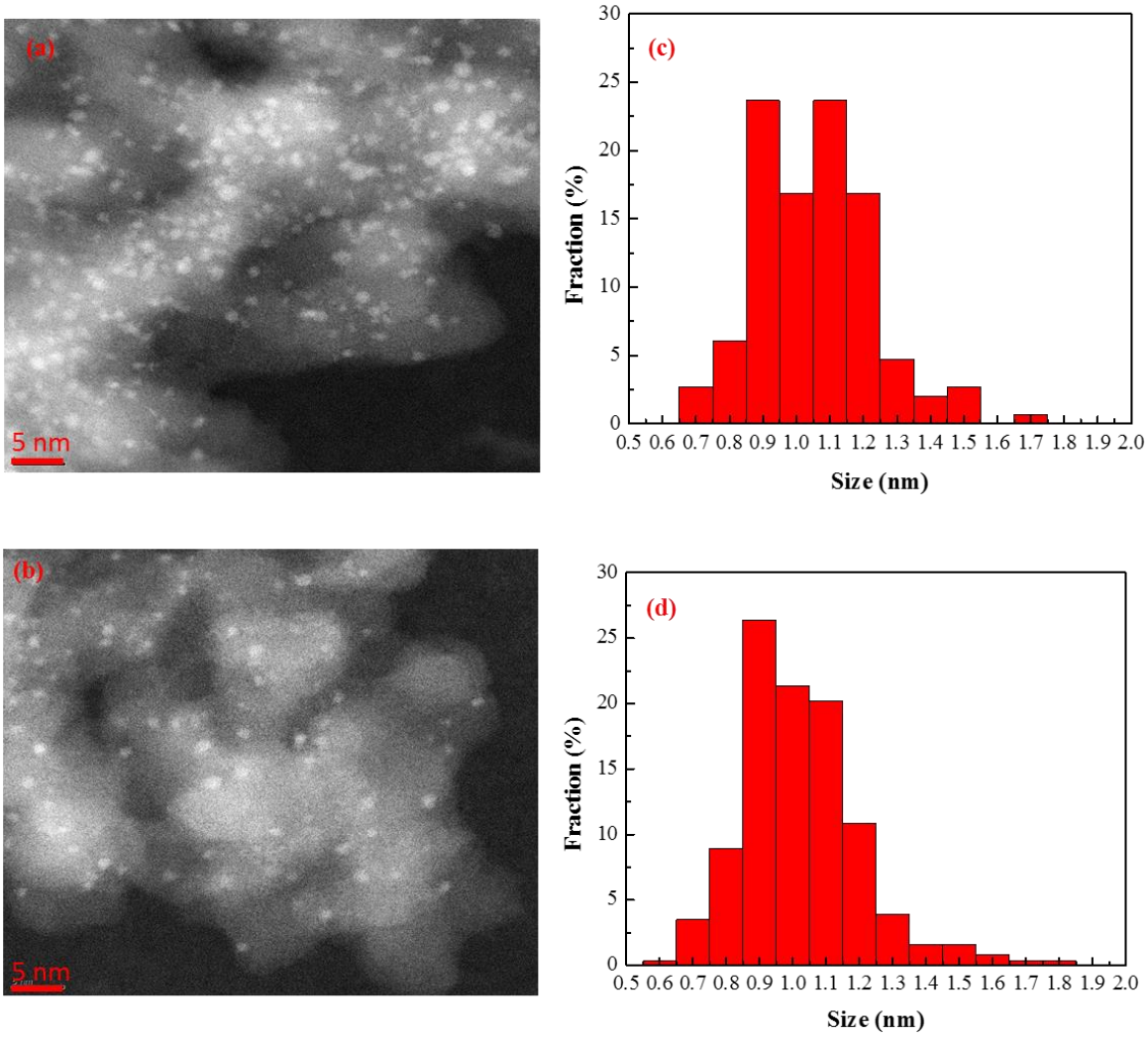

Figure 5.6.a) STEM micrographs and c) particle size distributions of SEA-prepared SiO_2-supported 2.1%Pd-1.0%Cu bimetallic sample.b) STEM micrographs and d) particle size distributions of SEA-prepared SiO_2-supported 1.3%Pd-0.7%Co bimetallic sample.

TPR results demonstrated a dramatic difference in reducibility of SEA- versus DI-prepared Pd-Co catalysts. In Figure 5.7, the high temperature reduced Co species (700°C) shifted towards low temperature reduced Pd (200°C) in the co-SEA catalyst and initiated

around 350°C. The intimacy between the two metals explains the substantial decrease in reduction temperature, due to hydrogen spillover from closely interacting Pd sites. The TPR profile of the DI sample can be explained by poorer interaction of Pd and Co. In this case, the larger Pd particles were believed to be reduced at much lower temperature than the SEA counterpart, and peaks around 290°C and 350°C were assigned as reduction of Co_3O_4, which has been reported in literature [135], corresponding to Co^{3+} to Co^{2+} and Co^{2+} to Co0 respectively. The reducibility of Pd-Cu bimetallic catalysts almost remained unchanged (not shown) due to the similar reductive properties of Pd and Cu ammine precursors; both are around 200°C.

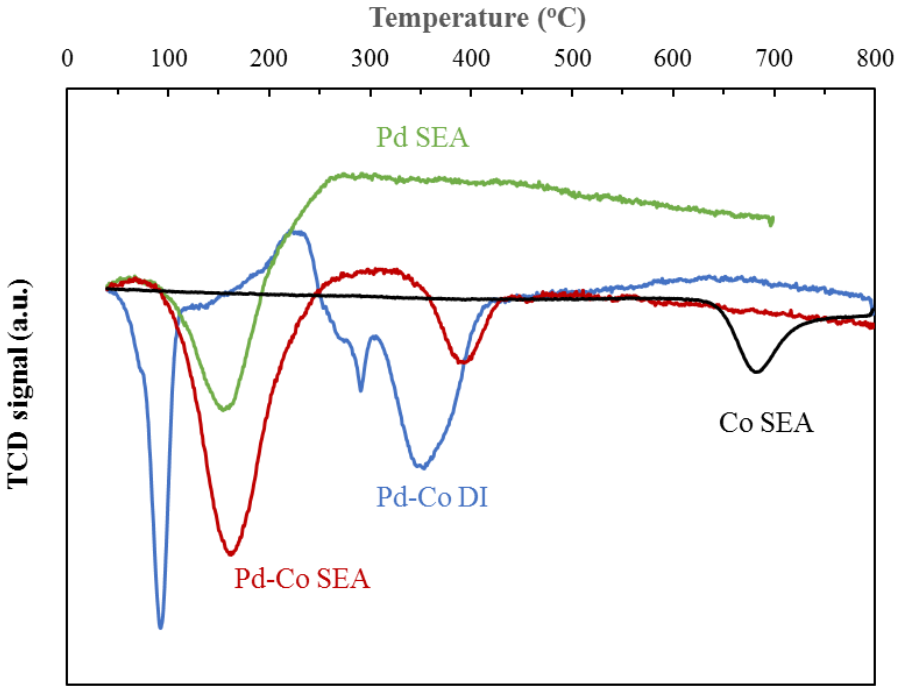

Figure 5.7. Reducibility change in bimetallic catalysts from H_2-TPR profiles.

5.2.4 Catalytic evaluation in furfural conversion

The bimetallic effect on activity/selectivity and preparation methods effect on the product distribution were investigated. A summary of the eleven catalysts‘ reactivity in furfural hydrogenation is listed in Table 5.1. Selectivity is reported at various levels of furfural conversion. The possible pathways reported in literature are shown in Scheme 5.1 [43-44, 136].

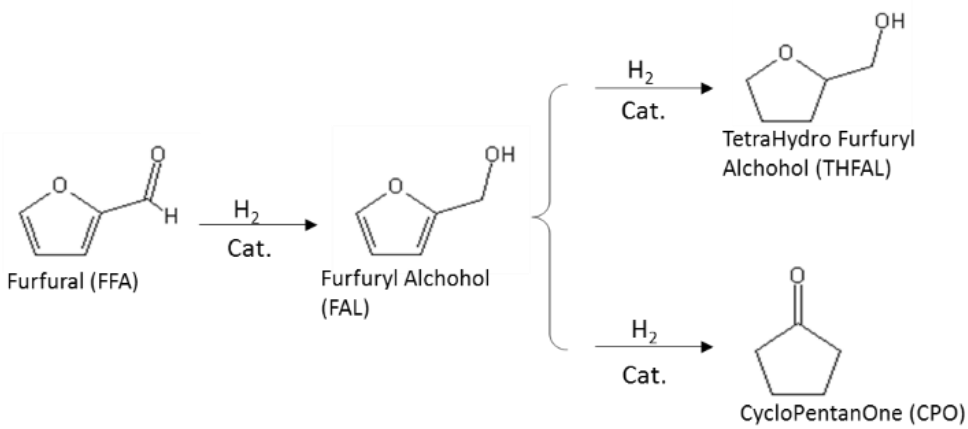

Scheme 5.1. Proposed pathway of furfural conversion in literature.

After the 3-hour run at 150^{o}C with 430 Psig hydrogen partial pressure, products detected included furfuryl alcohol (FAL), tetrahydrofurfuryl alcohol (THFAL), cyclopentanone (CPO), cyclopentanol (CPL), furan (FRN) and levulinic acid (LA). However the last three chemicals were observed in only trace amounts, as shown in the gas chromatogram of Figure A1. Thus the only appreciable reaction products are those appearing in Scheme 1. The results of furfural hydrogenation on monometallic Co, Cu and Pd catalysts is shown in Figure 5.8a. The amount of catalyst used varied in the range 0.115~0.297 grams to maintain the same number of moles (0.042 mmoles) of metals. Among these three catalysts, Co was inactive in these reaction conditions (water solvent),

likely because Co remained oxidized. Pd showed the highest conversion and selectivity to FAL (70%). However, the selectivity of CPO was only 28% over 1.3%Pd/SiO_2. CPO was observed as only product on Cu catalyst which converted 17% of FFA in 3 hours. The intrinsic catalytic acvitivy as denoted by the chemisorption-derived turnover frequency (TOF) was 10 times higher for the Pd monometallic catalyst than the Cu catalyst (0.188 s^{-1} vs 0.016 s^{-1}) as displayed in Table 5.2.

Figure 5.8b shows the results of the series of SEA-prepared Pd monometallic catalyst in which a constant amount of catalyst (266 mg) was used. (These catalysts were also used for the Madon-Boudart test as described in the experimental section below.) Conversion increased in proportion to metal loading from 16% to 90% and the trend in FAL production, rising and then falling, supports the consecutive reaction pathway proposed in the literature [43-44, 136], with the first step of hydrogenation of FFA to FAL and the second step of parallel pathways of further hydrogenation of FAL to THFAL or FAL ring rearrangement to a key intermediate to CPO. It has been reported that Pd catalysts favorhydrogenation of aldehyde and its furfural hydrogenation to THFAL in aqueous phase FFA conversion [36, 40]. The current results, however, show little accumulation of THFAL, and much higher selectivity toward CPO. This may be a consequence of Pd particle size. Detailed product distributions for these runs are plotted in Figures A2-A4.

The monometallic 2.3% Cu catalyst (Figure 5.8a) gave only 17% conversion and the 100% selectivity to CPO compared to the same number of moles of Pd. The absence of the FAL intermediate over Cu can be explained by Cu sites having high facility for the ring rearrangement step, but poor activity for the hydrogenation step; as soon as the FAL

forms in a slow step it rearranges. In a previous report [137], the rearrangement of FAL occured in water without presence of catalyst; and in Zhang's work [138], the ring arrangement of FAL was catalyzed by weak acidity of media: the yield of 4-hydroxycyclopent-2-enone (product of ring arrangement of FAL, intermediate to CPO) was 53.5% at 240°C in water with no catalysts. This may first be due to the lower reaction temperature, and second, to the acidic pH of the reaction medium which was determined to be in a range of 3.0 to 3.5 for both monometallic and bimetallic catalysts (see Table A1). In this narrow range and in the presence of catalyts, the selectivity to CPO was dramatically different on monometallic Pd and Cu catalysts (28% v.s. 100%) and the variance in CPO production was also observed on bimetallic catalysts wich will be presented later. Thus the effect of the liquid phase on selectivity is believed to be insignificant in this work.

From there monometallic results, it may be envisioned that a combination of Pd and Cu would operate synergistically whereby the high hydrogenation activity of the Pd could be coupled with the high ring arrangement activity of the Cu. The optimized catalyst would give high furfural conversion with high CPO selectivity, with greatly reduced amounts of Pd. To this end, the middle loading of 1.3% Pd was chosen as a basis, and Pd-Cu catalysts were prepared by different methods, while maintaining Pd: Cu in the range of 1.1 ~1.4. Pd-Co was also synthesized to study whether Pd can also be promoted by Co , per literature reports [44, 139].

Pd-Cu and Pd-Co bimetallic catalysts were evaluated under same conditions as monometallic catalysts. Reaction rates werecompared at 10% FFA conversion and selectivity is reported as various times. The number of moles of Pd (0.042 mmoles) was maintained constant by varying the mass of catalyst in the reaction. Pd-Cu bimetallic

catalysts were prepared by co-SEA, SEA-ED and co-DI, and the Pd-Co catalysts by co-SEA and co-DI.

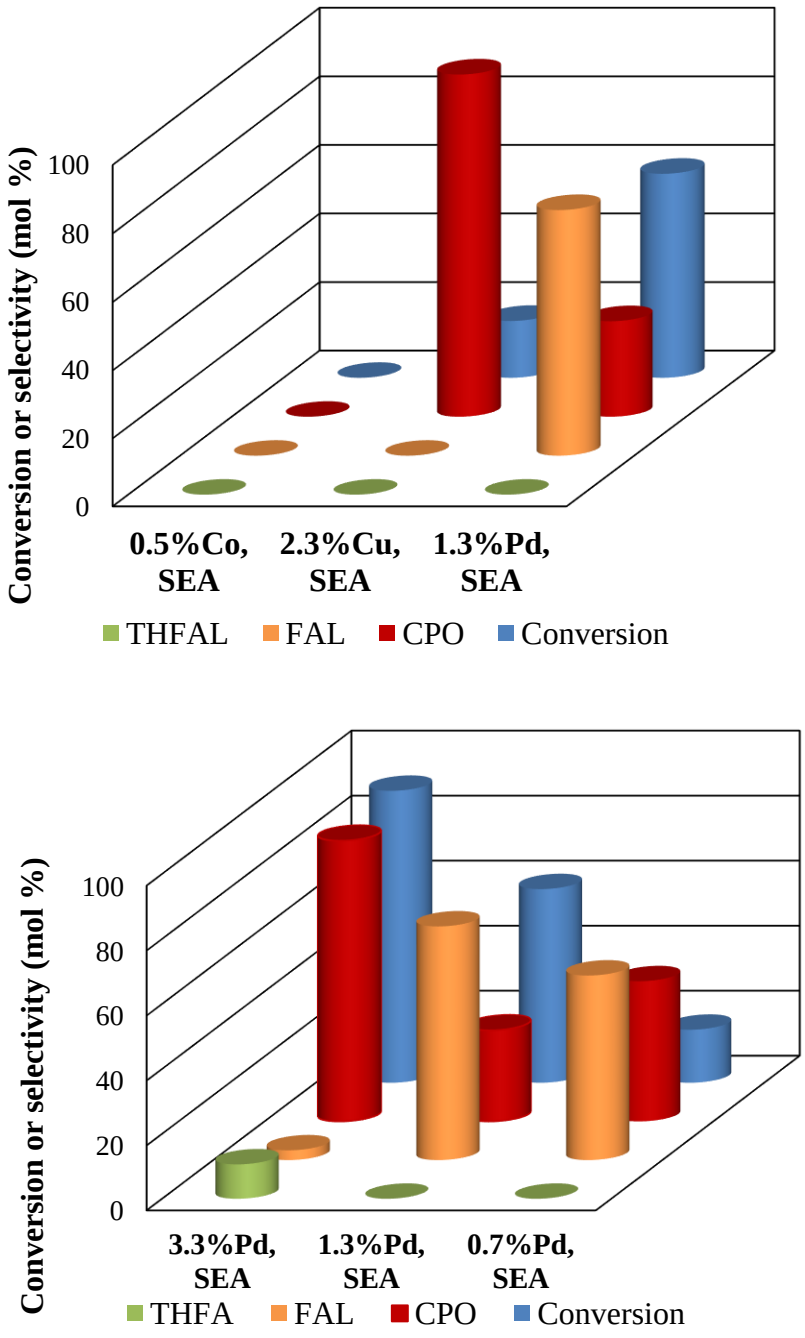

Figure 5.8.a) Catalytic evaluation over Pd, Co, Cu monometallic catalysts; b) Catalytic evaluation over three loadings of Pd monometallic catalyst. Reaction conditions: 3 grams FFA in 57 grams H_2O at 150°C with total pressure of 500 psig; agitation speed, 1000 rpm; reaction time, 3 hours.

In Witonska's study, the addition of copper only slightly influenced the activity of Pd/Al_2O_3, while it significantly modified its selectivity to [36]. As summarized in Table 5.2, at low conversion there was no difference in product distribution between Pd monometallic and PdCu bimetallic catalyst; as reaction continued, the production of CPO was markedly increased on the bimetallic catalyst (Figure 5.9): the selectivity to CPO tripled to the same level as observed on the $3.3\%Pd/SiO_2$ (Figure 5.8b) which can be attributed to the close interaction of Cu sites with Pd sites to promote rearrangement to CPO. TOF increased nearly 3 folds on 1.2%Pd-0.5%Cu co-SEA (0.471 s^{-1}, Table 5.2) catalyst compared to monometallic 1.3%Pd SEA (0.188 s^{-1}, Table 5.2) which also can be explained by PdCu bimetallic formation rendered by rational syntheis of co-SEA. Since the bimetallic particles remained small (1.1 nm per STEM, Figure 5.6), none of the Pd activity was lost (Figure 5.9); that is, the Cu alloying did not dilute the number of Pd sites at the catalytic surface. The parallel hydrogenation product THFAL was only detected in small quantities at the very end of reaction. The reactivity of three catalysts of approximately the same nominal composition, but prepared by different methods, is compared in Figure 5.10. Two catalysts, the co-SEA and co-DI, had compostions of 1.2% Pd and 0.5% Cu, while the SEA-ED catalyst had 1.3%Pd and 0.4% Cu. From the XRD and STEM characterization above, the co-SEA sample is believed to be homogeneously alloyed nanoparticles, highly dispersed, the DI is a mixture of poorly dispersed particles of pure Pd, pure Cu, a Pd rich alloy, and a Cu rich alloy. From chemisorption results described above, the SEA-ED sample is thought to be almost a full mmonolayer of Cu over highly dispersed Pd cores. These morphologies are sketched into the bar chart for the sake of convenience.

The preparation method has a profound effect on reactivity (Figure 5.10). The activity and selectivity of the SEA-ED sample are similar to the pure Cu sample in Figure 5.9, even though the amount of Cu is several times lower. It would appear that the Pd cores serve as support for highly dispersed Cu, present as a nearly full monolayer, and so its activity becomes similar to the lower dispersion, pure Cu sample. The DI sample gives even lower activity, and the high selectivity to CPO indicates that the ratio of Cu surface to Pd surface is high.

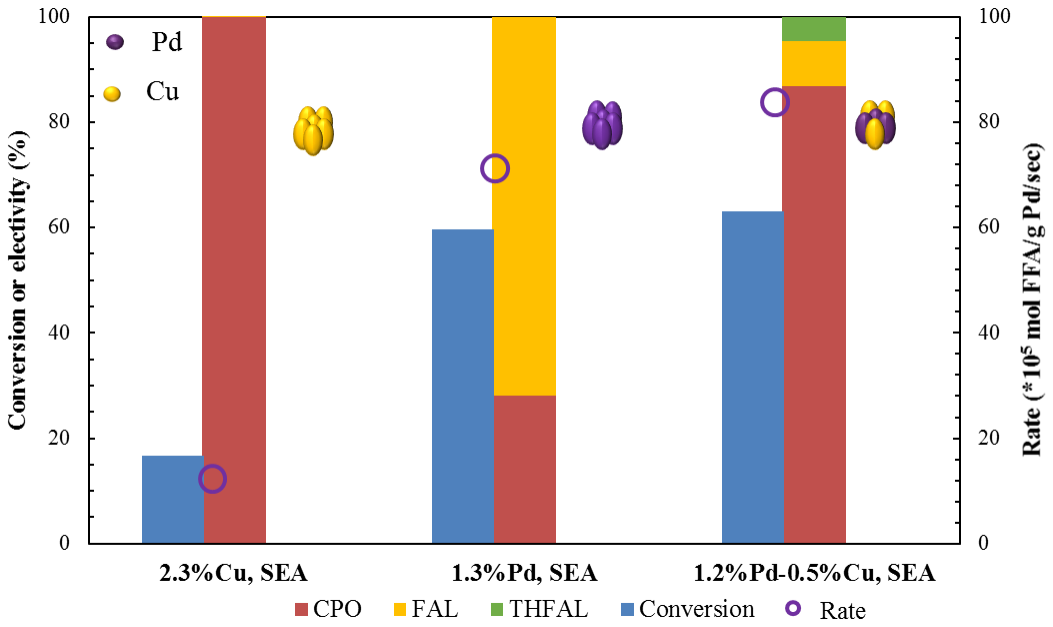

Figure 5.9. Pd-Cu alloying effect. Reaction conditions: 3 grams FFA in 57 grams H_2O at 150°C with total pressure of 500 psig; agitation speed, 1000 rpm; reaction time, 3 hours; catalyst ranged from 0.11 g to 0.27 g to keep metal/FFA molar ratio constant between monometallic catalysts, and Pd/FFA molar ratio constant between Pd monometallic and bimetallic catalysts.

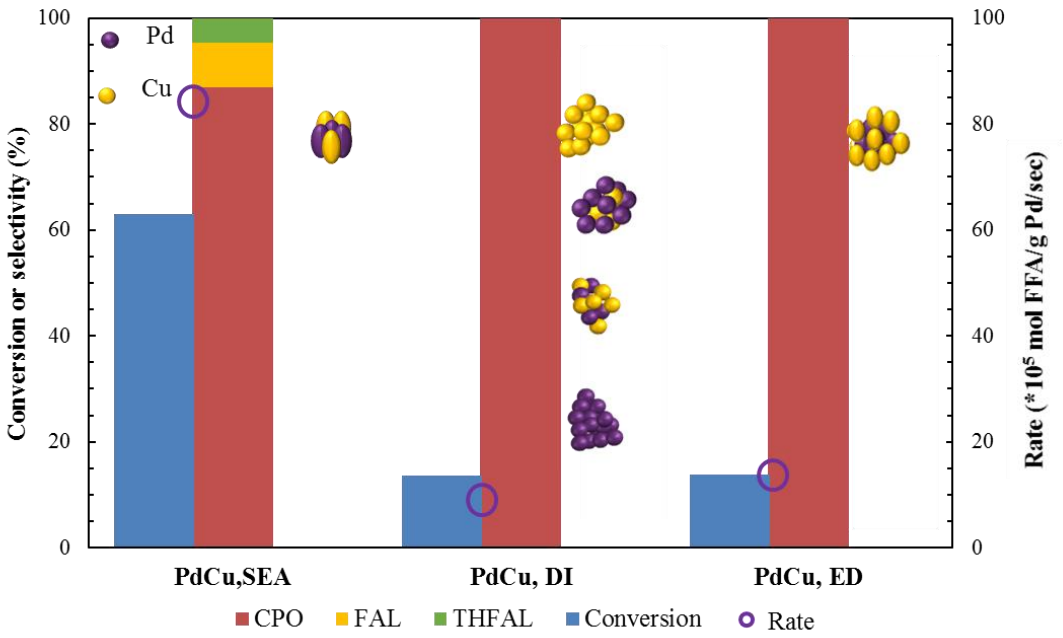

Figure 5.10. Preparation method effect. Reaction conditions: 3 grams FFA in 57 grams H_2O at 150°C with total pressure of 500 psig; agitation speed, 1000 rpm; reaction time, 3 hours; Constant catalyst/FFA ratio.

A final series of SEA-ED Pd catalysts with various Cu coverage were tested to relate θ_{Cu} and catalytic performance. Figure 5.11 shows that activity decreased with increasing Cu coverage; at 0.9 θ_{Cu} the activity and selectivity were, as mentioned above, virtually equivalent to the monometallic Cu catalyst. The interesting feature in this set of experiments is the intermediate Cu coverage catalyst (θ_{Cu} = 0.5, 1.3%Pd, 0.2%Cu), which is the only catalyst formulation in this study which gives significant amounts of THFAL product (43% to 57% CPO) with no FAL observed. The moderate amount of Cu on the Pd surface would appear to generate bimetallic surface sites very reactive toward FFA, while mitigating the ring rearrangement ability of the Cu surface while opening the secondary hydrogenation pathway. The only other catalyst showing observable amounts of TFHAL where the co-SEA catalysts at long reaction time; the same type of bimetallic site may have

been operative in those nanoparticles. Yuan et al. [140] observed THFAL to be the main product via bimetallic synergy from small portions of Pd with supported Ni. High pressure also appears to increase THFAL yield; in Biradar's work, at 725 psig over a 3%Pd/C catalyst, the THFAL yield was more than 40% [38]. The turnover frequencies of 0.4%Cu-1.3%Pd SEA-ED and 0.2%Cu-1.3%Pd SEA-ED were slightly higher than that of 1.3%Pd SEA, 0.263 $s^{-1}$and 0.215 s^{-1} respectively, however, only half of 1.3%Pd-0.5%Cu co-SEA, which, again, indicates that bimetallic formation plays crucial role here. Meanwhile, the amount of PdCu alloy is limited in the catalysts synthesized by SEA-ED method which is consistent with H_2-chemisorption results that Pd surface is covered by Cu particles. Even with almost full monolayer of Cu coverage, the TOF on 0.4%Cu-1.3%Pd SEA-ED was enhanced by the small amount of PdCu alloy compared to 2.3%Cu SEA (0.016 s^{-1}).

The reactivity of the Pd-Co catalysts is shown in Figure 5.12. The introduction of cobalt failed to improve the overall catalytic activity on PdCo catalyst, even with high dispersion bimetallic particles in co-SEA prepared catalyst. As displayed in Figure 5.12, FFA conversion dropped 60% on the monometallic Pd catalyst to 38.5% and 2.5% on 1.3%Pd-0.7%Co co-SEA and 1.3%Pd-0.7%Co DI respectively. The CPO selectivity was enhanced by Co existence as observed in PdCu bimetallic catalyst. PdCo alloy in 1.3%Pd-0.7%Co co-SEA facilitated the reaction at the early stage, the TOF was at the same level as 1.3%Pd-0.5%Cu co-SEA. The lower conversion on 1.3%Pd-0.7%Co co-SEA than 1.3%Pd-0.5%Cu co-SEA results from the great dealloying in the catalyst which will be presented and discussed in Post-reaction characterization. The higher activity of the PdCo co-SEA than the DI catalyst can be attributed to the well dispersed bimetallic particles shown in XRD and STEM.

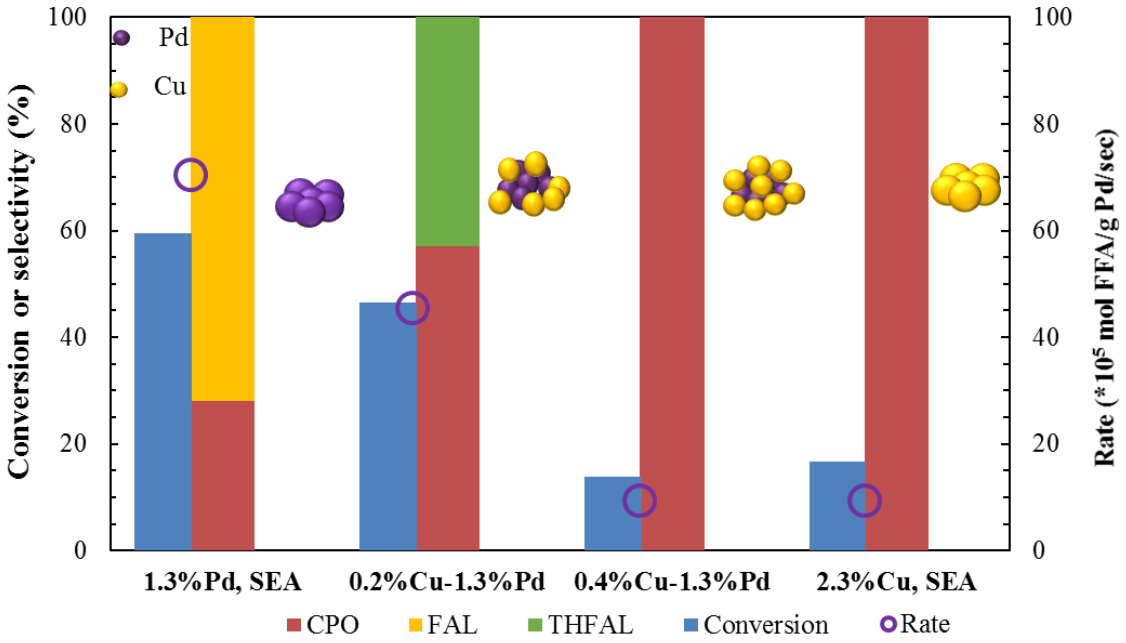

Figure 5.11. Copper coverage effect. Reaction conditions: 3 grams FFA in 57 grams H_2O at 150°C with total pressure of 500 psig; agitation speed, 1000 rpm; reaction time, 3 hours; Constant Pd/FFA ratio.

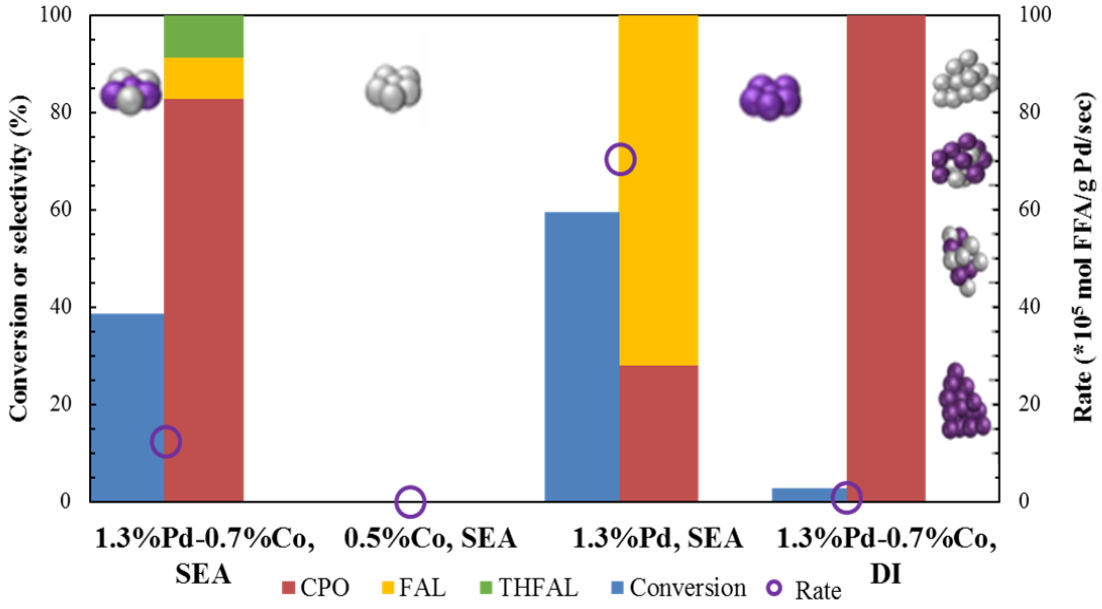

Figure 5.12. Pd-Co bimetallic effect on FFA conversion to CPA. Reaction conditions: 3 grams FFA in 57 grams H_2O at 150°C with total pressure of 500 Psig; agitation speed, 1000 rpm; reaction time, 3 hours; catalyst ranged from 0.15 g to 0.26 g to keep metal/FFA molar ratio constant between monometallic catalysts, and Pd/FFA molar ratio constant between Pd monometallic and bimetallic catalyst.

5.2.5 Post-reaction Characterization

XRD characterization of used catalysts is shown in Figure 5.13. Diffraction peaks were observed after 3-hour reaction for all monometallic and bimetallic catalysts. The monometallic Pd catalyst sintered to 4.8 nm after use (center pattern). The two SEA-ED samples are the top two patterns in the figure; the 0.5 ML Cu sample (0.2%Cu-1.3%Pd) sintered to 4.9 nm with a (111) peak position shifted toward Cu which indicates some degree of alloying as the Pd core sintered. While the half monolayer of Cu on Pd did not enhance the ability against sintering during reaction, the 0.9 ML shell (0.4%Cu-1.3%Pd) did, as the nanoparticles sintered only to 3.5 nm. This pattern appears to be a combination of a Pd rich and a Cu rich phase, suggesting that while some alloying had occurred, the particles may still be in a Pd-rich core, Cu-rich shell morphology which is a reflection of the initial morphology.

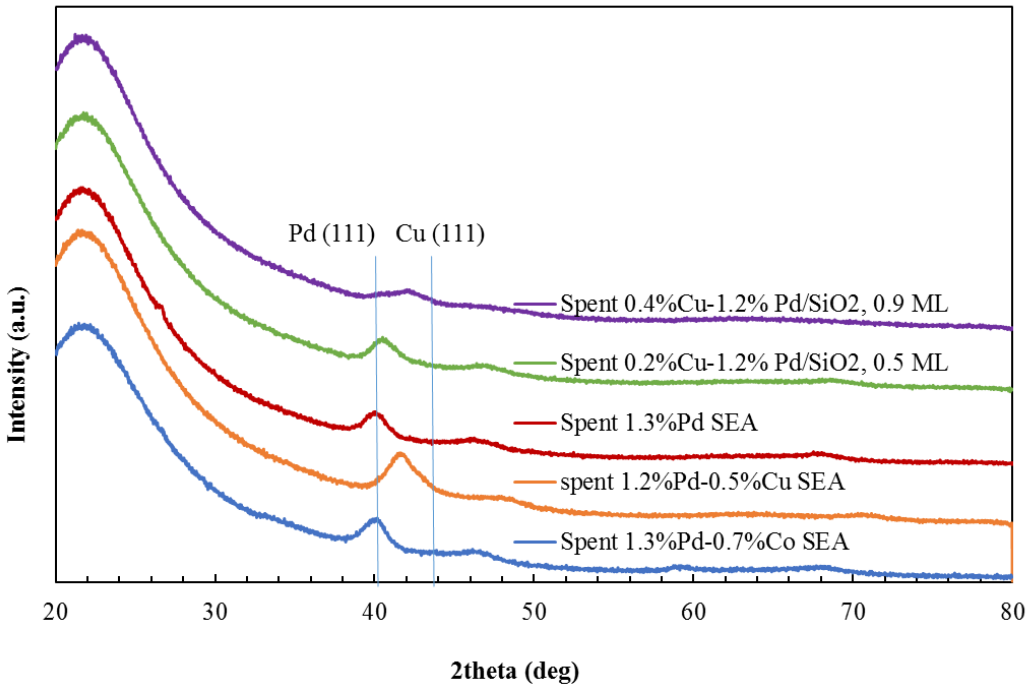

Figure 5.13. XRD analysis of spent Pd bimetallic catalysts prepared by SEA and ED.

Table 5.2. Summary of catalytic performance over mono- and bi-metallic catalysts.

Cat.	Conv.: 15±5%			Conv.: 40±5%			Conv.: 60±5%			Rate [*10^5 mol FFA/(g Pd*s)]	TOF (s^{-1})
	CPO	FAL	THF-AL	CPO	FAL	THF-AL	CPO	FAL	THF-AL		
0.8% Co, SEA	-	-	-	-	-	-	-	-	-	0	-
2.3%Cu, SEA	100	0	0	-	-	-	-	-	-	9.0	0.016
1.3% Pd, SEA	0	100	0	15.1	84.9	0	28.1	71.9	0	71.0	0.188
1.2%Pd-0.5%Cu, co-SEA	4.7	93.7	0	15.3	84.8	0	86.9	8.5	4.6	84.4	0.471
1.2%Pd-0.5%Cu DI	100	0	0	-	-	-	-	-	-	4.6	-
0.4%Cu-1.3%Pd, SEA-ED	100	0	0	-	-	-	-	-	-	9.5	0.215
0.2%Cu-1.3%Pd, SEA-ED	14.9	85.1	0	57.0	0	42.9	-	-	-	45.4	0.263
1.3%Pd-0.7%Co, co-SEA	22.2	77.8	0	69.9	22.2	7.9		-	-	10.5	0.518
1.3%Pd-0.7%Co, DI	100	0	0	-	-	-	-	-	-	0.23	-

The co-SEA Pd-Cu and Pd-Co samples, the lower two patterns of Figure 5.13, also showed increased resistance to sintering compared to pure Pd, with average sizes of 2.5 and 3.6 nm, respectively. The largest degree of alloying ((111) peak shift) of all bimetallic catalysts is seen for the co-SEA prepared PdCu catalyst. A careful deconvolution of the co-SEA Pd-Cu pattern (Figure 5.14a) reveals a combination of small (1.4 nm) and larger (3.4 nm, for the overall average of 2.5 nm) particles. This suggests that particles grow by particle migration, but in any event, the homogeneity of alloying is maintained as particle growth occurs. Once again, even while sintering has occurred the initial surface

composition is maintained. The structure-function relations derived for the initial Pd-Cu catalyst morphologies would also appear to extend in good part to the spent catalysts. In the spent co-SEA Pd-Co catalyst (bottom pattern of Figure 5.13 and Figure 5.14b), pure Pd is revealed by the position of the (111) peak being that of the pure metal. The pattern can be deconvoluted into 3.6 nm pure Pd particles and also 2.0 nm cobalt oxide particles in addition to some remaining PdCo alloyed particles (2.3 nm). Thus this catalyst appears to have dealloyed significantly.

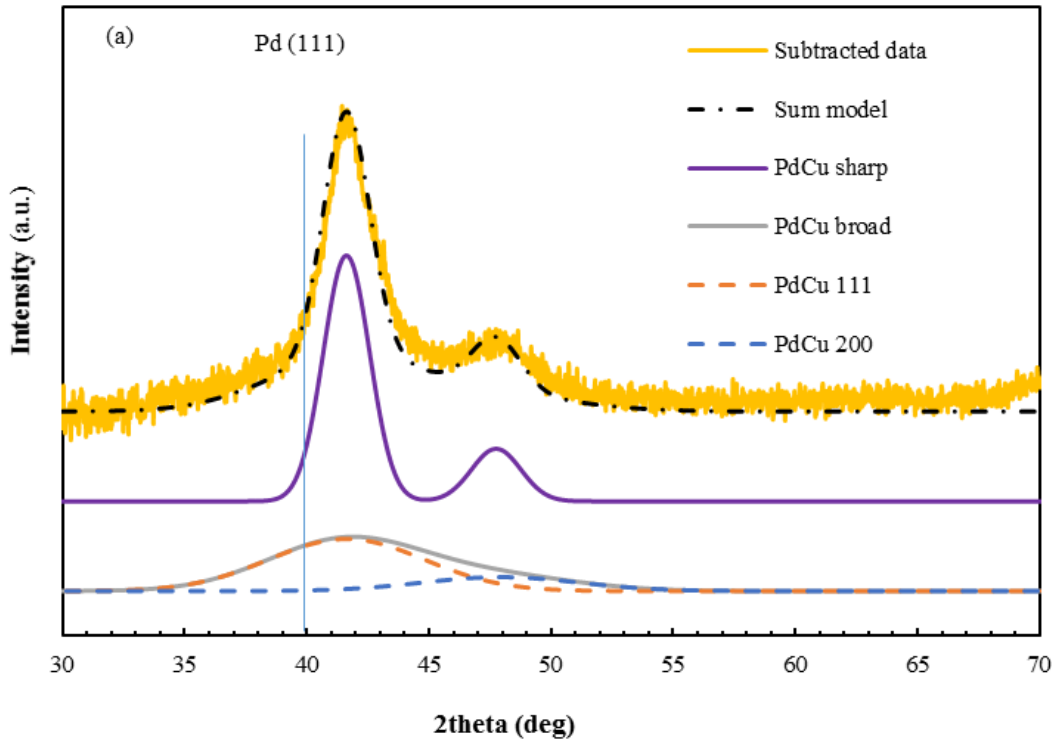

Figure 5.14.a) XRD deconvolution of spent PdCu co-SEA catalyst

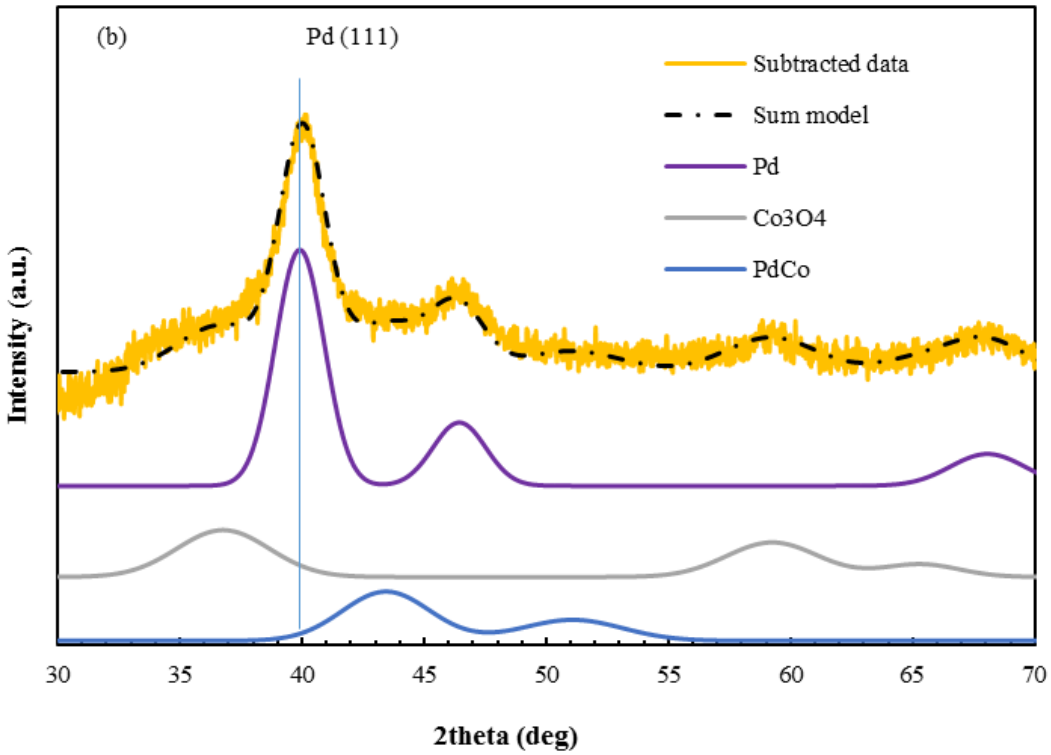

Figure 5.14.b) XRD deconvolution of spent PdCo co-SEA catalyst.

5.3 Conclusion

SEA and co-SEA preparations yielded ultra-small (about 1 nm) single metal Pd, Cu, and Co and homogeneously alloyed PdCu co-SEA and PdCo co-SEA nanoparticles supported on silica. When added as shells via ED to the SEA-synthesized Pd cores, Cu was deposited as one half or nine tenths partial monolayers. The homogeneously alloyed PdCu co-SEA nanoparticles as well as the 9/10ths monolayer Cu coated Pd nanoparticles showed enhanced resistance to sintering in the aqueous reaction environment, whereas the PdCo co-SEA catalyst dealloyed. Pure Pd activity for the sequential conversion of furfural via FAL to either THFAL or COP was high and showed considerable amounts of FAL with mostly CPO as final product. The activity of Cu was low and gave only the COP product,

suggesting that while furfural hydrogenation to the FAL intermediate is slow, activity for the ring arrangement step is higher. Combining Cu with Pd yielded a synergistic catalyst in which the high FFA hydrogenation activity of Pd sites is combined with the high activity of Cu sites.

The method of preparation was seen to be crucial to achieve this synergism; only the co-SEA preparation produced the necessary mixture of surface sites. Cu deposited as partial shells imparted only the activity of Cu, meaning lower overall activity with complete selectivity to CPO. The PdCo co-SEA catalyst was not nearly as active as PdCu co-SEA. In both cases the bimetallic DI catalysts had by far the lowest activity due to very large particle size. The ½ monolayer PdCu SEA-ED catalyst did yield the unique result of being the only formulation to give high amounts of the secondary hydrogenation product, THFAL, instead of the ring-rearranged product CPO.

Reference

1. He, Z.; Wang, X., Hydrodeoxygenation of model compounds and catalytic systems for pyrolysis bio-oils upgrading. *Catalysis for Sustainable Energy* **2012,** *1*.

2. Mortensen, P. M.; Grunwaldt, J.-D.; Jensen, P. A.; Jensen, A. D., Screening of Catalysts for Hydrodeoxygenation of Phenol as a Model Compound for Bio-oil. *Acs Catalysis* **2013,** *3* (8), 1774-1785.

3. O'Connell, K.; Regalbuto, J. R., High Sensitivity Silicon Slit Detectors for 1 nm Powder XRD Size Detection Limit. *Catalysis Letters* **2015,** *145* (3), 777-783.

4. Wang, H.; Male, J.; Wang, Y., Recent Advances in Hydrotreating of Pyrolysis Bio-Oil and Its Oxygen-Containing Model Compounds. *ACS Catalysis* **2013,** *3* (5), 1047-1070.

5. Kazi, F. K.; Fortman, J. A.; Anex, R. P.; Hsu, D. D.; Aden, A.; Dutta, A.; Kothandaraman, G., Techno-economic comparison of process technologies for biochemical ethanol production from corn stover. *Fuel* **2010,** *89*, S20-S28.

6. Furimsky, E., Hydroprocessing challenges in biofuels production. *Catalysis Today* **2013,** *217*, 13-56.

7. Huber, G. W.; Iborra, S.; Corma, A., Synthesis of transportation fuels from biomass: Chemistry, catalysts, and engineering. *Chemical Reviews* **2006,** *106* (9), 4044-4098.

8. Biswas, P.; Narayanasarrna, P.; Kotikalapudi, C. M.; Dalai, A. K.; Adjaye, J., Characterization and Activity of ZrO2 Doped SBA-15 Supported NiMo Catalysts for HDS and HDN of Bitumen Derived Heavy Gas Oil. *Industrial & Engineering Chemistry Research* **2011,** *50* (13), 7882-7895.

9. Wan, H.; Chaudhari, R. V.; Subramaniam, B., Catalytic Hydroprocessing of p-Cresol: Metal, Solvent and Mass-Transfer Effects. *Topics in Catalysis* **2012,** *55* (3-4), 129-139.

10. Nie, L.; de Souza, P. M.; Noronha, F. B.; An, W.; Sooknoi, T.; Resasco, D. E., Selective conversion of m-cresol to toluene over bimetallic Ni-Fe catalysts. *Journal of Molecular Catalysis a-Chemical* **2014,** *388*, 47-55.

11. Parsell, T. H.; Owen, B. C.; Klein, I.; Jarrell, T. M.; Marcum, C. L.; Haupert, L. J.; Amundson, L. M.; Kenttamaa, H. I.; Ribeiro, F.; Miller, J. T.; Abu-Omar, M. M.,

Cleavage and hydrodeoxygenation (HDO) of C-O bonds relevant to lignin conversion using Pd/Zn synergistic catalysis. *Chem. Sci.* **2013,** *4* (2), 806-813.

12. Foster, A. J.; Do, P. T. M.; Lobo, R. F., The Synergy of the Support Acid Function and the Metal Function in the Catalytic Hydrodeoxygenation of m-Cresol. *Topics in Catalysis* **2012,** *55* (3-4), 118-128.

13. Song, W.; Zhao, C.; Lercher, J. A., Importance of Size and Distribution of Ni Nanoparticles for the Hydrodeoxygenation of Microalgae Oil. *Chemistry-a European Journal* **2013,** *19* (30), 9833-9842.

14. Olcese, R.; Carre, V.; Aubriet, F.; Dufour, A., Selectivity of Bio-oils Catalytic Hydrotreatment Assessed by Petroleomic and GC*GC/MS-FID Analysis. *Energy & Fuels* **2013,** *27* (4), 2135-2145.

15. Do, P. T. M.; Foster, A. J.; Chen, J. G.; Lobo, R. F., Bimetallic effects in the hydrodeoxygenation of meta-cresol on gamma-Al2O3 supported Pt-Ni and Pt-Co catalysts. *Green Chemistry* **2012,** *14* (5), 1388-1397.

16. Wildschut, J.; Iqbal, M.; Mahfud, F. H.; Cabrera, I. M.; Venderbosch, R. H.; Heeres, H. J., Insights in the hydrotreatment of fast pyrolysis oil using a ruthenium on carbon catalyst. *Ener. Environ. Sci.* **2010,** *3*, 962-970.

17. Wildschut, J.; Mahfud, F. H.; Venderbosch, R. H.; Heeres, H. J., Hydrotreatment of Fast Pyrolysis Oil Using Heterogeneous Noble-Metal Catalysts. *Industrial & Engineering Chemistry Research* **2009,** *48* (23), 10324-10334.

18. Ohta, H.; Kobayashi, H.; Hara, K.; Fukuoka, A., Hydrodeoxygenation of phenols as lignin models under acid-free conditions with carbon-supported platinum catalysts. *Chemical Communications* **2011,** *47* (44), 12209-12211.

19. Zhao, C.; He, J. Y.; Lemonidou, A. A.; Li, X. B.; Lercher, J. A., Aqueous-phase hydrodeoxygenation of bio-derived phenols to cycloalkanes. *Journal of Catalysis* **2011,** *280* (1), 8-16.

20. Mercader, F. D.; Koehorst, P. J. J.; Heeres, H. J.; Kersten, S. R. A.; Hogendoorn, J. A., Competition Between Hydrotreating and Polymerization Reactions During Pyrolysis Oil Hydrodeoxygenation. *Aiche Journal* **2011,** *57* (11), 3160-3170.

21. Zhang, Q.; Chang, J.; Wang, T.; Xu, Y., Review of biomass pyrolysis oil properties and upgrading research. *Energy Conversion and Management* **2007,** *48* (1), 87-92.

22. Campelo, J. M.; Luna, D.; Luque, R.; Marinas, J. M.; Romero, A. A., Sustainable Preparation of Supported Metal Nanoparticles and Their Applications in Catalysis. *ChemSusChem* **2009,** *2* (1), 18-45.

23. Wang, T.; Mpourmpakis, G.; Lonergan, W. W.; Vlachos, D. G.; Chen, J. G., Effect of oxide supports in stabilizing desirable Pt-Ni bimetallic structures for hydrogenation and reforming reactions. *Physical Chemistry Chemical Physics* **2013,** *15* (29), 12156-12164.

24. Hensley, A. J. R.; Hong, Y.; Zhang, R.; Zhang, H.; Sun, J.; Wang, Y.; McEwen, J.-S., Enhanced Fe2O3Reducibility via Surface Modification with Pd: Characterizing the Synergy within Pd/Fe Catalysts for Hydrodeoxygenation Reactions. *ACS Catalysis* **2014,** *4* (10), 3381-3392.

25. Hong, Y.; Zhang, H.; Sun, J.; Ayman, K. M.; Hensley, A. J. R.; Gu, M.; Engelhard, M. H.; McEwen, J.-S.; Wang, Y., Synergistic Catalysis between Pd and Fe in Gas Phase Hydrodeoxygenation ofm-Cresol. *ACS Catalysis* **2014,** *4* (10), 3335-3345.

26. Hong, Y.; Hensley, A.; McEwen, J.-S.; Wang, Y., Perspective on Catalytic Hydrodeoxygenation of Biomass Pyrolysis Oils: Essential Roles of Fe-Based Catalysts. *Catalysis Letters* **2016,** *146* (9), 1621-1633.

27. Chheda, J. N.; Roman-Leshkov, Y.; Dumesic, J. A., Production of 5-hydroxymethylfurfural and furfural by dehydration of biomass-derived mono- and poly-saccharides. *Green Chemistry* **2007,** *9* (4), 342-350.

28. Sievers, C.; Musin, I.; Marzialetti, T.; Olarte, M. B. V.; Agrawal, P. K.; Jones, C. W., Acid-Catalyzed Conversion of Sugars and Furfurals in an Ionic-Liquid Phase. *ChemSusChem* **2009,** *2* (7), 665-671.

29. Lange, J. P.; van der Heide, E.; van Buijtenen, J.; Price, R., FurfuralυA Promising Platform for Lignocellulosic Biofuels. *Chemsuschem* **2012,** *5* (1), 150-166.

30. Chen, B. F.; Li, F. B.; Huang, Z. J.; Yuan, G. Q., Tuning catalytic selectivity of liquid-phase hydrogenation of furfural via synergistic effects of supported bimetallic catalysts. *Applied Catalysis a-General* **2015,** *500*, 23-29.

31. Lipnick, R. L., NMR-SPECTROSCOPY OF CYCLOPENTANE DERIVATIVES .1. CYCLOPENTANE AND CYCLOPENTANONE. *J. Mol. Struct.* **1974,** *21* (3), 411-421.

32. Dubkov, K. A.; Panov, G. I.; Starokon, E. V.; Parmon, V. N., Non-catalytic liquid phase oxidation of alkenes with nitrous oxide. 2. Oxidation of cyclopentene to cyclopentanone. *React. Kinet. Catal. Lett.* **2002,** *77* (1), 197-205.

33. Store, M. R. Cyclopentanone Market for Pharmaceuticals, Biological, Perfumes & Aromas, Rubber Chemicals, Insecticides and Other Applications: Global Industry Perspective, Comprehensive Analysis, Size, Share, Growth, Segment, Trends and Forecast, 2014 – 2020. http://www.marketresearchstore.com/report/cyclopentanone-market-z41366.

34. Dong, F.; Zhu, Y. L.; Ding, G. Q.; Cui, J. L.; Li, X. Q.; Li, Y. W., One-step Conversion of Furfural into 2-Methyltetrahydrofuran under Mild Conditions. *Chemsuschem* **2015,** *8* (9), 1534-1537.

35. Taylor, M. J.; Durndell, L. J.; Isaacs, M. A.; Parlett, C. M. A.; Wilson, K.; Lee, A. F.; Kyriakou, G., Highly selective hydrogenation of furfural over supported Pt nanoparticles under mild conditions. *Applied Catalysis B-Environmental* **2016,** *180*, 580-585.

36. Lesiak, M.; Binczarski, M.; Karski, S.; Maniukiewicz, W.; Rogowski, J.; Szubiakiewicz, E.; Berlowska, J.; Dziugan, P.; Witonska, I., Hydrogenation of furfural over Pd-Cu/Al2O3 catalysts. The role of interaction between palladium and copper on determining catalytic properties. *Journal of Molecular Catalysis a-Chemical* **2014,** *395*, 337-348.

37. Hronec, M.; Fulajtarova, K.; Liptaj, T., Effect of catalyst and solvent on the furan ring rearrangement to cyclopentanone. *Applied Catalysis a-General* **2012,** *437*, 104-111.

38. Biradar, N. S.; Hengne, A. A.; Birajdar, S. N.; Swami, R.; Rode, C. V., Tailoring the Product Distribution with Batch and Continuous Process Options in Catalytic Hydrogenation of Furfural. *Organic Process Research & Development* **2014,** *18* (11), 1434-1442.

39. Dong, F.; Zhu, Y. L.; Zheng, H. Y.; Zhu, Y. F.; Li, X. Q.; Li, Y. W., Cr-free Cu-catalysts for the selective hydrogenation of biomass-derived furfural to 2-methylfuran: The synergistic effect of metal and acid sites. *Journal of Molecular Catalysis a-Chemical* **2015,** *398*, 140-148.

40. Bhogeswararao, S.; Srinivas, D., Catalytic conversion of furfural to industrial chemicals over supported Pt and Pd catalysts. *Journal of Catalysis* **2015,** *327*, 65-77.

41. Shi, D. M.; Vohs, J. M., Deoxygenation of Biomass-Derived Oxygenates: Reaction of Furfural on Zn-Modified Pt(111). *Acs Catalysis* **2015,** *5* (4), 2177-2183.

42. Fulajtarova, K.; Sotak, T.; Hronec, M.; Vavra, I.; Dobrocka, E.; Omastova, M., Aqueous phase hydrogenation of furfural to furfuryl alcohol over Pd-Cu catalysts. *Applied Catalysis a-General* **2015,** *502*, 78-85.

43. Hronec, M.; Fulajtarova, K.; Vavra, I.; Sotak, T.; Dobrocka, E.; Micusik, M., Carbon supported Pd-Cu catalysts for highly selective rearrangement of furfural to cyclopentanone. *Applied Catalysis B-Environmental* **2016,** *181*, 210-219.

44. Li, X. L.; Deng, J.; Shi, J.; Pan, T.; Yu, C. G.; Xu, H. J.; Fu, Y., Selective conversion of furfural to cyclopentanone or cyclopentanol using different preparation methods of Cu-Co catalysts. *Green Chemistry* **2015,** *17* (2), 1038-1046.

45. Zahir, M. H.; Sato, K.; Mori, H.; Iwamoto, Y., Preparation and properties of hydrothermally stable gamma-alumina-based composite mesoporous membranes. *Journal of the American Ceramic Society* **2006,** *89* (9), 2874-2880.

46. Valle, B.; Gayubo, A. G.; Alonso, A.; Aguayo, A. T.; Bilbao, J., Hydrothermally stable HZSM-5 zeolite catalysts for the transformation of crude bio-oil into hydrocarbons. *Applied Catalysis B-Environmental* **2010,** *100* (1-2), 318-327.

47. Palella, B. I.; Lisi, L.; Pirone, R.; Russo, G.; Notaro, M., Enhancement of hydrothermal stability of Cu-ZSM5 catalyst for NO decomposition. *Kinetics and Catalysis* **2006,** *47* (5), 728-736.

48. Ravenelle, R. M.; Schuessler, F.; D'Amico, A.; Danilina, N.; van Bokhoven, J. A.; Lercher, J. A.; Jones, C. W.; Sievers, C., Stability of Zeolites in Hot Liquid Water. *Journal of Physical Chemistry C* **2010,** *114* (46), 19582-19595.

49. Pharn, H. N.; Pagan-Torres, Y. J.; Serrano-Ruiz, J. C.; Wang, D.; Dumesic, J. A.; Datye, A. K., Improved hydrothermal stability of niobia-supported Pd catalysts. *Applied Catalysis a-General* **2011,** *397* (1-2), 153-162.

50. Han, Y.; Li, N.; Zhao, L.; Li, D. F.; Xu, X. Z.; Wu, S.; Di, Y.; Li, C. J.; Zou, Y. C.; Yu, Y.; Xiao, F. S., Understanding of the high hydrothermal stability of the mesoporous materials prepared by the assembly of triblock copolymer with preformed zeolite precursors in acidic media. *Journal of Physical Chemistry B* **2003,** *107* (31), 7551-7556.

51. Samuel Chung, Q. L., Upendra A. Joshi, John R. Regalbuto, Kwesi Boateng, Michael Smith, Charles Coe, Using Polyfurfuryl Alcohol to Improve the Hydrothermal Stability of Mesoporous Oxides for Reactions in the Aqueous Phase. 2017.

52. Hahn, M. W.; Copeland, J. R.; van Pelt, A. H.; Sievers, C., Stability of Amorphous Silica-Alumina in Hot Liquid Water. *ChemSusChem* **2013,** *6* (12), 2304-2315.

53. Mokaya, R., Al content dependent hydrothermal stability of directly synthesized aluminosilicate MCM-41. *Journal of Physical Chemistry B* **2000,** *104* (34), 8279-8286.

54. Pagán-Torres, Y. J.; Gallo, J. M. R.; Wang, D.; Pham, H. N.; Libera, J. A.; Marshall, C. L.; Elam, J. W.; Datye, A. K.; Dumesic, J. A., Synthesis of Highly Ordered Hydrothermally Stable Mesoporous Niobia Catalysts by Atomic Layer Deposition. *ACS Catalysis* **2011,** *1* (10), 1234-1245.

55. Pham, H. N.; Anderson, A. E.; Johnson, R. L.; Schmidt-Rohr, K.; Datye, A. K., Improved hydrothermal stability of mesoporous oxides for reactions in the aqueous phase. *Angew Chem Int Ed Engl* **2012,** *51* (52), 13163-7.

56. Xiong, H.; Pham, H. N.; Datye, A. K., A facile approach for the synthesis of niobia/carbon composites having improved hydrothermal stability for aqueous-phase reactions. *Journal of Catalysis* **2013,** *302*, 93-100.

57. Xiong, H.; Nolan, M.; Shanks, B. H.; Datye, A. K., Comparison of impregnation and deposition precipitation for the synthesis of hydrothermally stable niobia/carbon. *Applied Catalysis A: General* **2014,** *471*, 165-174.

58. Zapata, P. A.; Faria, J.; Ruiz, M. P.; Jentoft, R. E.; Resasco, D. E., Hydrophobic Zeolites for Biofuel Upgrading Reactions at the Liquid-Liquid Interface in Water/Oil Emulsions. *Journal of the American Chemical Society* **2012,** *134* (20), 8570-8578.

59. Wei, J.; Shi, J.; Pan, H.; Su, Q.; Zhu, J.; Shi, Y., Thermal and hydrothermal stability of amino-functionalized SBA-16 and promotion of hydrophobicity by silylation. *Microporous and Mesoporous Materials* **2009,** *117* (3), 596-602.

60. van Dillen, A. J.; Terorde, R.; Lensveld, D. J.; Geus, J. W.; de Jong, K. P., Synthesis of supported catalysts by impregnation and drying using aqueous chelated metal complexes. *Journal of Catalysis* **2003,** *216* (1-2), 257-264.

61. Geus, J. W., *Production and thermal pretreatment of supported catalysts*. 1983; Vol. 16, p 1-33.

62. Regalbuto, J. R., Electrostatic Adsorption. In *Synthesis of Solid Catalysts;*, Jong, K. P. d., Ed. Wiley-VCH Verlag GmbH & Co.: Weinheim,: 2009; pp 33-58.

63. Jong, K. P. d., *Synthesis of supported catalysts*. 1999; Vol. 4.

64. Nguyen, D. L.; Umbarkar, S.; Dongare, M. K.; Lancelot, C.; Girardon, J. S.; Dujardin, C.; Granger, P., Deposition–precipitation versus anionic-exchange Au/Al2O3 catalysts: A comparative investigation towards the selective reduction of NOx. *Catalysis Communications* **2012,** *26*, 225-230.

65. Zanella, R., Crotonaldehyde hydrogenation by gold supported on TiO2: structure sensitivity and mechanism. *Journal of Catalysis* **2004,** *223* (2), 328-339.

66. Burattin, P.; Che, M.; Louis, C., Characterization of the Ni(II) phase formed on silica upon deposition-precipitation. *Journal of Physical Chemistry B* **1997,** *101* (36), 7060-7074.

67. Bamwenda, G. R.; Tsubota, S.; Nakamura, T.; Haruta, M., The influence of the preparation methods on the catalytic activity of platinum and gold supported on TiO2 for CO oxidation. *Catalysis Letters* **1997,** *44* (1-2), 83-87.

68. Zanella, R.; Giorgio, S.; Henry, C. R.; Louis, C., Alternative methods for the preparation of gold nanoparticles supported on TiO2. *Journal of Physical Chemistry B* **2002,** *106* (31), 7634-7642.

69. Brunelle, J. P., Preparation of catalysts by metallic complex adsorption on mineral oxides. *Pure Appli. Chem.* **1978,** *50*.

70. Liu, Q.; Joshi, U. A.; Uber, K.; Regalbuto, J. R., The control of Pt and Ru nanoparticle size on high surface area supports. *Physical Chemistry Chemical Physics* **2014,** *16* (48), 26431-26435.

71. Cao, S.; Monnier, J. R.; Williams, C. T.; Diao, W. J.; Regalbuto, J. R., Rational nanoparticle synthesis to determine the effects of size, support, and K dopant on Ru activity for levulinic acid hydrogenation to gamma-valerolactone. *Journal of Catalysis* **2015,** *326*, 69-81.

72. Jiao, L.; Regalbuto, J. R., The synthesis of highly dispersed noble and base metals on silica via strong electrostatic adsorption: I. Amorphous silica. *Journal of Catalysis* **2008,** *260* (2), 329-341.

73. Zhu, X.; Cho, H.-r.; Pasupong, M.; Regalbuto, J. R., Charge-Enhanced Dry Impregnation: A Simple Way to Improve the Preparation of Supported Metal Catalysts. *Acs Catalysis* **2013,** *3* (4), 625-630.

74. Cao, C. J.; Yang, G.; Dubau, L.; Maillard, F.; Lambert, S. D.; Pirard, J. P.; Job, N., Highly dispersed Pt/C catalysts prepared by the Charge Enhanced Dry Impregnation method. *Applied Catalysis B-Environmental* **2014,** *150*, 101-106.

75. Samad, J. E.; Hoenig, S.; Regalbuto, J. R., Synthesis of Platinum Catalysts over Thick Slurries of Oxide Supports by Strong Electrostatic Adsorption. *ChemCatChem* **2015,** *7* (21), 3460-3463.

76. Cao, S.; Monnier, J. R.; Williams, C. T.; Diao, W.; Regalbuto, J. R., Rational nanoparticle synthesis to determine the effects of size, support, and K dopant on Ru activity for levulinic acid hydrogenation to gamma-valerolactone. *Journal of Catalysis* **2015,** *326*, 69-81.

77. Jiao, L.; Regalbuto, J. R., The synthesis of highly dispersed noble and base metals on silica via strong electrostatic adsorption: II. Mesoporous silica SBA-15. *Journal of Catalysis* **2008,** *260* (2), 342-350.

78. Liu, Q., Samad, J. E., Copple, J. E., Eskandari, S., Satterwhite, C., Regalbuto, J. R., A pinch of salt to control supported Pt nanoparticle size. *Catalysis Today* **2017,** *280*.

79. Tengco, J. M. M.; Mehrabadi, B. A. T.; Zhang, Y. Y.; Wongkaew, A.; Regalbuto, J. R.; Weidner, J. W.; Monnier, J. R., Synthesis and Electrochemical Evaluation of Carbon Supported Pt-Co Bimetallic Catalysts Prepared by Electroless Deposition and Modified Charge Enhanced Dry Impregnation. *Catalysts* **2016,** *6* (6).

80. Zhu, X. R.; Cho, H. R.; Pasupong, M.; Regalbuto, J. R., Charge-Enhanced Dry Impregnation: A Simple Way to Improve the Preparation of Supported Metal Catalysts. *Acs Catalysis* **2013,** *3* (4), 625-630.

81. Park, J.; Regalbuto, J. R., SIMPLE, ACCURATE DETERMINATION OF OXIDE PZC AND THE STRONG BUFFERING EFFECT OF OXIDE SURFACES AT INCIPIENT WETNESS. *Journal of Colloid and Interface Science* **1995,** *175* (1), 239-252.

82. Cho, H. R.; Regalbuto, J. R., The rational synthesis of Pt-Pd bimetallic catalysts by electrostatic adsorption. *Catalysis Today* **2015,** *246*, 143-153.

83. Wong, A. P.; Kyriakidou, E. A.; Toops, T. J.; Regalbuto, J. R., The catalytic behavior of precisely synthesized Pt-Pd bimetallic catalysts for use as diesel oxidation catalysts. *Catalysis Today* **2016,** *267*, 145-156.

84. Rebelli, J.; Detwiler, M.; Ma, S. G.; Williams, C. T.; Monnier, J. R., Synthesis and characterization of Au-Pd/SiO2 bimetallic catalysts prepared by electroless deposition. *Journal of Catalysis* **2010,** *270* (2), 224-233.

85. Djokic, S., . *Mod. Aspect. Electroc.* **2002,** *35*, 83.

86. Schaal, M. T.; Metcalf, A. Y.; Montoya, J. H.; Wilkinson, J. P.; Stork, C. C.; Williams, C. T.; Monnier, J. R., Hydrogenation of 3,4-epoxy-1-butene over Cu-Pd/SiO2 catalysts prepared by electroless deposition. *Catalysis Today* **2007,** *123* (1-4), 142-150.

87. Schaal, M. T.; Pickerel, A. C.; Williams, C. T.; Monnier, J. R., Characterization and evaluation of Ag-Pt/SiO2 catalysts prepared by electroless deposition. *Journal of Catalysis* **2008,** *254* (1), 131-143.

88. Beard, K. D.; Borrelli, D.; Cramer, A. M.; Blom, D.; Van Zee, J. W.; Monnier, J. R., Preparation and Structural Analysis of Carbon-Supported Co Core/Pt Shell Electrocatalysts Using Electroless Deposition Methods. *ACS Nano* **2009,** *3* (9), 2841-2853.

89. Zhang, Y. Y.; Diao, W. J.; Williams, C. T.; Monnier, J. R., Selective hydrogenation of acetylene in excess ethylene using Ag- and Au-Pd/SiO2 bimetallic catalysts prepared by electroless deposition. *Applied Catalysis a-General* **2014,** *469*, 419-426.

90. Zhang, Y. Y.; Diao, W. J.; Monnier, J. R.; Williams, C. T., Pd-Ag/SiO2 bimetallic catalysts prepared by galvanic displacement for selective hydrogenation of acetylene in excess ethylene. *Catalysis Science & Technology* **2015,** *5* (8), 4123-4132.

91. Xiong, H.; Pham, H. N.; Datye, A. K., Hydrothermally stable heterogeneous catalysts for conversion of biorenewables. *Green Chem.* **2014,** *16* (11), 4627-4643.

92. Zhao, D. Y.; Feng, J. L.; Huo, Q. S.; Melosh, N.; Fredrickson, G. H.; Chmelka, B. F.; Stucky, G. D., Triblock copolymer syntheses of mesoporous silica with periodic 50 to 300 angstrom pores. *Science* **1998,** *279* (5350), 548-552.

93. Goguet, A.; Schweich, D.; Candy, J. P., Preparation of a Pt/SiO2 catalyst II. Temperature-programmed decomposition of the adsorbed platinum tetrammine hydroxide complex under flowing hydrogen, oxygen, and argon. *Journal of Catalysis* **2003,** *220* (2), 280-290.

94. Shah, A. M.; Regalbuto, J. R., RETARDATION OF PT ADSORPTION OVER OXIDE SUPPORTS AT PH EXTREMES - OXIDE DISSOLUTION OR HIGH IONIC-STRENGTH. *Langmuir* **1994,** *10* (2), 500-504.

95. Ravenelle, R. M.; Copeland, J. R.; Kim, W.-G.; Crittenden, J. C.; Sievers, C., Structural Changes of gamma-Al2O3-Supported Catalysts in Hot Liquid Water. *Acs Catalysis* **2011,** *1* (5), 552-561.

96. Yaseen Elkasabi, Q. L., Yongsuck Choi, Akwasi A. Boateng, John R. Regalbuto, Novel bio-oil hydrodeoxygenation catalysts produced using strong electrostatic adsorption, 2017.

97. Mullen, C. A.; Strahan, G. D.; Boateng, A. A., Characterization of Various Fast-Pyrolysis Bio-Oils by NMR Spectroscopy. *Energ. Fuel.* **2009,** *23*, 2707-2718.

98. Barbier, J.; Bahloul, D.; Marecot, P., EFFECT OF CHLORIDE ON SINTERING OF PT/AL2O3 CATALYSTS. *Catalysis Letters* **1991,** *8* (5-6), 327-334.

99. Borgna, A.; Garetto, T. F.; Apesteguia, C. R.; Le Normand, F.; Moraweck, B., Sintering of chlorinated Pt/gamma-Al2O3 catalysts: An in situ study by X-ray absorption spectroscopy. *Journal of Catalysis* **1999,** *186* (2), 433-441.

100. Monzon, A.; Garetto, T. F.; Borgna, A., Sintering and redispersion of Pt/gamma-Al2O3 catalysts: a kinetic model. *Applied Catalysis a-General* **2003,** *248* (1-2), 279-289.

101. Hayashi, T.; Tanaka, K.; Haruta, M., Selective vapor-phase epoxidation of propylene over Au/TiO2 catalysts in the presence of oxygen and hydrogen. *Journal of Catalysis* **1998,** *178* (2), 566-575.

102. Bezemer, G. L.; Bitter, J. H.; Kuipers, H.; Oosterbeek, H.; Holewijn, J. E.; Xu, X. D.; Kapteijn, F.; van Dillen, A. J.; de Jong, K. P., Cobalt particle size effects in the Fischer-Tropsch reaction studied with carbon nanofiber supported catalysts. *Journal of the American Chemical Society* **2006,** *128* (12), 3956-3964.

103. Mayrhofer, K. J. J.; Blizanac, B. B.; Arenz, M.; Stamenkovic, V. R.; Ross, P. N.; Markovic, N. M., The impact of geometric and surface electronic properties of Pt-catalysts on the particle size effect in electocatalysis. *Journal of Physical Chemistry B* **2005,** *109* (30), 14433-14440.

104. Liu, H. P.; Lu, G. Z.; Guo, Y.; Wang, Y. Q.; Guo, Y. L., Synthesis of mesoporous Pt/Al2O3 catalysts with high catalytic performance for hydrogenation of acetophenone. *Catalysis Communications* **2009,** *10* (9), 1324-1329.

105. Haneda, M.; Watanabe, T.; Kamiuchi, N.; Ozawa, M., Effect of platinum dispersion on the catalytic activity of Pt/Al2O3 for the oxidation of carbon monoxide and propene. *Applied Catalysis B: Environmental* **2013,** *142-143*, 8-14.

106. Auvray, X.; Olsson, L., Stability and activity of Pd-, Pt- and Pd–Pt catalysts supported on alumina for NO oxidation. *Applied Catalysis B: Environmental* **2015,** *168-169*, 342-352.

107. Contreras, J. L.; Gómez, G.; Zeifert, B.; Salmones, J.; Vázquez, T.; Fuentes, G. A.; Navarrete, J.; Nuño, L., Synthesis of Pt/Al2O3 catalyst using mesoporous alumina prepared with a cationic surfactant. *Catalysis Today* **2015,** *250*, 72-86.

108. Zanuttini, M. S.; Lago, C. D.; Querini, C. A.; Peralta, M. A., Deoxygenation of m-cresol on Pt/γ-Al2O3 catalysts. *Catalysis Today* **2013,** *213*, 9-17.

109. An, N.; Yuan, X.; Pan, B.; Li, Q.; Li, S.; Zhang, W., Design of a highly active Pt/Al2O3catalyst for low-temperature CO oxidation. *RSC Advances* **2014,** *4* (72), 38250.

110. Ivanova, A. S.; Slavinskaya, E. M.; Gulyaev, R. V.; Zaikovskii, V. I.; Stonkus, O. A.; Danilova, I. G.; Plyasova, L. M.; Polukhina, I. A.; Boronin, A. I., Metal–support interactions in Pt/Al2O3 and Pd/Al2O3 catalysts for CO oxidation. *Applied Catalysis B: Environmental* **2010,** *97* (1-2), 57-71.

111. Challa, S. R.; Delariva, A. T.; Hansen, T. W.; Helveg, S.; Sehested, J.; Hansen, P. L.; Garzon, F.; Datye, A. K., Relating Rates of Catalyst Sintering to the Disappearance of Individual Nanoparticles during Ostwald Ripening. *Journal of the American Chemical Society* **2011,** *133* (51), 20672-20675.

112. Hansen, T. W.; Delariva, A. T.; Challa, S. R.; Datye, A. K., Sintering of Catalytic Nanoparticles: Particle Migration or Ostwald Ripening? *Accounts of Chemical Research* **2013,** *46* (8), 1720-1730.

113. Deshmane, V. G.; Owen, S. L.; Abrokwah, R. Y.; Kuila, D., Mesoporous nanocrystalline TiO2 supported metal (Cu, Co, Ni, Pd, Zn, and Sn) catalysts: Effect of metal-support interactions on steam reforming of methanol. *Journal of Molecular Catalysis a-Chemical* **2015,** *408*, 202-213.

114. Goula, M. A.; Charisiou, N. D.; Papageridis, K. N.; Delimitis, A.; Pachatouridou, E.; Iliopoulou, E. F., Nickel on alumina catalysts for the production of hydrogen rich mixtures via the biogas dry reforming reaction: Influence of the synthesis method. *International Journal of Hydrogen Energy* **2015,** *40* (30), 9183-9200.

115. Tavasoli, A.; Abbaslou, R. M. M.; Trepanier, M.; Dalai, A. K., Fischer-Tropsch synthesis over cobalt catalyst supported on carbon nanotubes in a slurry reactor. *Applied Catalysis a-General* **2008,** *345* (2), 134-142.

116. Foger, K.; Jaeger, H., THE EFFECT OF CHLORINE TREATMENT ON THE DISPERSION OF PLATINUM METAL PARTICLES SUPPORTED ON SILICA AND GAMMA-ALUMINA. *Journal of Catalysis* **1985,** *92* (1), 64-78.

117. Schreier, M.; Feltes, T. E.; Schaal, M. T.; Regalbuto, J. R., The determination of oxide surface charging parameters for a predictive metal adsorption model. *Journal of Colloid and Interface Science* **2010,** *348* (2), 571-578.

118. Oosawa, Y.; Gratzel, M., EFFECT OF SURFACE HYDROXYL DENSITY ON PHOTOCATALYTIC OXYGEN GENERATION IN AQUEOUS TIO2 SUSPENSIONS. *Journal of the Chemical Society-Faraday Transactions I* **1988,** *84*, 197-205.

119. Samad, J. E.; Hashim, S.; Ma, S.; Regalbuto, J. R., Determining surface composition of mixed oxides with pH. *Journal of Colloid and Interface Science* **2014,** *436*, 204-210.

120. Pellenbarg, T.; Dementev, N.; Jean-Gilles, R.; Bessel, C.; Borguet, E.; Dollahon, N.; Giuliano, R., Detecting and quantifying oxygen functional groups on graphite nanofibers by fluorescence labeling of surface species. *Carbon* **2010,** *48* (15), 4256-4267.

121. Schaidle, J. A.; Schweitzer, N. M.; Ajenifujah, O. T.; Thompson, L. T., On the preparation of molybdenum carbide-supported metal catalysts. *Journal of Catalysis* **2012,** *289*, 210-217.

122. Schweitzer, N. M.; Schaidle, J. A.; Ezekoye, O. K.; Pan, X.; Linic, S.; Thompson, L. T., High activity carbide supported catalysts for water gas shift. *J Am Chem Soc* **2011,** *133* (8), 2378-81.

123. Job, N.; Chatenet, M.; Berthon-Fabry, S.; Hermans, S.; Maillard, F., Efficient Pt/carbon electrocatalysts for proton exchange membrane fuel cells: Avoid chloride-based Pt salts! *Journal of Power Sources* **2013,** *240*, 294-305.

124. Zhang, J. Z.; Colón-Mercado, H. R.; Goodwin, J. G., The effect of low concentrations of tetrachloroethylene on H2 adsorption and activation on Pt in a fuel cell catalyst. *Journal of Power Sources* **2011,** *196* (20), 8391-8397.

125. Banerjee, R. L., Q.; Samad, J. E.; Tengco, J. M. and Regalbuto, J. R., Ambient Oxidation of Ultrasmall Supported Platinum Nanoparticles with Benchtop Powder X-ray Diffraction, Ambient Oxidation of Ultrasmall Supported Platinum Nanoparticles with Benchtop Powder X-ray Diffraction. 2017.

126. Tettenhorst R., H. D. A., 1980, 28 (5), 373-380., Crystal chemistry of boehmite. . *Clays and Clay Minerals* **1987,** *28* (5).

127. Gre´gory Lefe`vre, M. D., Patrick Lepeut, Renaud Caplain,and; Fe´doroff, M., Hydroation of gamma alumina in water and its effects of surface reactivity. *Langmuir* **2002,** *18*, 7.

128. Chen, Y.; Choi, S.; Thompson, L. T., Ethyl formate hydrogenolysis over Mo2C-based catalysts: Towards low temperature CO and CO2 hydrogenation to methanol. *Catalysis Today* **2016,** *259*, 285-291.

129. Zhao, Y.; Yao, Z.; Shi, Y.; Qiao, X.; Wang, G.; Wang, H.; Yin, J.; Peng, F., A novel approach to the synthesis of bulk and supported β-Mo2C using dimethyl ether as a carbon source. *New J. Chem.* **2015,** *39* (6), 4901-4908.

130. Alonso, D. M.; Bond, J. Q.; Dumesic, J. A., Catalytic conversion of biomass to biofuels. *Green Chemistry* **2010,** *12* (9), 1493-1513.

131. Vojtko, J., New way of production of cyclopentanone. *Petroleum & Coal* **2005,** *47* (1), 4.

132. Guo, J. H.; Xu, G. Y.; Han, Z.; Zhang, Y.; Fu, Y.; Guo, Q. X., Selective Conversion of Furfural to Cyclopentanone with CuZnAl Catalysts. *Acs Sustainable Chemistry & Engineering* **2014,** *2* (10), 2259-2266.

133. Hronec, M.; Fulajtarova, K., Selective transformation of furfural to cyclopentanone. *Catalysis Communications* **2012,** *24*, 100-104.

134. Rebelli, J.; Rodriguez, A. A.; Ma, S.; Williams, C. T.; Monnier, J. R., Preparation and characterization of silica-supported, group IB–Pd bimetallic catalysts prepared by electroless deposition methods. *Catalysis Today* **2011,** *160* (1), 170-178.

135. Tang, C.-W.; Wang, C.-B.; Chien, S.-H., Characterization of cobalt oxides studied by FT-IR, Raman, TPR and TG-MS. *Thermochimica Acta* **2008,** *473* (1-2), 68-73.

136. Hronec, M.; Fulajtarova, K.; Sotak, T., Highly selective rearrangement of furfuryl alcohol to cyclopentanone. *Applied Catalysis B-Environmental* **2014,** *154*, 294-300.

137. Hronec, M.; Fulajtárová, K.; Soták, T., Kinetics of high temperature conversion of furfuryl alcohol in water. *Journal of Industrial and Engineering Chemistry* **2014,** *20* (2), 650-655.

138. Li, G.; Li, N.; Zheng, M.; Li, S.; Wang, A.; Cong, Y.; Wang, X.; Zhang, T., Industrially scalable and cost-effective synthesis of 1,3-cyclopentanediol with furfuryl alcohol from lignocellulose. *Green Chem.* **2016,** *18* (12), 3607-3613.

139. Xu, W. J.; Liu, X. H.; Ren, J. W.; Zhang, P.; Wang, Y. Q.; Guo, Y. L.; Guo, Y.; Lu, G. Z., A novel mesoporous Pd/cobalt aluminate bifunctional catalyst for aldol condensation and following hydrogenation. *Catalysis Communications* **2010,** *11* (8), 721-726.

140. Yuan, Q. Q.; Zhang, D. M.; van Haandel, L.; Ye, F. Y.; Xue, T.; Hensen, E. J. M.; Guan, Y. J., Selective liquid phase hydrogenation of furfural to furfuryl alcohol by Ru/Zr-MOFs. *Journal of Molecular Catalysis a-Chemical* **2015,** *406*, 58-64.

Appendix A

Supporting information for furfural hydrogenation

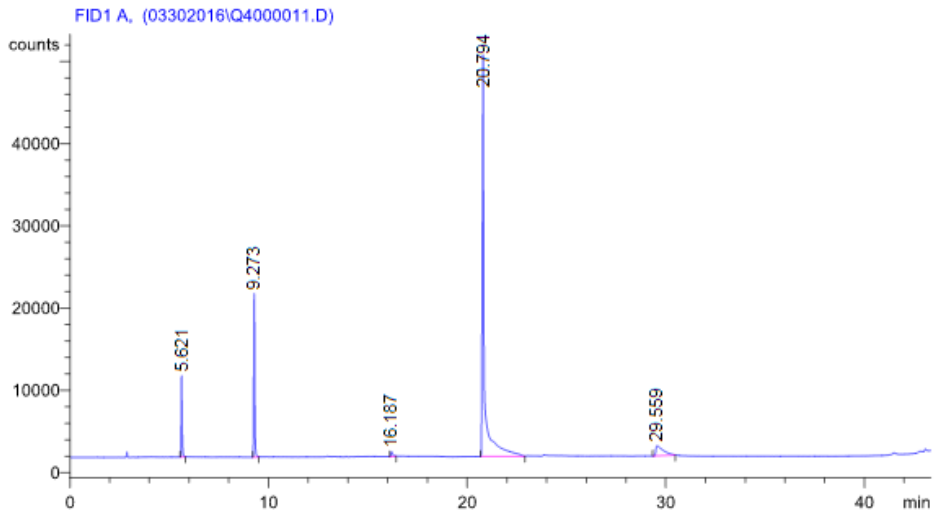

Figure A1:Product analysis of 0.7%Pd/SiO_2 after 3 hours (150^oC) in GC chart; t=2.301 min,furan; t=5.621 min: standard, dioxane; t=9.273 min,cyclopentanone; t=16.187 min: cyclopentanol; t=20.794 min: furfural; t=29.559 min,furfuryl alcohol;scarce amount of furan and cyclopentanol only were observed in the final products.

Table A1 pH measurement after 3 hours reaction.

Catalyst	Ph
1.3%Pd% SEA	3.5
1.2%Pd-0.5%Cu SEA	3.0
0.4%Cu-1.3%Pd SEA-ED	3.2
1.2%Pd-0.5%Cu DI	3.2
2.3%Cu SEA	3.1

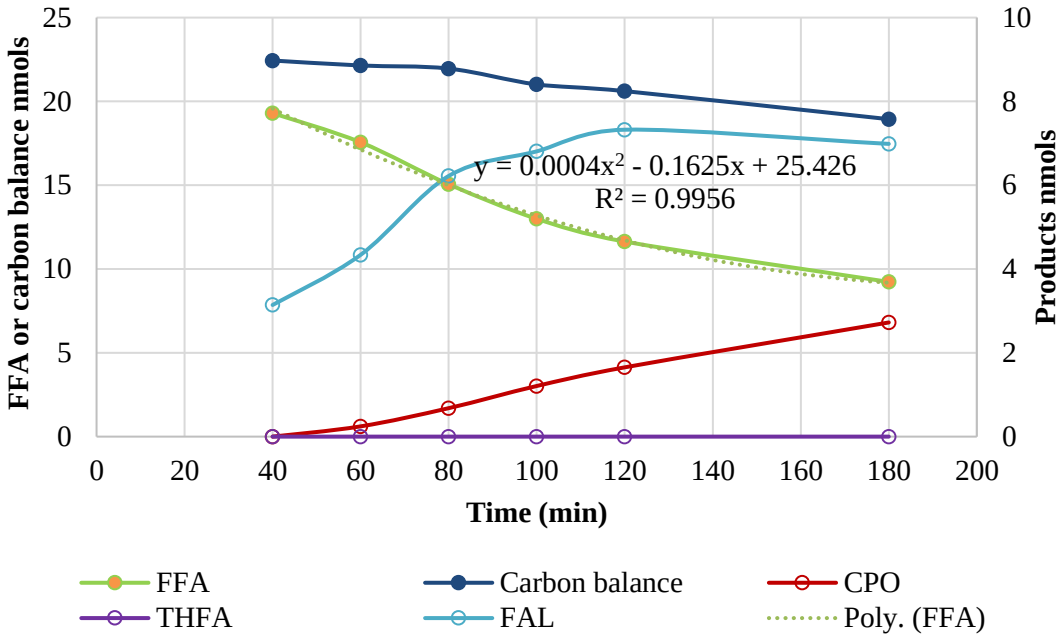

Figure A2 Product analysis of 1.3%Pd/SiO_2; solide circles are by primary axis (left) and empty circles follow secondary axis (right).

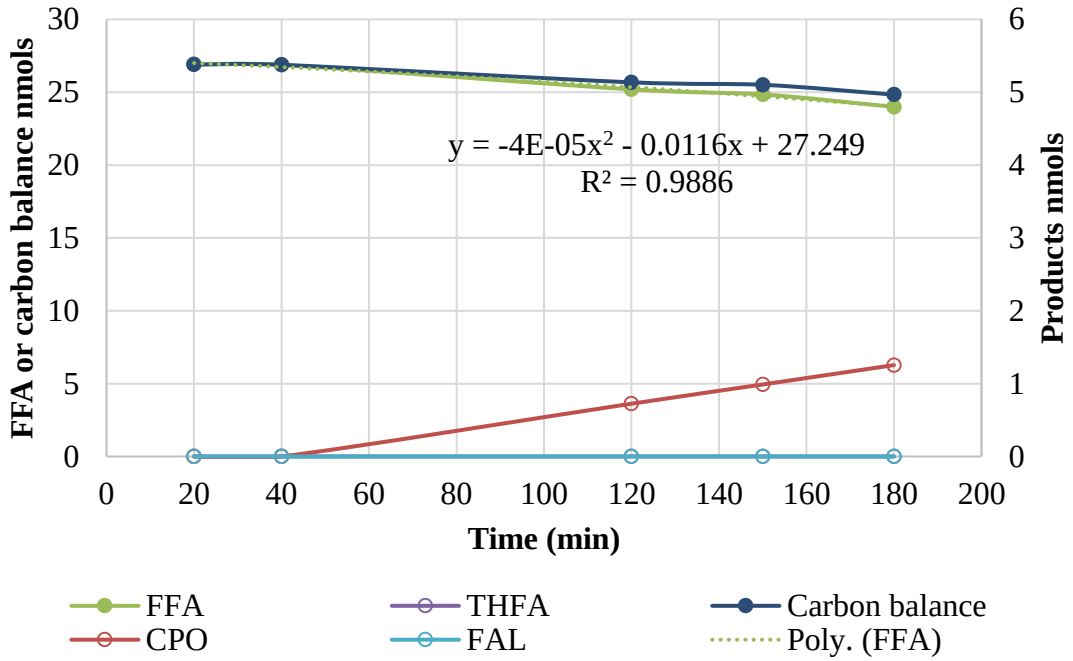

Figure A3 Product analysis of 2.3%Cu/SiO_2; solide circles are by primary axis (left) and empty circles follow secondary axis (right).

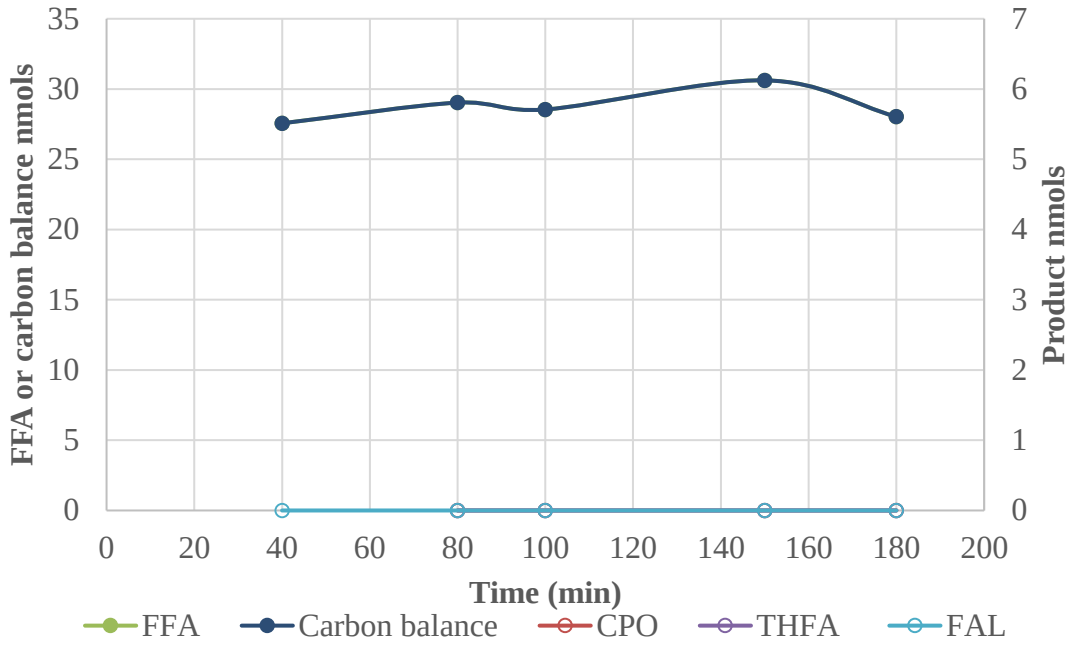

Figure A4 Product analysis of 0.85%Co/SiO_2; solide circles are by primary axis (left) and empty circles follow secondary axis (right).

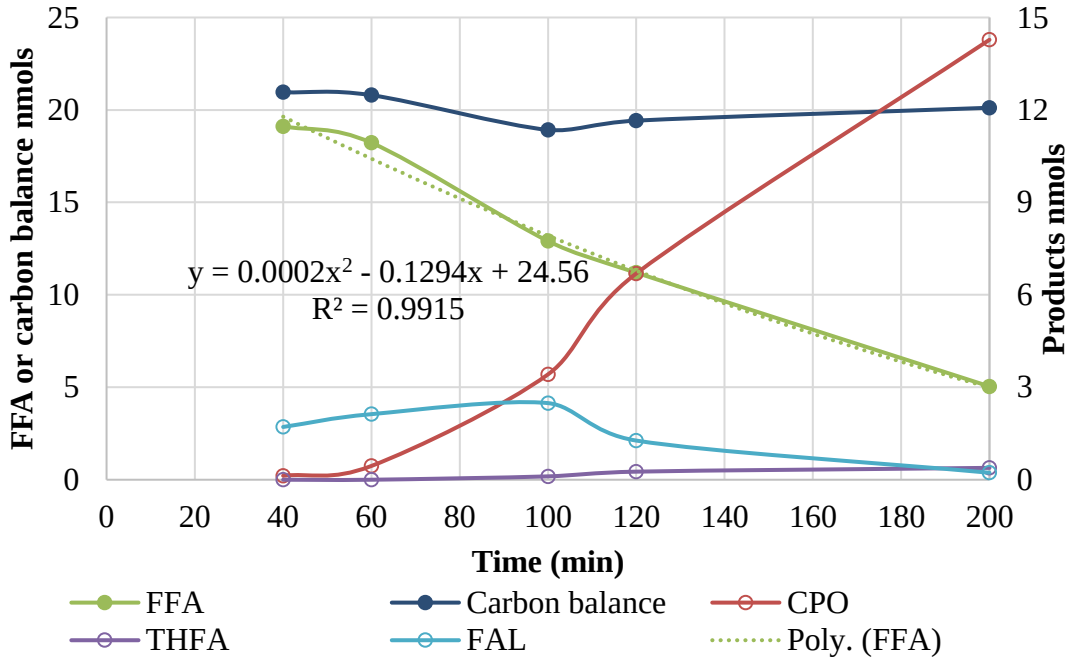

Figure A5 Product analysis of 1.2%Pd-0.5%Cu/SiO_2 SEA; solide circles are by primary axis (left) and empty circles follow secondary axis (right).

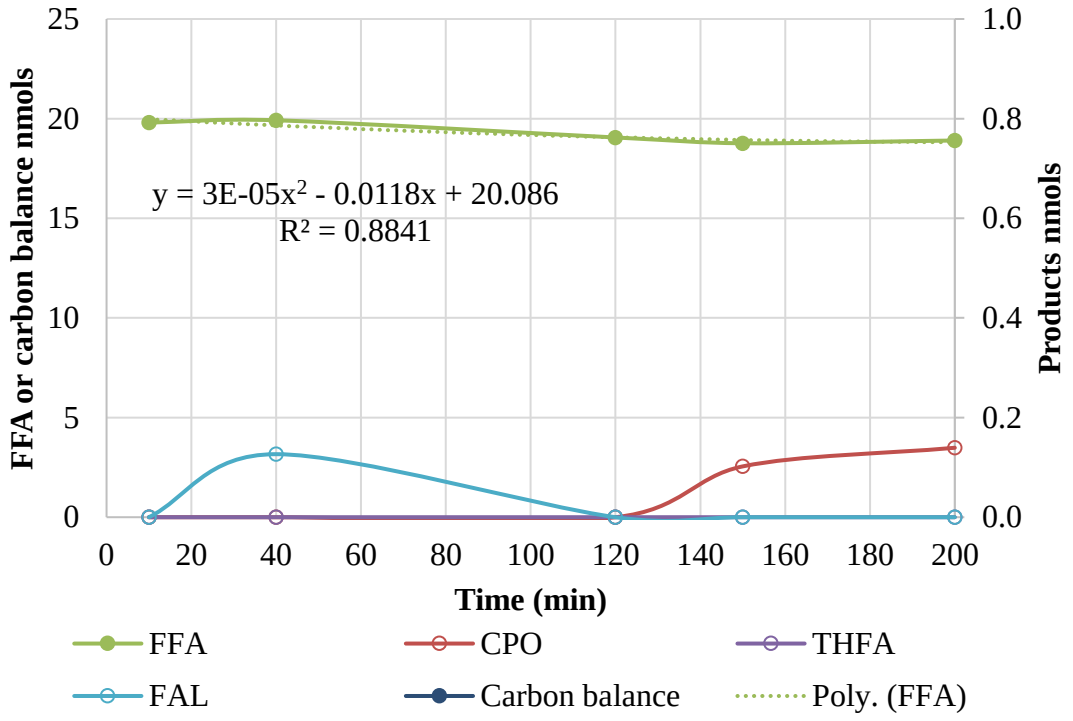

Figure A6 Product analysis of 1.2%Pd-0.5%Cu/SiO_2 DI; solide circles are by primary axis (left) and empty circles follow secondary axis (right).

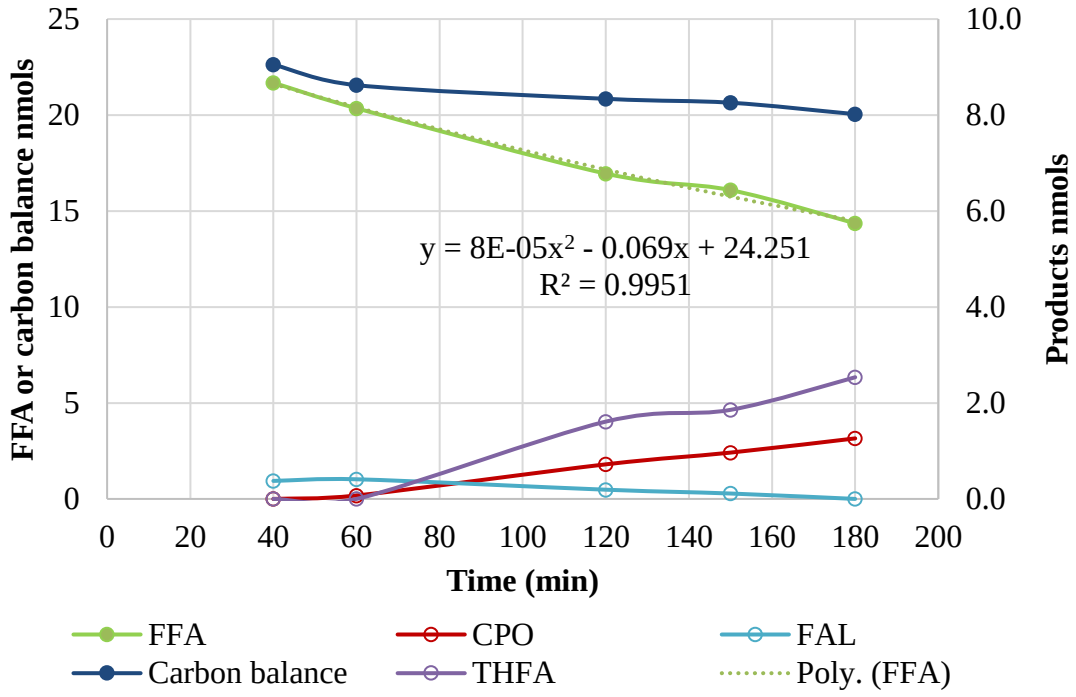

Figure A7 Product analysis of 0.2%Cu-1.3%Pd /SiO_2 SEA-ED; solide circles are by primary axis (left) and empty circles follow secondary axis (right).

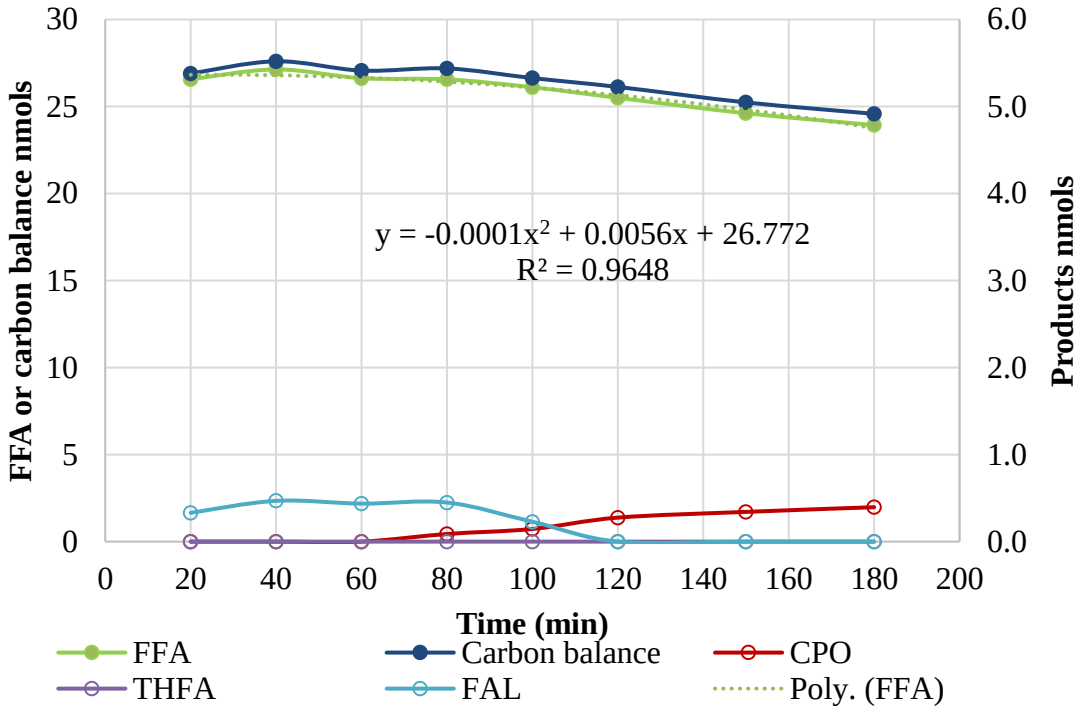

Figure A8 Product analysis of 0.4%Cu-1.3%Pd /SiO_2 SEA-ED; solide circles are by primary axis (left) and empty circles follow secondary axis (right).

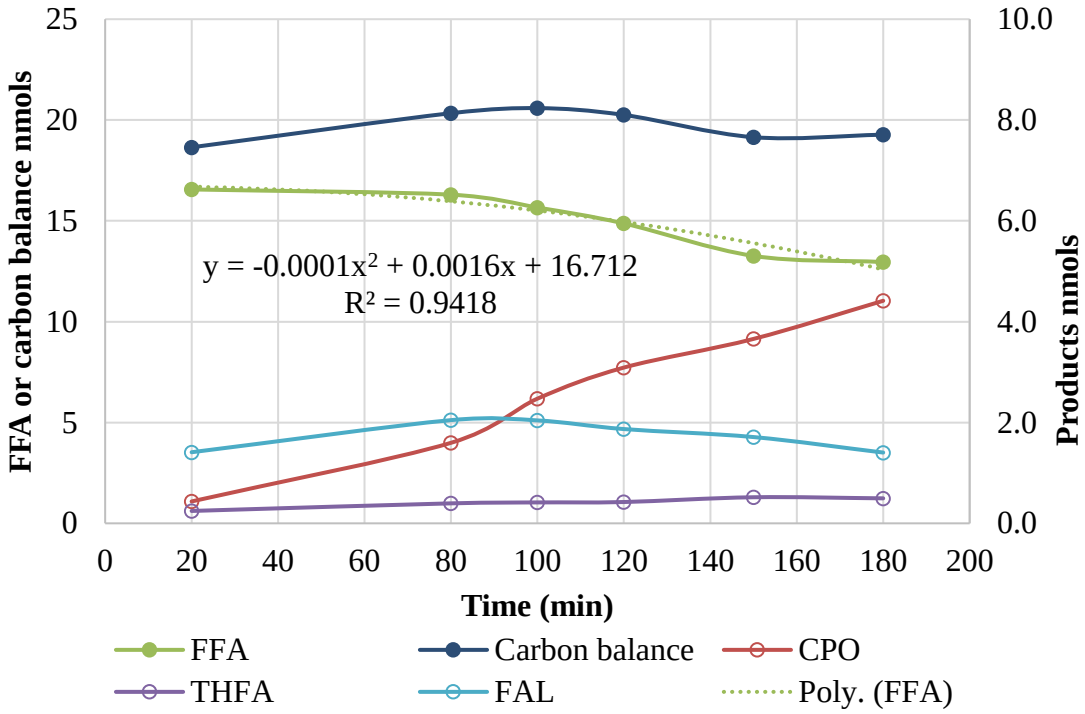

Figure A9 Product analysis of 1.3%Pd-0.7%Co /SiO_2 SEA; solide circles are by primary axis (left) and empty circles follow secondary axis (right).

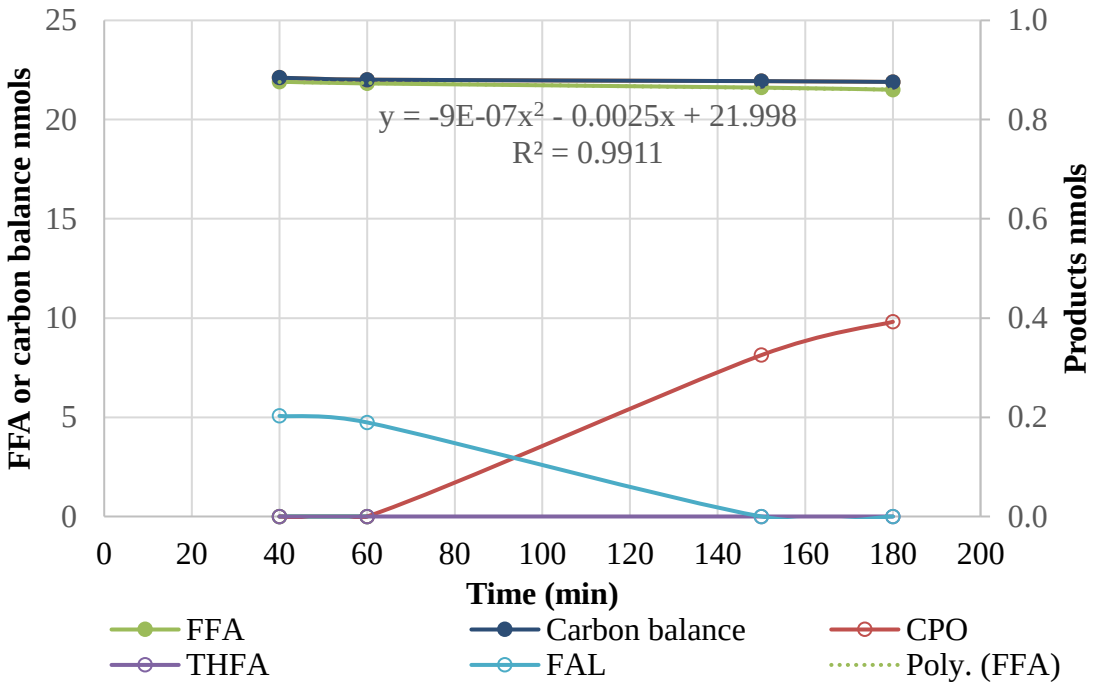

Figure A10 Product analysis of 1.3%Pd-0.7%Co /SiO_2 DI; solide circles are by primary axis (left) and empty circles follow secondary axis (right).

Appendix B

Permission to re-use Chapter 4.2.1

Re-use permission requests

Material published by the Royal Society of Chemistry and other publishers is subject to all applicable copyright, database protection, and other rights. Therefore, for any publication, whether printed or electronic, permission must be obtained to use material for which the author(s) does not already own the copyright. This material may be, for example, a figure, diagram, table, photo or some other image.

Author reusing their own work published by the Royal Society of Chemistry

You do not need to request permission to reuse your own figures, diagrams, etc, that were originally published in a Royal Society of Chemistry publication. However, permission should be requested for use of the whole article or chapter except if reusing it in a thesis. If you are including an article or book chapter published by us in your thesis please ensure that your co-authors are aware of this.

Reuse of material that was published originally by the Royal Society of Chemistry must be accompanied by the appropriate acknowledgement of the publication. The form of the acknowledgement is dependent on the journal in which it was published originally, as detailed in 'Acknowledgements'.

Appendix C

Permission to reproduce Chapter 4.2.2

ELSEVIER LICENSE
TERMS AND CONDITIONS

Mar 06, 2017

This Agreement between Qiuli Liu ("You") and Elsevier ("Elsevier") consists of your license details and the terms and conditions provided by Elsevier and Copyright Clearance Center.

License Number	4063050360587
License date	Mar 06, 2017
Licensed Content Publisher	Elsevier
Licensed Content Publication	Catalysis Today
Licensed Content Title	A pinch of salt to control supported Pt nanoparticle size
Licensed Content Author	Qiuli Liu,Jadid Samad,John E. Copple,Somayeh Eskandari,Christine Satterwhite,John R. Regalbuto
Licensed Content Date	1 February 2017
Licensed Content Volume	280
Licensed Content Issue	n/a
Licensed Content Pages	7
Start Page	246
End Page	252
Type of Use	reuse in a thesis/dissertation
Portion	full article
Format	both print and electronic
Are you the author of this Elsevier article?	Yes
Will you be translating?	No
Order reference number	
Title of your thesis/dissertation	Rational synthesis of catalysts for biomass conversion
Expected completion date	Mar 2017
Estimated size (number of pages)	125
Elsevier VAT number	GB 494 6272 12
Requestor Location	Qiuli Liu 541 Main St RM020 COLUMBIA, SC 29209 United States Attn: Qiuli Liu
Publisher Tax ID	98-0397604
Total	0.00 USD
Terms and Conditions	

INTRODUCTION

1. The publisher for this copyrighted material is Elsevier. By clicking "accept" in connection with completing this licensing transaction, you agree that the following terms and conditions apply to this transaction (along with the Billing and Payment terms and conditions established by Copyright Clearance Center, Inc. ("CCC"), at the time that you opened your Rightslink account and that are available at any time at http://myaccount.copyright.com).

GENERAL TERMS

2. Elsevier hereby grants you permission to reproduce the aforementioned material subject to the terms and conditions indicated.
3. Acknowledgement: If any part of the material to be used (for example, figures) has appeared in our publication with credit or acknowledgement to another source, permission must also be sought from that source. If such permission is not obtained then that material may not be included in your publication/copies. Suitable acknowledgement to the source must be made, either as a footnote or in a reference list at the end of your publication, as follows:
"Reprinted from Publication title, Vol /edition number, Author(s), Title of article / title of chapter, Pages No., Copyright (Year), with permission from Elsevier [OR APPLICABLE SOCIETY COPYRIGHT OWNER]." Also Lancet special credit - "Reprinted from The Lancet, Vol. number, Author(s), Title of article, Pages No., Copyright (Year), with permission from Elsevier."
4. Reproduction of this material is confined to the purpose and/or media for which permission is hereby given.
5. Altering/Modifying Material: Not Permitted. However figures and illustrations may be altered/adapted minimally to serve your work. Any other abbreviations, additions, deletions and/or any other alterations shall be made only with prior written authorization of Elsevier Ltd. (Please contact Elsevier at permissions@elsevier.com). No modifications can be made to any Lancet figures/tables and they must be reproduced in full.
6. If the permission fee for the requested use of our material is waived in this instance, please be advised that your future requests for Elsevier materials may attract a fee.
7. Reservation of Rights: Publisher reserves all rights not specifically granted in the combination of (i) the license details provided by you and accepted in the course of this licensing transaction, (ii) these terms and conditions and (iii) CCC's Billing and Payment terms and conditions.
8. License Contingent Upon Payment: While you may exercise the rights licensed immediately upon issuance of the license at the end of the licensing process for the transaction, provided that you have disclosed complete and accurate details of your proposed use, no license is finally effective unless and until full payment is received from you (either by publisher or by CCC) as provided in CCC's Billing and Payment terms and conditions. If full payment is not received on a timely basis, then any license preliminarily granted shall be deemed automatically revoked and shall be void as if never granted. Further, in the event that you breach any of these terms and conditions or any of CCC's Billing and Payment terms and conditions, the license is automatically revoked and shall be void as if never granted. Use of materials as described in a revoked license, as well as any use of the materials beyond the scope of an unrevoked license, may constitute copyright infringement and publisher reserves the right to take any and all action to protect its copyright in the materials.
9. Warranties: Publisher makes no representations or warranties with respect to the licensed material.
10. Indemnity: You hereby indemnify and agree to hold harmless publisher and CCC, and their respective officers, directors, employees and agents, from and against any and all claims arising out of your use of the licensed material other than as specifically authorized pursuant to this license.
11. No Transfer of License: This license is personal to you and may not be sublicensed, assigned, or transferred by you to any other person without publisher's written permission.
12. No Amendment Except in Writing: This license may not be amended except in a writing signed by both parties (or, in the case of publisher, by CCC on publisher's behalf).
13. Objection to Contrary Terms: Publisher hereby objects to any terms contained in any purchase order, acknowledgment, check endorsement or other writing prepared by you, which terms are inconsistent with these terms and conditions or CCC's Billing and Payment terms and conditions. These terms and conditions, together with CCC's Billing and Payment terms and conditions (which are incorporated herein), comprise the entire agreement between you and publisher (and CCC) concerning this licensing transaction. In the event of any conflict between your obligations established by these terms and conditions and those

established by CCC's Billing and Payment terms and conditions, these terms and conditions shall control.

14. Revocation: Elsevier or Copyright Clearance Center may deny the permissions described in this License at their sole discretion, for any reason or no reason, with a full refund payable to you. Notice of such denial will be made using the contact information provided by you. Failure to receive such notice will not alter or invalidate the denial. In no event will Elsevier or Copyright Clearance Center be responsible or liable for any costs, expenses or damage incurred by you as a result of a denial of your permission request, other than a refund of the amount(s) paid by you to Elsevier and/or Copyright Clearance Center for denied permissions.

LIMITED LICENSE

The following terms and conditions apply only to specific license types:

15. **Translation**: This permission is granted for non-exclusive world **English** rights only unless your license was granted for translation rights. If you licensed translation rights you may only translate this content into the languages you requested. A professional translator must perform all translations and reproduce the content word for word preserving the integrity of the article.

16. **Posting licensed content on any Website**: The following terms and conditions apply as follows: Licensing material from an Elsevier journal: All content posted to the web site must maintain the copyright information line on the bottom of each image; A hyper-text must be included to the Homepage of the journal from which you are licensing at http://www.sciencedirect.com/science/journal/xxxxx or the Elsevier homepage for books at http://www.elsevier.com; Central Storage: This license does not include permission for a scanned version of the material to be stored in a central repository such as that provided by Heron/XanEdu.

Licensing material from an Elsevier book: A hyper-text link must be included to the Elsevier homepage at http://www.elsevier.com . All content posted to the web site must maintain the copyright information line on the bottom of each image.

Posting licensed content on Electronic reserve: In addition to the above the following clauses are applicable: The web site must be password-protected and made available only to bona fide students registered on a relevant course. This permission is granted for 1 year only. You may obtain a new license for future website posting.

17. **For journal authors:** the following clauses are applicable in addition to the above:

Preprints:

A preprint is an author's own write-up of research results and analysis, it has not been peer-reviewed, nor has it had any other value added to it by a publisher (such as formatting, copyright, technical enhancement etc.).

Authors can share their preprints anywhere at any time. Preprints should not be added to or enhanced in any way in order to appear more like, or to substitute for, the final versions of articles however authors can update their preprints on arXiv or RePEc with their Accepted Author Manuscript (see below).

If accepted for publication, we encourage authors to link from the preprint to their formal publication via its DOI. Millions of researchers have access to the formal publications on ScienceDirect, and so links will help users to find, access, cite and use the best available version. Please note that Cell Press, The Lancet and some society-owned have different preprint policies. Information on these policies is available on the journal homepage.

Accepted Author Manuscripts: An accepted author manuscript is the manuscript of an article that has been accepted for publication and which typically includes author-incorporated changes suggested during submission, peer review and editor-author communications.

Authors can share their accepted author manuscript:

- immediately
  - via their non-commercial person homepage or blog
  - by updating a preprint in arXiv or RePEc with the accepted manuscript
  - via their research institute or institutional repository for internal institutional uses or as part of an invitation-only research collaboration work-group

- directly by providing copies to their students or to research collaborators for their personal use
- for private scholarly sharing as part of an invitation-only work group on commercial sites with which Elsevier has an agreement

– after the embargo period
  - via non-commercial hosting platforms such as their institutional repository
  - via commercial sites with which Elsevier has an agreement

In all cases accepted manuscripts should:

– link to the formal publication via its DOI
– bear a CC-BY-NC-ND license - this is easy to do
– if aggregated with other manuscripts, for example in a repository or other site, be shared in alignment with our hosting policy not be added to or enhanced in any way to appear more like, or to substitute for, the published journal article.

Published journal article (JPA): A published journal article (PJA) is the definitive final record of published research that appears or will appear in the journal and embodies all value-adding publishing activities including peer review co-ordination, copy-editing, formatting, (if relevant) pagination and online enrichment.
Policies for sharing publishing journal articles differ for subscription and gold open access articles:
Subscription Articles: If you are an author, please share a link to your article rather than the full-text. Millions of researchers have access to the formal publications on ScienceDirect, and so links will help your users to find, access, cite, and use the best available version.
Theses and dissertations which contain embedded PJAs as part of the formal submission can be posted publicly by the awarding institution with DOI links back to the formal publications on ScienceDirect.
If you are affiliated with a library that subscribes to ScienceDirect you have additional private sharing rights for others' research accessed under that agreement. This includes use for classroom teaching and internal training at the institution (including use in course packs and courseware programs), and inclusion of the article for grant funding purposes.
Gold Open Access Articles: May be shared according to the author-selected end-user license and should contain a CrossMark logo, the end user license, and a DOI link to the formal publication on ScienceDirect.
Please refer to Elsevier's posting policy for further information.
18. **For book authors** the following clauses are applicable in addition to the above:
Authors are permitted to place a brief summary of their work online only. You are not allowed to download and post the published electronic version of your chapter, nor may you scan the printed edition to create an electronic version. **Posting to a repository:** Authors are permitted to post a summary of their chapter only in their institution's repository.
19. **Thesis/Dissertation**: If your license is for use in a thesis/dissertation your thesis may be submitted to your institution in either print or electronic form. Should your thesis be published commercially, please reapply for permission. These requirements include permission for the Library and Archives of Canada to supply single copies, on demand, of the complete thesis and include permission for Proquest/UMI to supply single copies, on demand, of the complete thesis. Should your thesis be published commercially, please reapply for permission. Theses and dissertations which contain embedded PJAs as part of the formal submission can be posted publicly by the awarding institution with DOI links back to the formal publications on ScienceDirect.

Elsevier Open Access Terms and Conditions
You can publish open access with Elsevier in hundreds of open access journals or in nearly 2000 established subscription journals that support open access publishing. Permitted third party re-use of these open access articles is defined by the author's choice of Creative Commons user license. See our open access license policy for more information.
Terms & Conditions applicable to all Open Access articles published with Elsevier: